Reliability Aspects of Microelectromechanical Systems for Space Applications - Mechanical Properties of Structural Materials and Analysis of Packaging Strains

THÈSE N^{O} 6279 (2014)

PRÉSENTÉE LE 20 OCTOBRE 2014
À LA FACULTÉ DES SCIENCES ET TECHNIQUES DE L'INGÉNIEUR
LABORATOIRE DES MICROSYSTÈMES POUR LES TECHNOLOGIES SPATIALES
PROGRAMME DOCTORAL EN MICROSYSTÈMES ET MICROÉLECTRONIQUE

ÉCOLE POLYTECHNIQUE FÉDÉRALE DE LAUSANNE

POUR L'OBTENTION DU GRADE DE DOCTEUR ÈS SCIENCES

PAR

Tobias BANDI

acceptée sur proposition du jury:

Prof. J. Brugger, président du jury
Prof. H. Shea, Dr A. Neels, directeurs de thèse
Prof. N. de Rooij, rapporteur
Dr A. Dommann, rapporteur
Dr W. Noell, rapporteur

ÉCOLE POLYTECHNIQUE
FÉDÉRALE DE LAUSANNE

Suisse
2014

Abstract

Microelectromechanical systems (MEMS) are an essential ingredient in many technological innovations and a source of game-changing inventions in the automotive industry, space exploration, consumer electronics and medical applications due to its capability to control mechanical effects on a micrometer scale. Especially where accessibility, connectivity, system size and energy supply are limited, microsystems can be an enabling technology for sensing, actuation and data transmission. However, their applicability depends on their ability to operate reliably even in extremely hazardous situations such as in space, where the devices are exposed to high levels of radiation, large temperature variations and accelerations. Improving the design and increasing the lifetime of devices requires the identification and detailed understanding of failure modes.

This thesis was aimed at deepening the understanding of fabrication-related effects and space-relevant environmental hazards on the mechanical properties of MEMS on the material and the systems level. Although countless microsystems have been developed in recent years, several vital questions related to the reliability of MEMS systems and MEMS materials remain open to date. Two topics which merit special attention were at the center of this study: First, the influence of packaging on the functioning and the reliability of microsystems and second, the reliability of microsystems and their materials under the harsh environmental conditions imposed by space applications. Out of this area of interest the following questions were studied:

Strain analysis in MEMS package by HRXRD: Packaging offers protection to the microsystem and aids to maintain a stable environment. However, it also influences the strain distribution in the system, and the energy losses in resonant structures due to air being squeezed in thin gaps between the resonator and the package. The distribution of residual stresses and bonding stresses in a MEMS wafer-level package was analyzed by high-resolution x-ray diffraction (HRXRD) and the possibility of nondestructive investigation of the strain distribution in sub-surface structures was demonstrated.

Air damping in MEMS packages: An improved framework for the analysis of air-damping in microresonators and their packages has been presented. Understanding the pressure sensitivity allows determining the admissible pressure levels in resonator packages, above which the performance is deteriorated by losses through air-damping. In addition, monitoring the resonance frequency and quality factor variations over time can be used to determine the hermeticity and leak rates in very small packages where the traditional helium leak test method fails because the relevant leak rates are below its sensitivity.

Reliability of MEMS under space-relevant environmental hazards: The performance of resonant microstructures is directly linked to the Young's modulus of the utilized material and therefore they are very sensitive to variations thereof. The susceptibility of microfabricated structural materials (SU-8 and silicon) to proton irradiation was investigated. In order to isolate the influence of radiation on the materials themselves, single material resonators with contactless actuation and readout were tested. The experimental results showed that single crystal silicon and SU-8 were tolerant to high doses of proton radiation and are hence very well suited for MEMS in space applications in this regard. In addition, the impact of proton and gamma-irradiation on piezoelectrically activated silicon tuning fork resonators was investigated. A very good radiation tolerance was observed, with no significant degradation at total ionizing doses of up to 170 krad. Mechanical tests were carried out to assess the susceptibility to shocks and vibrations encountered during space missions. The devices were found to be fully immune to such hazards.

By investigating space-relevant environmental hazards and their effects on MEMS devices this thesis aimed at contributing to the continued efforts by the scientific community to foster microsystems for space applications.

Keywords: microelectromechanical system, reliability, radiation, space, high resolution x-ray diffraction, finite element simulation, mechanical properties of materials, damping.

Résumé

Les microsystèmes (MEMS) sont un ingrédient clé dans l'innovation technologique et la source d'inventions novatrices dans les industries automobiles, pour l'exploration spatiale, l'électronique de loisir et dans les technologies médicales. Cela est dû à leur capacité de rendre contrôlable des effets mécaniques à l'échelle micrométrique. Les microsystèmes présentent une alternative efficace pour la détection, l'actionnement et la transmission de données, particulièrement là ou l'accessibilité, la connectivité, la taille du système ainsi que l'apport d'énergie sont limités. Cependant, l'utilisation des microsystèmes exige un fonctionnement fiable dans des environnements sévères comme dans l'espace où ils sont exposés à des niveaux élevés de rayonnement et à de grandes variations de température et d'accélération. L'amélioration de la conception, de la fabrication et du fonctionnement des microsystèmes ne peut se faire que si les modes de défaillance ont été identifiés et une compréhension détaillé du système a été établie.

Cette étude vise à approfondir notre compréhension des effets liés à la fabrication et aux risques environnementaux sur les propriétés mécaniques des matériaux utilisés dans les microsystèmes. Bien qu'un grand nombre de microsystèmes aient été développés à ce jour, d'importantes questions demeurent sans réponse quant à la fiabilité des MEMS et des matériaux utilisés. Les deux sujets suivant méritent une attention particulière et ont été placés au centre de ce travail : Premièrement, l'influence de l'encapsulation sur le fonctionnement et la fiabilité des microsystèmes et deuxièmement, la fiabilité des microsystèmes et de leurs matériaux dans les conditions extrêmes de l'espace. Dans ces domaines d'intérêt, les questions suivantes ont été examinées en détail :

L'analyse des contraintes dans l'encapsulation des MEMS par HRXRD : L'encapsulation est un moyen de protéger les microsystèmes et de maintenir un environnement stable. Mais cela influence aussi la distribution des contraintes dans le système ainsi que la perte d'énergie dans les structures résonantes en raison de l'air coincé dans l'espace entre le résonateur et les structures voisines. La distribution des contraintes résiduelles ainsi que celles induites par l'encapsulation ont été examinées par la diffraction des rayons X à haute résolution (HRXRD). La possibilité d'analyse non destructive de contrainte sous la surface et dans des structures encapsulées a été discutée.

L'amortissement par une couche mince de fluide comprimé dans l'encapsulage des MEMS : Un cadre amélioré d'analyse de l'amortissement par l'air dans des microrésonateurs et leur encapsulage est présenté. La compréhension de la sensibilité à la pression permet de déterminer le niveau de pression admissible au-dessus duquel la performance d'un système est sensiblement diminuée dû à l'amortissement par l'air. Cela permet également la conception de résonateurs pour lesquels les variations de la fréquence de résonance et du facteur de qualité sont indicatives du taux de fuite. Cela est d'un grand intérêt pour la détermination du taux de fuite dans des cavités très petites.

La fiabilité des MEMS dans les conditions spatiales: La performance des microstructures résonnantes est directement liée au module de Young des matériaux utilisés et, de ce fait, les MEMS sont très sensibles aux variations de cette propriété mécanique. La susceptibilité de deux matériaux utilisés dans la structure des microsystèmes, le silicium et le SU-8, aux dommages causés par le rayonnement protonique a été étudiée. Afin d'isoler les effets du rayonnement, des résonateurs faits d'un seul matériau avec des modes d'actionnement et de caractérisation sans contact ont été utilisés. Les résultats obtenus indiquent que le silicium monocristallin et le SU-8 supportent des doses élevés de rayonnement protonique et sont donc bien adaptés à des applications spatiales à cet égard. L'impact des protons et des rayons gamma sur le fonctionnement de résonateurs en silicium activés par une couche mince piézoélectrique a également été analysé. Une haute tolérance à l'irradiation sans dégradation de performance jusqu'à 170 krad a été observée. Des essais mécaniques simulant les chocs et les vibrations pendant une mission spatiale ont aussi été effectués. Aucun dispositif défectueux n'a été trouvé à l'issue de ces tests.

Par l'investigation de l'impact des conditions environnementales spatiales sur le fonctionnement et la fiabilité des microsystèmes, cette thèse vise à supporter les efforts continus de la communauté scientifique à favoriser les systèmes micro-électro-mécaniques dans le domaine des applications spatiales.

Mots clés: systèmes micro-électro-mécaniques, fiabilité, radiation, espace, diffraction des rayons X à haute résolution, simulations par éléments finis, propriétés mécaniques des matériaux, amortissement.

Zusammenfassung

Mikroelektromechanische Systeme (MEMS) sind eine Quelle sowohl kontinuierlicher Innovation als auch bahnbrechender Fortschritte in einer Vielzahl von Bereichen von der Automobilindustrie und der Raumfahrtstechnologie über die Unterhaltungselektronik bis hin zur Medizintechnologie. Der Schlüssel zu diesem Innovationspotential liegt in der Möglichkeit, mechanische Effekte auf der Mikrometerskala zu kontrollieren und nutzbar zu machen. In Anwendungen in denen die Energieversorgung, die Raumverhältnisse und die Zugänglichkeit eingeschränkt sind, sind Mikrosysteme oft die einzige Möglichkeit, Sensorik und Steuerungselemente an zentralen Stellen einzubauen, und die Energie- und Datenverbindung sicherzustellen. Der Einsatz von MEMS verlangt jedoch eine verlässliche und korrekte Funktionsweise des Systems. Dies gilt in besonderem Mass für anspruchsvolle Umgebungen wie dem Weltall, wo Mikrosysteme beispielsweise hohen Strahlenbelastungen und Temperaturschwankungen ausgesetzt sind und wo eine Reparatur praktisch unmöglich ist. Die Gewährleistung und Verbesserung der Zuverlässigkeit von MEMS bedingt eine genaue Kenntnis der Fehlerart und –folgen.

Ziel dieser Arbeit war es, ein vertieftes Verständnis von prozess- und umweltbedingten Einflüssen auf die mechanischen Eigenschaften von Mikrosytemen auf der Material- und Systemebene zu erreichen. Obschon bereits eine Vielzahl von Mikrosystemen entwickelt wurde, sind wichtige Fragen bezüglich der Zuverlässigkeit bis heute unbeantwortet geblieben. Zwei Themenbereiche die besondere Aufmerksamkeit verdienen, standen im Zentrum dieser Arbeit: Erstens der Einfluss der Verpackung auf die Zuverlässigkeit und die Funktionsfähigkeit von Mikrosystemen, und zweitens die Beständigkeit von MEMS und den eingesetzten Materialien im rauen Umfeld, dem Mikrosysteme in Raumfahrtsmissionen ausgesetzt sind. Aus diesem Themenbereich wurden folgende Fragen detailliert untersucht:

Analyse der Spannungs- und Dehnungsverteilung in Mikrosystemverkapselungen: Die Verpackung bietet einen Schutz und sorgt für eine stabile Umgebung. Gleichzeitig wird jedoch durch die Verpackung auch die Spannungs- und Dehnungsverteilung des Systems beeinflusst, was zu einem veränderten Alterungsprozess und zu zusätzlicher Dämpfung von Schwingelementen führen kann. Die Eigenspannungen in einer Verpackung auf der Wafer-Ebene wurden durch hochauflösende Röntgendiffraktion (HRXRD) analysiert. Dazu wurde die Möglichkeit einer zerstörungsfreien Untersuchung der Dehnungsverteilung in Strukturen unter der Probenoberfläche demonstriert.

Luftdämpfung in Mikrosystemverkapselungen: Ein erweiterter Ansatz für die Analyse von Luftdämpfung in Mikrosystemen und deren Verkapselung wurde vorgestellt. Das Verständnis dieser Dämpfungsprozesse bildet die Basis für die Bestimmung des zulässigen Luftdrucks im Innern der Verpackung, dessen Überschreitung einen messbaren Einfluss auf die Leistung des Systems hat. Zusätzlich dazu erlaubt dies die Entwicklung von Resonatoren, deren Resonanzfrequenz und Dämpfungskoeffizient einen Rückschluss auf die Leckrate einer Verkapselung ermöglichen.

Zuverlässigkeit von Mikrosystemen für Raumfahrtsmissionen: Die Eigenschaften von resonanten Mikrosystemen ist von der Elastizität der eingesetzten Materialien abhängig, und daher auch sehr empfindlich gegenüber deren Veränderung. Die Beständigkeit von zwei Strukturmaterialien, Silizium und SU-8, unter Protonenbestrahlung wurde untersucht. Um die Effekte auf die Materialien selbst isolieren zu können, wurden aus einem einzigen Material bestehende Resonatoren hergestellt und mittels kontaktloser Methoden angeregt und charakterisiert. Die Resultate dieser Experimente bestätigten, dass die beiden Materialien äusserst tolerant gegenüber intensiver Bestrahlung mit Protonen sind und daher gut für Raumfahrtsapplikationen geeignet sind. Des Weiteren wurde der Einfluss von Protonenstrahlen und Gammastrahlen auf piezoelektrisch aktivierte Siliziumresonatoren getestet. Eine sehr gute Funktionstüchtigkeit des Systems unter Strahlenbelastungen, ohne signifikante Schäden bei Strahlungsdosen von bis zu 170 krad, wurde nachgewiesen. Zusätzlich dazu wurde die Zuverlässigkeit der Resonatoren unter mechanischen Schocks und Vibrationen, wie sie beim Start einer Rakete auftreten, überprüft und nachgewiesen.

Durch die Untersuchung der Zuverlässigkeit von Mikrosystemen und Mikrosystemmaterialien unter den äusserst anspruchsvollen Bedingungen im Weltall, versucht diese Arbeit einen Beitrag zu der Förderung von Mikrosystemen in Raumfahrtsapplikationen zu leisten und das Potential dieser Technologie auszuschöpfen.

Schlagwörter: Mikroelektromechanische Systeme, Zuverlässigkeit, Bestrahlung, Raumfahrt, Hochauflösende Röntgendiffraktion, Finite Elemente Simulation, Mechanische Materialeigenschaften, Dämpfung.

Acknowledgements

A research project like this is never a completely isolated work. It would not have been possible to perform the experiments and write this thesis without the help and support of many kind people around me, only some of whom it is possible to mention in particular here.

Above all, I would like to express my deep appreciation and gratitude to my supervisors Dr. Antonia Neels and Prof. H. R. Shea for their support, guidance and advice throughout the research project. The unsurpassed scientific expertise of Prof. Dr. Shea in the field of MEMS reliability, together with his willingness to give his time for valuable and constructive suggestions, criticism and advice was greatly appreciated. Antonia Neels has guided me throughout the project with profound knowledge and experimental and scientific proficiency, enthusiastic encouragement and very constructive critiques. She always gave me the liberty to work my own way, encouraged me in taking new challenges and always supported me when required. The XRD Applications Laboratory (now part of the Characterization & Quality Assurance sector) set up by her and Prof. Dr. Alex Dommann at the Centre Suisse d'Electronique et de Microtechnique SA (CSEM) provided for an enormously stimulating environment for this project. Alex Dommann's passion for x-rays in general, diffraction techniques in specific and all technologic domains to which x-rays can be benefitially applied (hence almost all areas of science) has sparked over to me too.

The funding of this work by the Networking/Partnering Initiative (NPI) of the European Space Agency and the Swiss National Science Foundation are gratefully acknowledged.

I am deeply thankful to the internal and external examiners of my Jury, Prof. Dr. Nico F. de Rooij, Prof. Dr. Alex Dommann and Dr. Wilfried Noell who have honored me by accepting to review and evaluate this thesis and Prof. Jürgen Brugger for accepting to be the president of the jury.

The continued support of this thesis by Prof. Dr. Nico F. de Rooij, Prof. Dr. Alex Dommann and Patrick Albert, the heads of the Microsystems Technology division at CSEM, is very gratefully acknowledged.

I am very thankful for the work of my colleagues at CSEM and EPFL, Dr. Andreas Schifferle and Dr. Joao Polido-Gomes. Without their achievements on the mechanical testing equipment, the RSM simulation, and on the single-material resonators, this work would not have been possible in this form.

I would like to thank the members of our group, Dr. Olha Sereda, Dr. Xavier Maeder, Dr. Marios Garganourakis, Dr. Andreas Schifferle, Dr. Massoud Dadras, Mireille Le Boeuf, Silvia Biselli, Aziz Ibzazene and Dr. Jeremy Tillier. The daily work with them was invaluable on both an academic and a personal level, for which I am extremely grateful, and many experiments would not have been possible without their help.

This work would neither have been possible without the help from the staff of the Microsystems Technology division. I would like to particularly thank the persons responsible for the fabrication of the silicon tuning fork resonators: Dr. Claude Muller, Dr. Jacek Baborowski, Aurélie Pezous, Dr. Philippe Niedermann, Dr. Francis Cardot and Sylvain Jeanneret.

In the frame of the ESA-NPI project I was fortunate to have the exciting opportunity to work at in the facilities of the European Space Research and Technology Centre (ESTEC) during about 8 months. This enabled me to gain experience with many different methods for testing and analyzing components and materials. Moreover, I learned much about the specific requirements and quality standards of space applications. I am very grateful to having been able to profit from the excellent facilities and specialist know-how at ESTEC.

I am very grateful to Laurent Marchand from the European Space Agency for the continued project support. His enthusiasm and devotion to foster MEMS in space applications were extremely inspiring for me. His continuous efforts to introduce me into the many-sided activities of ESA have allowed me to gain invaluable insight into the functioning of space projects and the European space industry.

I kindly acknowledge the support of the members of ESA's Components Technology and Space Materials Division and the Space Components Standardisation and Evaluation Division. First and foremost I would like to thank Nicolas Saillen for the technical guidance and expertise, Michele Muschitiello, Alessandra Costantino and Bob Nickson for the support during the ^{60}Co irradiation tests and Christian Poivey for helpful discussions on the radiation test planning. In addition I express my gratitude towards the members of the Materials & Electrical Components Laboratory for helpful hands and patient explanations in the experimental work done at ESTEC.

I would also like to thank all colleagues at CSEM and EPFL for the excellent working atmosphere and the good times spent together.

My deepest thanks go to my family and friends, who have been a great source of support throughout my life and this thesis.

And last but most importantly, I thank Nathalie. Thank you for your endless support and the joy and love that you bring to every day of my life.

I am very grateful to having had the possibility to work and live with so many inspiring and visionary personalities!

Contents

List of Figures

List of Tables

List of Abbreviations

AC	Alternating current
ATR-FTIR	Attenuated Total Reflection - Fourier Transform Infrared Spectroscopy
AU	Astronomical Unit
CERN	European Organization for Nuclear Research
CMOS	Complementary Metal-Oxide-Semiconductor
CSEM	Swiss Center for Electronics and Microtechnology
CTE	Coefficient of Thermal Expansion
CTI	Commission for Technology and Innovation
DC	Direct Current
DRIE	Deep Reactive Ion Etching
EBSD	Electron Backscatter Diffraction
ECSS	European Cooperation for Space Standardization
EDX	Energy-Dispersive X-ray Spectroscopy
EEE	Electrical, Electronic and Electromechanical (parts)
EPFL	Swiss Federal Institute of Technology in Lausanne
ESA	European Space Agency
ESCC	European Space Components Coordination
FEA	Finite Element Analysis
FWHM	Full Width at Half Maximum
GEO	Geostationary Earth Orbit
GPS	Global Positioning System
HNA	(Mixture of) Hydrofluoric acid, Nitric acid and Acetic acid
HRXRD	High-Resolution X-ray Diffraction
IC	Integrated Circuit
IR	Infrared
LEO	Low Earth Orbit

LET	Linear Energy Transfer
LHC	Large Hadron Collider
MD	Molecular Dynamics
MEMS	Micro-Electro-Mechanical System
NIEL	Non-Ionizing Energy Loss
NPI	Networking/Partnering Initiative
PCB	Printed Circuit Board
PEB	Post Exposure Bake
PGMEA	Propylene glycol methyl ether acetate
PMMA	Poly(methyl methacrylate)
RC	Rocking Curve
RFID	Radio-Frequency Identification
RSM	Reciprocal Space Map
RTC	Real Time Clock
SEM	Scanning Electron Microscope
SOI	Silicon on Insulator
SRIM	Stopping and Range of Ions in Matter
TCF	Temperature Coefficient of Frequency
TCXO	Temperature Compensated Crystal Oscillator
TDD	Total Displacement Dose
TEM	Transmission Electron Microscopy
TID	Total Ionizing Dose
TMAC	Tangential Momentum Accommodation Coefficient
ToF-SIMS	Time of Flight - Secondary Ion Mass Spectrometry
UV	Ultraviolet
XRD	X-ray Diffraction

Chapter 1

Introduction

Microelectromechanical systems (MEMS) offer the possibility to gain control over mechanical effects on a micrometer scale. Co-integrating micromechanisms with optical, chemical, magnetic and electronic elements allows building complex systems which enable dramatic reduction of mass, size and power consumption and give access to new ranges of physical effects unattainable by macrosystems. As a result, MEMS technology is an essential ingredient in many technological innovations and a source of game-changing inventions in automotive industry, space exploration, consumer electronics, and medical applications.

Based on basic structural elements such as beams, membranes and hinges, made from materials as diverse as semiconductors, metals, ceramics and polymers, and integrated with sensing elements and actuators based on electrical, thermal, chemical and optical effects, a huge range of highly complex devices can be fabricated. In addition to the miniaturization, microfabrication processes enable highly parallel batch processing, excellent uniformity and low unit costs.

Yet to bring a product to market-readiness is very challenging. Although MEMS devices are commonly based on high-quality and very stable materials such as single-crystal silicon, the system complexity and the high number of required process steps in device fabrication pose a great challenge to the long-term reliability, as many of the involved processes introduce defects and strains [1]. For instance, residual stresses may be caused by a mismatch of the crystal lattice parameters or the thermal expansion between adjacent materials. Exposure to plasmas and etching agents influences the surface roughness and causes subsurface damage by diffusion, particle penetration and radiation damage.

In addition to the fabrication related defects, the MEMS may be exposed harsh conditions during assembly, packaging, integration, transport, storage and operation. Some of the most demanding environments in which MEMS are used are the outer space, the deep seas, the Earth's poles and subterranean areas. Where accessibility, connectivity, system size and energy supply are limited, microsystems can be an enabling technology, yet their applicability depends on their ability to operate reliably in these extreme situations. A profound knowledge of the possible deficiencies is crucial to mitigating failure modes, increasing fabrication yields and ensuring long-term functioning. The variety of possible sources of failure and degradation calls for appropriate techniques to identify and analyze underlying causes

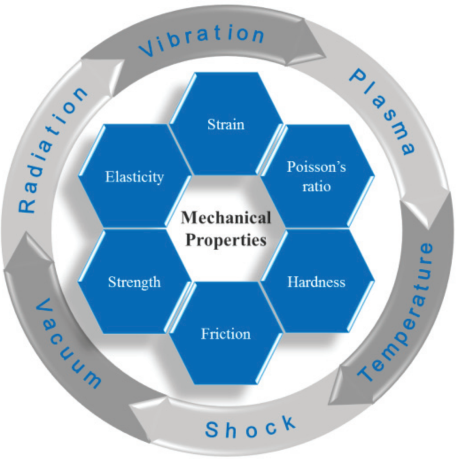

Figure 1.1: A selection of mechanical properties of MEMS materials. These properties may be influenced by fabrication processes and environmental hazards.

from the materials level to systems. For this reason, there is a need for techniques for failure mode and effects analysis which are adopted to the advancing fabrication technologies and new application domains.

In microsystems the mechanical properties of the utilized materials are often of special importance: For instance, resonant structures are used in a broad range of MEMS such as accelerometers, gyroscopes, time-keeping oscillators and resonant-mode filters. Their performance is directly linked to the Young's modulus and Poisson's ratio of the resonant element and therefore they are also very sensitive to variations in these parameters. Furthermore, structures under mechanical load or residual stresses may undergo sudden performance shifts, drift and even catastrophic failure due to creep, fatigue or fracture.

The mechanical properties which are of highest interest are [2]-[5]

- the Young's modulus,
- the Poisson's ratio,
- the yield and fracture strengths,
- Residual stresses and strain gradients

as well as energy dissipation such as friction and damping (Figure 1.1).

This thesis was aimed at deepening the understanding of fabrication-related effects and space-relevant environmental hazards on these properties on the material and the systems level. A combination of environmental and mechanical testing, model simulations and material and device characterization techniques was used to approach this task. These three sets of tools and methods present a holistic view of the reliability and failure of MEMS devices

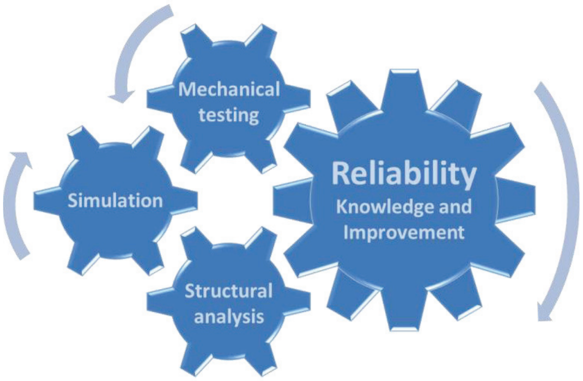

Figure 1.2: Testing, simulations and structural analysis contribute to advancing and improving reliability.

and thereby support the advancement of reliability (Figure 1.2). In this thesis the focus was placed onto a selection of as yet little-studied or unexplored space-relevant effects in microresonators, namely in piezoelectrically activated silicon resonators and in single-material resonators made from silicon and SU-8.

Besides the mentioned ubiquity of resonating structures the choice of microresonators is motivated by the fact that the highest requirements on the stability of the mechanical properties of MEMS materials and systems are imposed by frequency referencing and time-keeping applications. In turn, resonators are excellent systems to investigate variations of the mechanical properties of materials. Silicon resonators are the most advanced technology for MEMS resonators, and are competing with quartz in the time-keeping and frequency referencing markets. In contrast to electronic resonators, which can be easily integrated into CMOS fabrication processes but lack from lower stability and precision, mechanical resonators generally offer high frequency stability and low noise but at the cost of more complex system integration. Microfabricated resonators offer the possibility of low fabrication tolerances paired with parallelized fabrication and packaging which result in low unit costs [6]. The main factors limiting the frequency stability of mechanical oscillators (i.e. a resonator and the sustaining circuit) are short-term instabilities, temperature variations, stress relief, aging, mechanical accelerations and radiation damage [7], [8]. Most of these effects, such as instabilities in the circuitry, mechanical shocks and vibrations can be minimized or compensated. However, when operating under harsh conditions such as at elevated temperatures or pressures, high radiation exposure levels or in corrosive environments, not all environmental effects can be sufficiently reduced and hence their effects on the performance of the devices must be evaluated. The efforts made in this thesis to evaluate the susceptibility and resistance to such environmental hazards in MEMS systems and materials are outlined in the next section.

1.1 Thesis outline and contributions

This thesis is structured as follows. In Chapter 2 an overview over the environmental hazards encountered in space missions is given, together with the known degradation effects such conditions have on microresonators and the mechanical properties of structural materials, in particular silicon and quartz. Chapter 2 also covers the techniques to investigate the variations of Young's modulus, the yield strength and residual stresses in microfabricated specimens.

The reliability investigations made on piezoelectrically activated microresonators are reported on starting in Chapter 3. The investigated device was a silicon tuning fork resonator activated by a thin film of aluminum nitride. The design and fabrication of the devices was done in the Microsystems Technology Division of CSEM and was not part of this thesis. Chapter 3 describes the stress investigation of the eutectic bonding interface using high-resolution x-ray diffraction (HRXRD). Stresses and stress relaxation are an important contributing mechanism for aging in microresonators and hence methods for non-destructive analysis thereof are highly beneficial to the process optimization, quality control and failure analysis. Even though the bonding interface lies tens of micrometers below the device surface it is possible to get a detailed picture of the stress distribution and the influence of the packaging thereon. In addition, the comparison of the experimental results with simulated diffraction patterns based on finite element analyses is discussed.

Chapter 4 treats the influence of air damping on the performance of the piezoelectrically activated tuning fork resonators. Due to the sensitivity to air damping, resonators can be used to determine the hermeticity of MEMS packages. The dependency of the quality factor and resonance frequency on the ambient air pressure was experimentally determined and was compared to theoretical models which were refined and adapted to the specific geometry of the system.

Chapter 5 covers the experimental investigations made on the effect of radiation damage on the mechanical properties of two commonly used materials, single crystal silicon and SU-8. Single-material cantilevers with contactless actuation and readout were used to investigate the radiation tolerance of the two materials, which allows isolating the effect of radiation on the materials themselves. Geometries, fabrication processes and operation modes typical for microsystems were utilized. This allows for transferability of these results to other types of MEMS devices.

Going over from the materials level to the system level, Chapter 6 reports on the susceptibility of the piezoelectrically activated silicon tuning fork resonators to radiation damage as well as space-relevant mechanical loads.

Chapter 7 summarizes the achievements made in this work and gives an outlook on topics of interest for future investigations.

In appendix A the work made on the assessment of the yield strength of single crystal silicon and the progress made on non-linear three-point bending and four-point bending tests adapted for evaluating the stability of thin and highly compliant devices is presented.

Chapter 2

Space-Relevant Environmental Hazards and Methods to Monitor the Elasticity and Residual Stresses in MEMS Materials

The aim of this chapter is first to give the reader an overview over the methods used to investigate the variations of the Young's modulus, residual stresses and the yield strength in MEMS materials. The second goal of this chapter is to discuss the main environmental challenges which may adversely affect MEMS in space. Space technology is a very promising domain for microsystems because MEMS are an enabling technology for miniaturization in space exploration, offering the possibility to significantly reduce the weight, size, power consumption, thermal management complexity, and hence the cost of space exploration, business and commerce. On the other hand, the requirements on the reliability in space applications are also extremely demanding as a result of the harsh environmental conditions.

The chapter is structured as follows. Methods for analyzing the variations of the elasticity of MEMS materials and their yield strength are discussed in sections 2.1 and 2.2. Residual stresses, the use of HRXRD for the nondestructive analysis of strains in microsystems and the role of finite element analysis therein are presented in sections 2.3 to 2.5. Then the most relevant environmental hazards for MEMS in space are discussed. These are ionizing and non-ionizing radiation (section 2.6), thermal effects (section 2.7) and mechanical vibrations and shocks (section 2.8). In addition, the need for hermetic packaging of MEMS and the difficulty in assessing leak rates in small MEMS packages is discussed in section 2.9. The degradation effects caused in quartz and silicon resonators by the different environmental hazards are summarized at the end of the respective sections. The aim is to place this work into context, to outline the obstacles overcome by established technology and state-of-the-art microsystems, and to try to anticipate the nature of the challenges for future MEMS technologies based on resonant structures entering into these markets.

A part of this chapter is published in T. Bandi, H. R. Shea and A. Neels, *Proc. SPIE*, 2014, pp. 9113-10 (© 2014 Society of Photo Optical Instrumentation Engineers).

2.1 Young's modulus

When investigating the effect of environmental hazards and aging on the mechanical properties of materials, a choice has to be made on which experimental technique to use. The selection should be based on the consideration of whether the method gives the most precise results on the *variation* of the material property, in addition to its *absolute* value. For instance, consider the precision by which a change of the elasticity of a material can be determined; Typical test methods to investigate the elasticity are tensile tests, beam bending tests, nanoindentation and resonant tests using beams, plates or films [2]. Table 2.1 shows the formulations of the Young's modulus for these test methods together with estimates of the precision by which a variation of it can be measured. It is assumed that no other parameters such as the temperature, pressure or humidity influence the measurement and that the dimensions of the specimens remain unchanged. Clearly the resonance frequency measurement offers the highest precision and hence is the method of choice to investigate small changes of the materials elasticity in microfabricated structures.

For the first harmonic mode of a cantilever, the resonance frequency f is given by

$$f = \frac{1.875^2}{2\pi} \frac{T}{L^2} \sqrt{\frac{E}{12\rho}} \tag{2.1}$$

where T is the resonator thickness, L is its length, E is the Young's modulus and ρ is the density. The measurement of resonance frequency variations of micro-resonators allows monitoring variations of the elasticity induced by environmental hazards on the ppm-level or even ppb-level as $\Delta f / f = 1/2 * \Delta E / E$. The sensitivity is (only) limited by the precision and accuracy of the frequency measurement and by the degree to which unwanted environmental effects which also influence the resonance frequency can be eliminated. Similar considerations can be made for other mechanical parameters and show for instance that resonant structures oscillating in torsional modes are suited to investigate small variations of Poisson's ratio [9], [10]. Obviously, the results in Table 2.1 reflect the sensitivity of resonant MEMS-structures to variations of the elasticity mentioned in the introduction of this work. The use of resonant structures to investigate the effect of radiation on the elasticity of single-crystal silicon, SU-8 and a piezoelectrically activated microresonator will be discussed in Chapter 5 and Chapter 6.

2.2 Yield strength

The quality of the crystal in a finished MEMS device is influenced by the fabrication and packaging processes, many of which introduce defects that deteriorate the mechanical stability of the material and act as stress concentrators. Due to the brittle nature of silicon these defects can lead to catastrophic failure during assembly, packaging and operation.

Exposure to plasmas and etching agents influences the surface roughness and causes subsurface damage by diffusion, particle penetration and radiation damage. For instance, deep reactive ion etching (DRIE) is an iterative process in which isotropic etching is alternated with a passivation of the sidewalls, giving rise to near-vertical but scalloped and rough trenches in the silicon by means of which the structures to be fabricated are defined [17]. The resulting

Table 2.1: Comparison of test methods to evaluate the Young's modulus[1].

Test	Formulation for Young's modulus	Total differential[2]	Typical Precision[3]	Comment	Main reference
2-point bending	$E = 6\alpha^2 \frac{FB^2}{WT^3}$	$\frac{\Delta E}{E} = \left\lvert\frac{\Delta F}{F}\right\rvert + 2\left\lvert\frac{\Delta B}{B}\right\rvert$	10^{-3}	*B*: Span of the two parallel chucks supporting the U-shaped beam *F*: Elastic force exerted by the beam *L*: Support span [m] *W*: Beam width (perpendicular to the direction of deflection)[m] *T*: Beam thickness (along the direction of deflection) [m] α: Constant (0.835) *d*: Deflection [m]	[11]
3-point bending (linear)	$E = \frac{FL^3}{4WT^3 d}$	$\frac{\Delta E}{E} = \left\lvert\frac{\Delta F}{F}\right\rvert + \left\lvert\frac{\Delta d}{d}\right\rvert$	10^{-3}		[12]
4-point bending (linear)	$E = \frac{5FL^3}{2WT^3 d}$	$\frac{\Delta E}{E} = \left\lvert\frac{\Delta F}{F}\right\rvert + \left\lvert\frac{\Delta d}{d}\right\rvert$	10^{-3}		[12]
Tensile test	$E = \frac{1}{\varepsilon}\frac{F}{WT}$	$\frac{\Delta E}{E} = \left\lvert\frac{\Delta \varepsilon}{\varepsilon}\right\rvert + \left\lvert\frac{\Delta F}{F}\right\rvert$	10^{-3}	ε: Longitudinal strain	[13]
Resonant test	$E = C_r \rho f_{res}^2 \frac{L^4}{T^2}$	$\frac{\Delta E}{E} = 2\left\lvert\frac{\Delta f_{res}}{f_{res}}\right\rvert$	10^{-7}-10^{-9}	for the 1st harmonic resonance $C_r = 12\rho\left(\frac{2\pi}{1.875^2}\right)^2$	[2]
Nanoindentation	$E = \left(1-\nu^2\right)\frac{1}{2\beta}\sqrt{\frac{\pi}{A}}S$	$\frac{\Delta E}{E} = \frac{1}{2}\left\lvert\frac{\Delta A}{A}\right\rvert + \left\lvert\frac{\Delta S}{S}\right\rvert$	10^{-3}-10^{-2}	ν: Poisson's ratio β: Constant (~1) *A*: Projected area of indenter contact *S*: Slope of load-displacement curve	[14], [15], [16]

---

[1] The formulas are given for evaluating the Young's modulus of rectangular beams, except for the nano-indentation.

[2] The total differential is formulated neglecting the error in the dimensions of the specimens. This is justified by the fact that here the focus lies on the changes of the elasticity during aging, where the dimensions are considered to remain constant.

[3] The values are order-of-magnitude estimates based on typical measurement precisions, e.g. that forces in the single-Newton range can be measured with a precision of 0.1-1% [2]. Measurement scattering and uncontrollable parameter variations (e.g. temperature, pressure or humidity) further lower the precisions experimentally achievable.

defects and surface structure directly affect the yield strength. An excellent review of the yield strength of brittle MEMS materials was presented in ref. [18]. The yield strength of single crystal silicon was shown to depend heavily on the size of the specimens and ranged from 17.4 GPa in 200 nm thick beams to 0.5 GPa in 0.5 mm thick specimens [19]. The yield strength depended on the defect density and the total number of defects subjected to mechanical strain. No significant difference in the yield strength was observed between room temperature and 300°C in silicon micro- and nano-beams subjected to bending and tensile tests [20]. At elevated temperatures near 600°C the mechanical behavior of silicon goes over from brittle to ductile [21]. A strong suppression of the brittle-to-ductile transition temperature was reported in nanometer sized specimens, where ductile deformations were observed at room temperature in tension [22] and compression [23]. Also die separation methods such as mechanical blade dicing and laser dicing induce characteristic damage near the cutting lines. Grinding and polishing processes used for wafer thinning leave scratches and marks on the backside of the wafer. More specifically, blade dicing induces chipping and cracking near the cutting line and laser dicing can lead to cracks and zones with high defect densities in the vicinity of the cut surface [24].

Because it is prohibitively complex and time-consuming to test all possible geometries used in MEMS devices it is preferable to use test specimens (e.g. straight beams) to predict the failure distribution of structures with arbitrary shapes [25]-[28]. Moreover, this allows benchmarking new technologies and processes against existing fabrication methods. Nevertheless, the mechanical test setup should allow reproducing the strain conditions and device properties of the use case as close as possible due to the following reasons. First, the distribution of damage varies with the depth of the processed structure. Examples are two-step blade dicing [24] and the variation of the damage with increasing depth of plasma etching [17], which influences the overall strength of structures. Secondly, both cracks initiated at the strained surface and at the strained edges contribute to the failure distribution of silicon dies [29]. For instance, surface and edge flaws were observed to be the main source of chip fracture in flip chip assemblies due to stresses built up by soldering and thermal cycling [30], [31]. Therefore it is important to reproduce the thickness and the loaded-surface-to-edge ratio (i.e. the width of the sample when the thickness is given) as well as the strain directionality as close as possible when simulating stresses occurring in real devices by mechanical testing.

For testing the effect of grinding and polishing, rotationally symmetric bending tests such as the ball-ring test or the ring-ring tests are most suitable [33]. The edges are not loaded in these test geometries and hence they are sensitive to surface damages only. Specialized test geometries such as the twist-bending test or the ball-on-edge test are sensitive to (wafer) edge flaws but the distribution of the stress along the edges is very sensitive to the position of the supports and the stress level itself [32]. Miniaturization of the test setup therefore is challenging. The *n*-point bending tests (*n* equals to 2, 3 or 4) allow testing for edge and surface flaws simultaneously. For detailed reviews on different test setups for evaluating the mechanical reliability of wafers and chips it is referred to [32]-[35] and references therein.

Recently an instrument for displacement controlled two-point bending which allows testing specimens with dimensions similar to typical microfabricated silicon structures has been presented [11]. The specimen was a long, slender beam with a cross-section of 50x50 μm^2 and a length of 5 cm. During the test it was bent in a U-shape and kept between two parallel chucks by its own elasticity. The maximum stress occurred at the apex of the non-linearly bent beam while at the contact points the beam was almost straight and hence strain-free. An advantage of this test geometry is therefore that the contact points of the chucks are far away from the areas with maximum stress which prevents fracture due to additional clamping and contact stresses. During the test the two chucks were approached continuously and the elastic force exerted by the specimen on the chucks was monitored until fracture occurred. Using this setup the effect of post-DRIE treatments on the yield strength of silicon whiskers with a cross-section of 50 x 50 μm^2 was systematically investigated. Significantly increased mechanical stabilities were found for silicon treated by thermal wet oxidation, HNA etching and KOH etching and optimum process parameters were determined.

In the frame of this thesis a further development of this instrument to extend the range of testable yield strengths by implementation of 3-point and 4-point bending was made. This was required because in the 2-point configuration the specimen was fixed by its own elasticity hence it had to be able to support a certain minimum stress at the beginning of the test. For a specimen of 50 μm thickness this was approximately 1 GPa which is beyond the strengths achievable by standard wafer dicing processes. Three- and four-point bending test methods are well established and are commonly made in the linear regime where the bending of the specimens is negligibly small [12], [36], [37]. However, in specimens with small width and thickness, which can be below 100 μm, the non-linearity of the bending must be considered.
As this work is not directly applicable to the piezoelectrically activated microresonator which was at the center of this thesis, the results are discussed in the Appendix A.

2.3 Residual stresses

Packaging is essential for MEMS reliability by providing a stable environment and protection from contaminations and corrosive agents [38]. Due to the shrinking size of structures in microsystems the spatial distance between functional features is reduced too, and as a result, residual strains in one part of the system may interfere with the surrounding elements. Packaging may be a source of performance degradation and failure if the bonding causes strains radiate to the functional parts of the device. Residual stresses by packaging can be induced by mechanical pressure during bonding, by a mismatch of the coefficient of thermal expansion of adjoined materials or from shrinkage of polymer encapsulants [38], [39].

The effect of packaging by anodic bonding on the resonance frequency of a MEMS gyroscope was investigated by Choa [40]. The resonance frequency of the gyroscope was shifted significantly after the bonding process. The problem was mitigated by more efficient mechanical decoupling of the resonant structure from the mounting frame, which was achieved by using a semi-folded suspension instead of an L-shaped suspension. This significantly reduced the bonding-induced effect and improved the stability of the gyroscope in high temperature storage tests.

Residual strains may not cause instantaneous failure but can cause a gradual degradation and premature failure of the device. Loeb and coworkers [41] reported the evaluation of an electrical feed-through into a glass capsule developed for medical implant purposes. When using a 90% Pt-10% Ir alloy, hermetic feedthroughs were obtained, which however, failed catastrophically in thermal cycling tests, due to the mismatch of the coefficients of thermal expansion between the glass and the metallic wire. By using tantalum as a feedthrough material this cause of failure could be eliminated effectively.

The effect of adhesives and the substrate on the strain in MEMS were investigated for silicon double-clamped microresonators [42] and high-g accelerometers [43]. The output of both devices (resonance frequency and resistance of the piezoresistance, respectively) was affected by the strength of the bonding to the substrate. Thicker layers of softer adhesive materials were more effective in decoupling the thermal expansions of the device and the substrate. In [44] it was shown that stresses in micron-thick metal layers deposited on the epitaxially grown silicon encapsulation layer of a double-clamped microresonator directly affected the resonance characteristics and that such systems can also be utilized to study stress-relaxation in the metallic thin films.

Stresses can also be induced intentionally to compensate for mismatches of the thermal expansion coefficients (CTE) and the temperature coefficients of elasticity between materials [45]. Recently a double-clamped silicon resonator with a temperature coefficient of frequency (TCF) of below 1 ppm/°C was demonstrated using this principle [46]. The compensation for the temperature dependent elasticity in silicon was achieved by a careful adjustment of geometrical stress-buffering structures and stresses induced in the silicon due to the CTE mismatch with the Pyrex substrate wafer.

Controlling stress-related effects in MEMS requires theoretical models, simulation tools and also analytical tools for experimentally verifying the predictions and for evaluating the performance of real devices. Finite element analysis (FEA) has been extensively used to predict the stress distribution in MEMS and microresonators [42], [47], [48].

2.4 Analysis of residual stresses by x-ray diffraction

The variety of possible sources of stress-related failure and degradation calls for appropriate techniques to identify and analyze underlying causes from the materials level to systems. X-ray diffraction (XRD) in general and high-resolution x-ray diffraction in particular, is a nondestructive method which can provide answers to various, and in this context most notably stress-related, problems encountered in microsystems engineering.

X-ray diffraction is the basis of a number of experimental methods to probe the periodic structural properties of materials and systems. In crystals, the periodic arrangement of atoms in the lattice leads to strong diffraction peaks. However, also multilayer structures and even amorphous materials can be investigated by this method, as the radial distribution function causes specific variations of the diffracted intensity [49]. For MEMS technology the most important application of x-ray diffraction is the analysis of strain in thin films and in silicon structures, which may be under mechanical load or which may act as a strain gauge for interfaces and adjacent structures [50], [51]. The availability of laboratory instruments with beam-shaping optical elements, monochromators and sensitive detectors enable rapid and precise XRD analyses at reasonable costs.

In comparison to other strain measurement techniques x-ray diffraction offers distinctive advantages. As the diffraction is only dependent on the spacing between atomic planes, single elements of the strain tensor can be assessed, whereas for instance Raman spectroscopy gives a scalar value of the strain [52]. Surface-sensitive methods such as Electron Backscatter Diffraction (EBSD) and Raman spectroscopy are limited to depths of few micrometers or less and thus the investigation of buried structures requires destructive sample preparation [53], [54]. The same applies to Transmission Electron Microscopy (TEM), where high spatial resolution can be achieved but for which the sample needs to be thinned to electron transparency. The limits of the spatial resolution in HRXRD are influenced by the beam size and the x-rays penetration depth, as the whole illuminated volume contributes to the diffracted intensity. On the other hand, the penetration depth of x-rays (on the order of 100 µm in semiconductors) allows investigating sub-surfaces structures in a nondestructive way.

The interference pattern of x-rays scattered on the electrons in a material can be understood as a Fourier transform of the electron density [55]. This transformation from the real space with lattice parameters (a,b,c) leads to the reciprocal space, which, in the simple case of a cubic lattice with edge length a, has the lattice parameters $(h,k,l=n2\pi/a)$, where n is an integer. Each point in the reciprocal space corresponds to a diffraction peak. The distance of reciprocal space points from the origin is $2\pi/d_{hkl}$ for the cubic system, where d_{hkl} is the spacing between the atomic planes with the Miller indices *hkl*. Bragg's equation relates d_{hkl} with the diffraction angle θ

$$d = n\lambda\left[2\sin(\theta)\right]^{-1} \tag{2.2}$$

where n is an integer and λ is the x-ray wavelength. The reciprocal space therefore elegantly reveals the diffracting properties of crystals. The position, shape and background of the diffraction peaks contain information on the strain distribution, orientation and quality of the

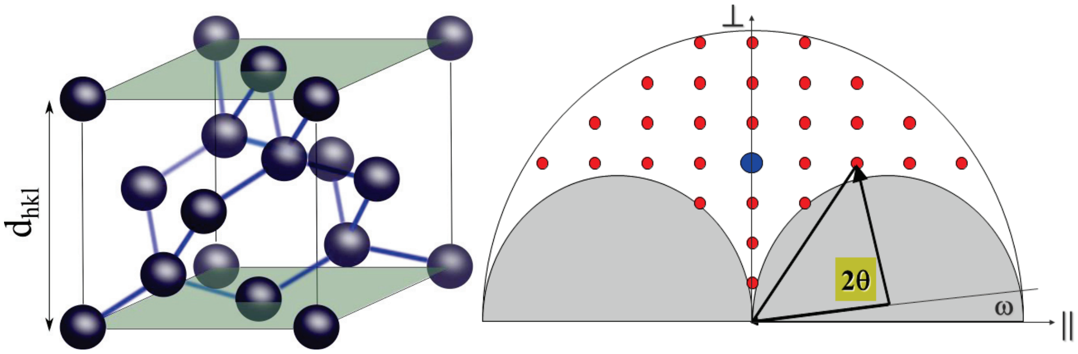

Figure 2.1: (Left) Unit cell of a silicon crystal with the (001) planes highlighted.
(Right) Representation of the reciprocal space with the diffraction angles *ω* (incidence angle of the x-rays onto the sample) and *2θ* (angle between the incident x-ray beam and the detector). The gray shaded areas are experimentally not accessible due to negative incidence or exit angles.

crystal [55]. Figure 2.1(left) shows the cubic crystal unit cell of silicon with the (001) planes highlighted in green.

The right graph in Figure 2.1 shows a representation of the reciprocal space. In diffraction measurements is probed by recording the intensity of the diffracted x-rays at a given coordinate in reciprocal space. The detector is placed at an angle of *2θ* relative to the incident x-ray beam. The angle at which the x-rays hit the sample is *ω*. Rocking curves (RC) are measured by varying the angle of incidence of the x-rays on the sample *ω*, which corresponds to a rotation around the origin of reciprocal space. Radial scans (or *ω/2θ*-scans*)* are made by changing *ω* and *2θ* simultaneously at a ratio of 1:2 (Figure 2.1, right). Maps of the Reciprocal Space (RSM) can be constructed by consecutive *ω/2θ*-scans with changing offset *δω*.

From Bragg's equation it is apparent that the smallest detectable strain, i.e. the variation in the lattice parameter *d*, depends on the dispersion and divergence of the incident x-rays and the spatial resolution of the detector. Rocking curves are measured using beam-shaping optics and an open detector. A secondary monochromator in front of the detector further increases the resolution in reciprocal space and a strain sensitivity of 10^{-4} can be achieved routinely. The secondary monochromator is used for the measurement of RSMs.

In the context of packaging-related problems RC measurements have been used previously to evaluate strain gradients close to bonding interfaces and to correlate the degradation during accelerated aging tests with changes in the strain level of MEMS components [56]-[58]. HRXRD measurements have also been made to evaluate strain in silicon MEMS caused by adhesives [57]-[59]. The warpage of silicon dies embedded in IC packages has been investigated by x-ray diffraction by mapping the width of the diffraction peaks over the surface of the chip, resulting in a qualitative distribution of the warpage in the device [60].

2.5 Finite element analysis

With the combination of finite element analysis and HRXRD, the understanding of the strain distribution can be further enhanced. Finite element simulations allow calculating the strain distribution throughout device but these theoretical results are based on a number of assumptions and estimated variables. Based on the deformation field obtained from the FEA, the reciprocal space maps can be calculated using the method developed by A. Schifferle which is described in detail in ref. [11]. The deformation gradient, which describes the local deformation at a given point, is first extracted from the FEA model. Then, using an Octave or MATLAB® routine, the individual components of the stress tensor and the rotation of the material at each node of the mesh can be evaluated numerically. In this way the scattering vector can be determined for each point in the mesh. Reciprocal space maps can then be constructed by applying a Gaussian broadening to each scattering vector and summing up the contributions from every node. Excellent qualitative and quantitative agreement between experimental measurements and simulations has been reported for micro-tensile tests on silicon specimens [11].

Due to the large depth at which the structures investigated in this work were located, absorption needed to be considered. In this work this was accounted for by considering the photoelectric absorption. A weight factor w was determined for each node based on the path of the x-rays scattered on the respective node based on the Beer-Lambert law [61]:

$$w = \frac{I}{I_0} = \sum_i e^{-\mu_i l_i} \tag{2.3}$$

where l_i denotes the path length of the x-rays through the i-th layer. The ratio I/I_0 is the loss of intensity of the x-ray beam due to the photoelectric absorption.

2.6 Radiation

After this discussion of the analytical methods, the environmental hazards relevant for space applications are discussed. The applicability of microsystems in space depends on their ability to operate reliably under the demanding environmental conditions imposed by the spacecraft's trajectory. Radiation induced degradation can cause severe impairment of the device performance. The tolerance of MEMS to radiation depends on the operation principle, the design and the material selection. In consequence of the multisided MEMS typology a wide range of radiation effects and tolerances has been reported and reviewed in [62]. The majority of degradation effects are caused by ionizing damage, especially charge trapping in dielectrics, and structural defects induced by non-ionizing energy losses (NIEL).

Charge trapping in dielectrics has been identified as a major radiation-induced cause of failure [62]. The accumulation of charges in insulating materials is a common reliability issue for many electrostatically operated MEMS that can also be induced by high electric fields.

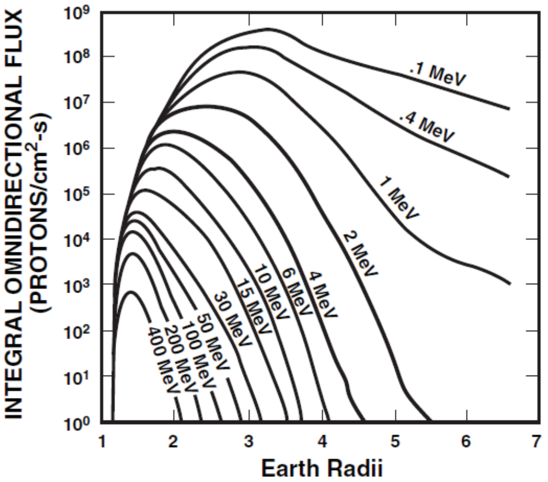

Figure 2.2: Proton fluxes versus elevation for various energies. From [67] after [65]. (© 2013 IEEE)

In both cases counteracting the effects of trapped charge is possible by following basic rules such as minimizing the volume of dielectrics in critical areas and by designing devices whose operation is insensitive to trapped charge [62]. This can significantly improve the reliability [63] but cannot eliminate material-specific limitations such as the degradation of the mechanical and electrical properties of the materials themselves. Appropriate material selection is therefore at the heart of engineering of reliable MEMS and is one of the main factors determining the performance and the failure modes of devices. However, fabrication process constraints and functionality requirements limit the choices. Possible candidate materials need to be evaluated in detail for their ability to perform under harsh environmental conditions. The performance of a material in microsystems may differ significantly from its properties in the bulk form or in integrated circuits. Consequently, the reliability of a material needs to be evaluated considering the system specificities and the qualification procedures must be defined accordingly.

There is no general threshold for the radiation tolerance of MEMS materials, as the radiation-induced damage will affect different parts of a MEMS device differently. The acceptable dose levels depend on the fabrication processes, the functional role of a material and the influence it exerts on the performance of the device.

In the following, relevant radiation conditions for space applications are summarized and considerations on the choice of radiation sources for MEMS reliability testing are made.

To illustrate the possible environments in space, consider a hypothetical flight to Mars. In its course the spacecraft is exposed to a variety of radiation conditions. These depend on the orbit, the space weather conditions and the solar activity [64], [65]. Near Earth charged particles trapped by the Earth's magnetic field dominate the radiation spectrum. In a spacecraft

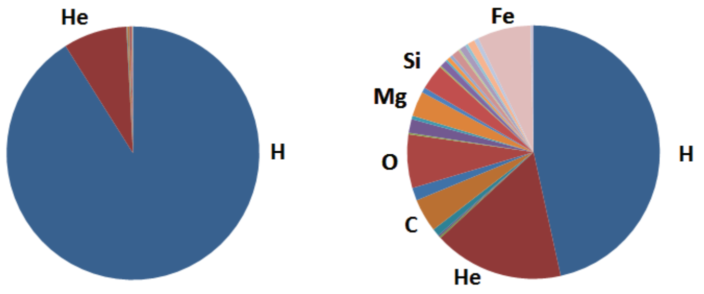

Figure 2.3: (Left) Relative abundance of elements in galactic cosmic rays. (Right) *Relative abundance* * Z^2 which illustrates the effect nuclear mass on the stopping power in materials. The elements are ordered after the nuclear charge *Z*. Data from ref. [68].

with a standard shielding thickness of 100-250 mils of aluminum (corresponding to 2.5-6.3 mm or, normalized by the material density, 0.7-1.7 g/cm^2) the dominating contribution to the absorbed dose comes from protons in the low Earth orbits (LEO) and electrons in the geostationary orbits (GEO) [62]. Proton energies lie in the range between 0.1 MeV and 400 MeV but the distribution of proton energies depends heavily on the orbit (Figure 2.2). The maximum energy of electrons is about 5 MeV and 7 MeV in LEO and GEO, respectively [65].

In the interplanetary regions the particle spectrum is dominated by the solar activity and galactic cosmic rays. Protons are the main species of solar flares and account for 90-95% of the particles [65]. The remaining portion of particle emission falls to heavier ions (mostly alpha-particles). Similarly, galactic cosmic rays are a mostly protons (85%) and alpha- particles (14%) and heavier ions contribute to less than one percent of the species. The energy of the galactic cosmic rays are significantly higher (GeV/nucleon) than for particles originating from the sun (MeV/nucleon) [68]. Although heavy ions only account for less than one percent of galactic cosmic rays their contribution to the total energy loss can be significant because the stopping power scales with the square of the nuclear charge (Figure 2.3) [68], [69]. Due to the high stopping power the heavy ions are an important source of single-event effects in electronic devices. However, most MEMS components do not rely on thin depletion regions or p-n junctions and hence can be considered to be insensitive to single-event effects [62].

2.6.1 Considerations on the choice of sources for MEMS radiation hardness assessment

The short overview given above shows that the main contributions to radiation damages are made by electrons, protons and electron-induced bremsstrahlung. The composition, flux density and energy of the radiation are subject to considerable variations over time and orbit, and radiation hardness assessment tests can only approximate the conditions in operation [65], [68].

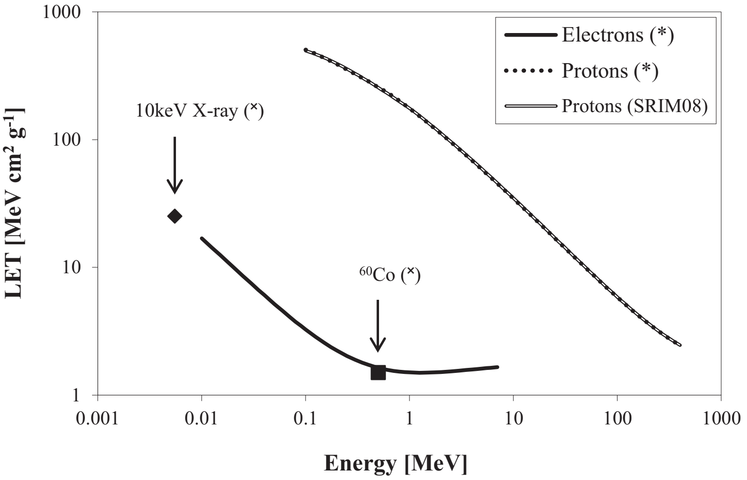

Figure 2.4: Electronic stopping power of protons, electrons and secondary electrons created by γ-rays and 10 keV x-rays. The figure is adopted from [67], [72] and is containing data from [67](×), [73](*), and SRIM-2008 calculations.

Figure 2.4 shows the linear energy transfer (LET) of different radiation types versus the particle energy. The LET denotes the ionizing energy deposited per unit length in the track of an impinging particle and is normalized by the material density. The energy ranges of the protons and electrons in the graph correspond to the energies observed in space [65].

A commonly used source of ionizing damage is γ-rays produced by the radioactive decay of ^{60}Co. The decay to ^{60}Ni occurs under the emission of photons with energies of 1.17 MeV and 1.33 MeV. Gamma-radiation induced damage is mainly caused by the Compton Effect leading to direct ionization and energy deposition by the secondary electrons. The secondary electron energy is in the range of 0.1-1 MeV [70], [71]. In devices where the radiation induced damage is correlated with ionization effects, the ^{60}Co γ-rays are expected to produce similar effects as electron irradiation because the spectrum of γ-ray induced secondary electrons closely resembles space-relevant electron spectra [67]. In analogy to this, 10 keV x-rays are expected to reproduce ionization-mediated degradations caused by ~10 MeV protons [74]. This hypothesis has been studied in detail in metal-on-silicon (MOS) devices, which are mainly affected by charge trapping in thin oxide layers. In ref. [66] and ref. [75] the threshold voltage shift of MOS transistors has been evaluated under irradiation with protons, electrons and ^{60}Co γ-rays at doses of up to 500 krad(SiO_2). While the radiation-induced change of the threshold voltage differed significantly between 41.4 MeV protons and γ-rays, a strong correlation between 10 keV x-rays and protons was found. These observations have been attributed to differences in the charge yield and in the electron-hole pair distributions [66]. The fraction of electron-hole pairs that escape the initial recombination in the first fractions of a second depends on the electric field in the material and the distribution of electron-hole pairs. Impinging particles with high stopping powers create a dense population of ionization events, whereas for lower stopping powers the mean distance between electron-hole pairs is larger. Therefore the charge yield is larger for radiation with lower stopping power than for radiation with higher stopping power and radiations creating similar distributions of ionization events affect irradiated specimen in a similar way. These experiments indicated that degradation effects due to ionization can be regarded as equivalent between ^{60}Co γ-rays and electrons with space-relevant energies because the two radiation sources have similar LET [66], [75].

Non-ionizing energy losses cause the displacement of atoms and the creation of vacancies and interstitials. These structural defects may be electrically active, influencing the carrier mobility and minority carrier lifetime. Displacement damage is predominantly caused by heavy ions and protons. The secondary electrons generated by ^{60}Co γ-rays usually carry enough energy to displace atoms from their lattice position and create recoils. The displacement damage induced by ^{60}Co radiation has been investigated theoretically on the basis of the energy distribution of secondary electrons created by Compton scattering of γ-rays [70], [71]. However, the NIEL obtained differed significantly between the two studies. The displacement damage factor ratio K_p/K_γ between 1 MeV protons and ^{60}Co radiation was found to be 2.4 in ref. [70] and 302 in ref. [71], but the reason for this discrepancy was unclear to the authors of the latter paper. In spite of this, if gamma-rays and protons are used for radiation testing a wide range of displacement damage rates are covered. It is also noted, the total displacement damage induced by electrons and γ-rays is orders of magnitude lower than proton-induced damages (Figure 2.5).

Heavy ions are less abundant but are important sources of single-event effects due to their large stopping power [68]. However, as mentioned above, the feature sizes of MEMS typically are on the micron-scale and the operation does not rely on thin depletion regions or p-n junctions. Therefore single-event effects are not expected to affect the devices [62] and hence heavy ion tests were not conducted.

A limited number of radiation sources and energies are used in the radiation tests, but the total dose absorbed over the device lifecycle has to be reproduced. The total ionizing dose (TID) absorbed by a space system shielded by 4 mm of aluminum is on the order of 1 krad/year in LEO and 10 krad/year in GEO [1]. The total dose level usually requested in the qualification testing of generic EEE parts is 100 krad [76]. For comparison, the expected ionizing dose of a tracking detector in the Large-Hadron-Collider (LHC) at CERN is 1 Mrad, obtained after 1.5 years of operation, which is much higher than most space doses [77].

2.6.2 Influence of radiation on Young’s modulus of structural MEMS materials

In this subsection the aging and degradation effects caused by radiation on quartz and state-of-the-art silicon resonators are summarized to give the reader an overview of the challenges

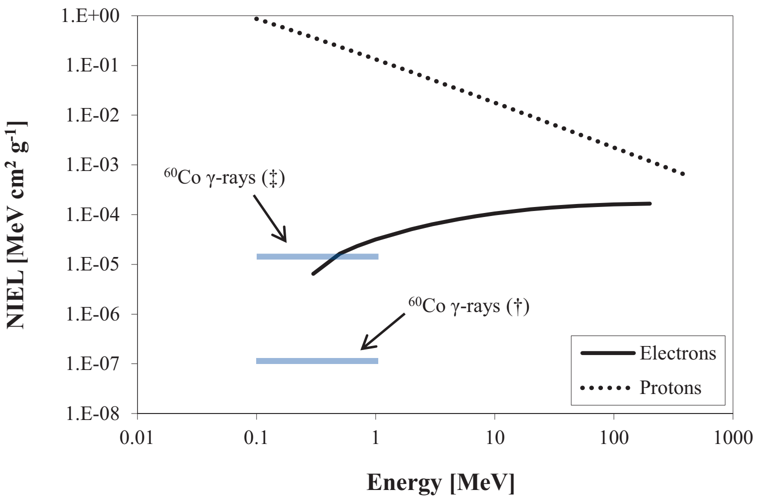

Figure 2.5: NIEL for electron, proton and ^{60}Co-radiation versus the particle energy. For ^{60}Co the energy of the secondary electrons is shown for the two refs. [70](‡) and [71](†).

related to radiation damage in micromechanical systems. A note to put the discussed frequency stabilities into context: As mentioned in the introduction, mechanical resonators can offer high stability and precision. However, depending on the specific requirements of the application, very different grades of precision are available. In quartz, these range from uncompensated crystals with a frequency precision of ±10 ppm and an aging of about 1 ppm/year to ultra-stable resonators where frequency stabilities of 0.2 to 1 ppm total over 20 years in space environments are achieved [78].

2.6.2.1 Quartz

Ionizing damage can lead to the motion and modification of impurities and point defects. Aluminum impurities are recognized to be the main reason for radiation-sensitivity of α-Quartz [7], [79], [80]. The aluminum can take the place of silicon in the crystal lattice and due to its lower valence it requires an additional electron to form four bonds with the neighboring oxygen atoms. This may be provided by compensators such as alkali metals (sodium or lithium) or hydrogen [81]. Ionizing irradiation causes these defects to be modified, for instance converted into more stable Al-OH and Al-hole centers. As a result, the elastic constants are changed, which becomes manifest in a resonance frequency shift of the resonator. The magnitude of this effect is dependent on the concentration of the aluminum impurities as well as the type of compensators in the crystal. Upon exposure to ionizing radiation the frequency shift increases and eventually saturates at a certain dose. The maximum frequency shift increases with higher aluminum concentrations in the samples.

A purification step by electro-diffusion at elevated temperatures can be applied to the quartz to remove or replace the alkali metal ions in the crystal [82]. These swept crystals show significantly lower radiation sensitivity. For instance, in ref. [79] several quartz samples with 0.2 ppm to 70 ppm Al were swept in presence of sodium, lithium and hydrogen and the effect on the radiation sensitivity to ^{60}Co gamma-rays was investigated. The measurements were made on AT-cut resonators at the upper turnover point (at about 26°C) where the slope of the frequency versus temperature is zero. In a sample with 60-70 ppm Al sodium-sweeping led to a relative frequency shift of up to 406 ppm and saturation was only reached at 7.4 Mrad. In a lithium-swept resonator with the same aluminum concentration a frequency shift of 3.4 ppm and a saturation dose of 4.7 Mrad were found. In contrast, in hydrogen-swept quartz with sub-ppm aluminum concentration only 0.3 ppm frequency variation was observed at a saturation dose of 1 Mrad. As these high-dose effects saturate, a pre-conditioning of the resonators at tens of krad is a possibility to reduce the radiation sensitivity. However, it has been noted that the short-term stability can be deteriorated by pre-use irradiations [78].

At low doses of ~0.1 krad the frequency variation is larger but is not correlated to the aluminum concentration and generally anneals out within hours to few days. The low dose effects were attributed to the converse piezoelectric effect in which the radiation-induced charge accumulation in the quartz leads to a build-up of a stress field in the resonator [80].

Displacement damage by neutrons leads to a stiffening of the crystal and hence an increase of the resonance frequency. The magnitude of this effect has been stated to be 5×10^{-21} cm^2/neutron for fluences between 10^{12} n/cm^2 and 10^{13} n/cm^2 [7].

2.6.2.2 Silicon

In [9] it has been reported that the resonance frequency of silicon micromirrors had changed shortly after proton irradiation of 1 MeV and 4.3 MeV protons and 100 Mrad total ionizing dose. After three weeks the devices had recovered the resonance frequency prior to irradiation. This observation was explained by the introduction of defects which were mobile at room temperature and therefore annealed out after the irradiation.

Surface-micromachined polysilicon resonator beams irradiated by gamma- and electron radiation have been investigated in [83], [84]. A decrease of the resonance frequency and an increase of resistance were observed. The results were attributed to a combination of displacement damage, injection annealing and thermal spike effects.

The effect of fast neutrons on the electromechanical properties of silicon has been studied recently by passive strain gauges and no variations of Young’s modulus were found within the experimental uncertainty (which was on the order of 10%) [85], [86].

Further efforts are clearly required in order to assess the reliability of single crystal silicon as a structural material for microsystems with resonant structures for applications with high radiation exposure levels. The experiments which were made on the radiation tolerance of silicon and SU-8 single-material resonators as well as piezoelectrically activated MEMS will be presented in Chapter 5 and Chapter 6, respectively.

2.7 Thermal effects

During a space mission very harsh thermal conditions can be encountered. After fabrication and acceptance of the flight model it is shipped to the Launch site by truck, airplane or ship. At the launch site it may have to be stored for several months depending on the launch schedule. For instance, the launch of the ESA Rosetta mission was delayed by about one year. To protect the spacecraft from the tropical weather (high humidity and salinity due to the proximity to the sea) it was stored under controlled atmosphere in a cleanroom[4].

After the launch the temperature is governed by the ratio at which energy is absorbed and emitted by the spacecraft. The sources for heating are mainly the radiation from the sun and radiation reflected and re-emitted from celestial bodies. At one astronomic unit (AU) from the Sun, which denotes the average distance of Earth from the Sun, the intensity of the radiation is as high as 1.4 kW/m^2. In low Earth orbits the albedo and infrared radiation emitted by Earth can further increase the intensity by several hundred W/m^2, whereas in GEO and further away from Earth these contributions are low. Variations in the exposure related to the spacecraft's orbit (distance to Earth and eclipses) add temporal components to the thermal balance. The solar radiation intensity decreases with the inverse square of the distance from the sun, and hence varies enormously between different planets in our planetary system. In addition, there are large differences between exposed and shadowed areas. For instance, on the surface of the moon the temperature varies between over 100°C to -170°C [87].

Many failure mechanisms in MEMS are related to the energy available for the formation, diffusion and aggregation of defects. The rates at which these processes occur are dependent on temperature (e.g. diffusion), humidity (such as for corrosion) and/or thermal cycles (e.g. fatigue and delamination at interfaces). Standard models for the influence of these parameters are given in Table 2.2. Increasing the respective parameters during a reliability test can be used to accelerate the related failure modes. Typical values for the activation energy lie between 0.3 to 1 eV [88]. For space qualification tests the European Cooperation for Space Standardization (ECSS) requests a 10°C temperature extension on the minimum and maximum temperatures encountered in a mission and 8 test cycles [89].

2.7.1 Temperature-related effects and aging in resonant microstructures

Elevated temperatures and temperature variations mostly are reversible but also lasting effects on the elasticity of materials are possible.

---

[4] [Online] http://www.esa.int/Our_Activities/Space_Science/Rosetta/Frequently_asked_questions (Accessed on 24. May 2014)

Table 2.2: Three models for the prediction of the influence of acceleration factors on the time to failure or number of temperature cycles to failure. Adopted from ref. [88].

Mechanism (Model name)	Time or number of cycles to failure	Acceleration factor	Comments
Temperature (Arrhenius)	$A_0 \exp\left(\frac{E_a}{k_B T}\right)$	$\exp\left(\frac{E_a}{k_B}\left[\frac{1}{T_{use}} - \frac{1}{T_{stress}}\right]\right)$	E_A = Activation energy A_0 = Constant
Temperature and humidity (Peck)	$A_0 RH^{-N} \exp\left(\frac{E_a}{k_B T}\right)$	$\left(\frac{RH_{stress}}{RH_{use}}\right)^N \exp\left(\frac{E_a}{k_B}\left[\frac{1}{T_{use}} - \frac{1}{T_{stress}}\right]\right)$	RH = Relative humidity [%] N: Humidity coefficient (~ -2.7)
Thermal cycling (Coffin-Manson)	$A_0 \Delta T^{-n}$	$\left(\frac{\Delta T_{stress}}{\Delta T_{use}}\right)^n$	ΔT = Temperature range (T_{max}-T_{min}) n: Temperature cycle coefficient (~2)

2.7.1.1 Quartz

Temperature variations near the operation range will influence a resonator due to the temperature dependency of the elastic constants. This can be minimized by a number of different strategies, of which the most common ones are temperature compensation and oven control (another strategy is the stress-based compensation mentioned above). The temperature coefficient of frequency should be as close to zero as possible in the targeted temperature range. For (uncompensated) SC-cut resonators as they are used in oven controlled quartz oscillators the frequency variation can be 0.02 ppm/°C in the range of ±25°C [7]. Temperature compensation is achieved by precisely measuring the temperature of the resonator and applying a correction to the oscillator output signal. Placing the resonators in a thermally isolated oven, ideally at a set-point above the maximum outside temperature, allows achieving high temperature stability. In doing so it is possible to keep the temperature of resonators within 1 mK in space environments in which temperature variations of over 100°C occur [90].

Hysteresis is a temperature-related effect limiting the stability of temperature compensated quartz oscillators (TCXO) to 0.01-1 ppm [7]. When the temperature of the resonator is cycled there is a frequency difference between the heating and the cooling traces. Retrace, which is closely linked to hysteresis is a shift of the resonance frequency after switching the resonator off and on. Several possible causes for hysteresis and retrace have been identified: Mass-transfer due to contaminations can significantly contribute to hysteresis effects but can be eliminated by hermetic and contamination-free packaging. Also stress relief in electrodes, the mounting structures and the package contribute to the hysteresis. In addition, the motion of impurities and lattice defects influence the thermal hysteresis by a modification of the elasticity of the quartz. In natural quartz larger hystereses were observed than in swept quartz which has much lower defect densities and lower defect mobilities [91], as discussed above.

Mass transfer and stress relief were found to dominate the aging behavior of quartz resonators [8].

The applicability of quartz in high-temperature environments is limited due to the transformation of the piezoelectric trigonal phase (α-quartz) into the hexagonal β-quartz phase at 573°C. However, already at lower temperatures the alpha-phase is subject to twinning, which degrades its piezoelectric properties and therefore the maximum operation temperature of quartz is generally limited to 350°C [92].

2.7.1.2 Silicon

The main drawback of single crystal silicon as a structural material for resonators is the sensitivity to temperature variations which results in frequency shifts of -28 to 30 ppm/K, depending on the crystal orientation [93]. Temperature stabilities rivalling these of temperature compensated quartz oscillators have been demonstrated in single crystal silicon resonators using a micro-ovenization and multipoint calibration, which resulted in a stability of ±0.05 ppm from -20°C to +80°C [94]. In addition, oscillators with ±0.2 ppm stability across the temperature range of -40 to +85°C and system performance characteristics meeting 4G and GPS specifications have been presented [95]. This oscillator also offers very low hysteresis of below 0.05 ppm in an 80°C range, which is similar to quartz TCXO resonators. However, the temperature compensation used suffers from higher power consumption than quartz oscillators. Miniaturization, and the consequential reduction of heat loss, has been proposed as a path for achieving low-power oven-controlled silicon oscillators [96].

In addition, the direct reduction of the TCF of MEMS resonators by material engineering is a way to reduce the heat losses and hence the power consumption. A very promising approach based on heavy doping has resulted in the demonstration of ±0.05 ppm/°C variation between 20°C and 100°C in a thermally activated silicon resonator [97]. Recently the first- and second-order TCF were measured as a function of the doping level in silicon doped by phosphorous, arsenic and boron, and parameters for nulling the first order TCF were obtained [98]. Another method to control silicon's TCF is to combine the silicon with a material that's TCF is of opposite sign, such as silicon dioxide. As a result, microresonators can be designed that have a turnover point at which the frequency versus temperature is zero. Such resonators are especially suited for oven-controlled systems as the turnover temperature can be adjusted by the geometry of the structure. At the turnover point a frequency stability of ±0.1 ppm was demonstrated over a period of more than one hour in Si–SiO_n resonators [99].

There are also indications that the aging of silicon resonators can compete with quartz. In electrostatically actuated silicon resonators hermetically sealed by an epitaxial polysilicon layer the frequency stability can reach yearly variations on the ppm or even sub-ppm level [100], [101]. One main difficulty in measuring the long-term stability of MEMS resonators are the fluctuations in the environmental conditions, especially the temperature. An approach to circumvent this problem is to place two resonators close to each other on the same chip. Both devices should be affected in the same way by fluctuations of the ambient temperature and it was demonstrated that the variations between two resonators were ±10 ppb over one month. Although such a setup cannot detect aging effects which affect both resonators in the same way, it gives an indication about the stability accessible in silicon resonators [102].

2.7.1.3 Aluminum nitride

Aluminum nitride is discussed here because it is a commonly used piezoelectric material for actuation of microresonators and is also the material utilized in the piezoelectrically activated silicon resonators investigated in this work (see Chapter 3 and Chapter 6).

Early results on aging tests performed on resonators made from stacked AlN and SiO_n were reported in [103]. After 15 thermal cycles between -50°C and 150°C the frequency drift of the resonators was below 15 ppm.

In [104] reliability studies on AlN-on-SiO_2 resonators were made in air and under vacuum during over 1200 hours. For the resonators stored in air a slow degradation of the resonance frequency of 50 ppm was observed. Higher drift levels were found in the devices stored in vacuum. However, ToF-SIMS analyses revealed silicone contaminations on these devices which originated from the vacuum system and were held responsible for the drifts. This underlines the importance of clean and hermetic packaging.

In refs. [105] and [106] the reliability of AlN-activated silicon microcantilevers was investigated. Single crystal silicon of 15 µm thickness and 200-1000 µm length was used as the bulk material of the cantilevers. The actuation was achieved using 1 and 1.4 µm thick AlN layers and CrNi electrodes. After high temperature storage at 130°C during 192 hours an increase of the resonance frequency (approximately 100-300 ppm) and the deflection amplitude was observed. This was attributed to an increase of the Young's modulus of the AlN layer. Operation of the resonators at elevated actuation voltages led to a continuous decrease of the resonance frequency, proportional to the applied voltage, and hence the resonance amplitude. This was related to cracks generated in the top electrodes due to fatigue. The amplitudes were large (up to 20 µm for 800 µm long resonators) and lifetimes of several years (~10^8 cycles) were predicted for sub-micrometer amplitudes. The dielectric constant of the AlN was found not to be affected by this accelerated resonant fatigue test.

Recently, the reliability of resonators which were thermally compensated by SiO_2 pillars in the silicon bulk and which were actuated by a thin film of piezoelectric AlN was analyzed. A shift of several ppm was observed in the first 10 days of accelerated aging at 100°C, but thereafter the frequency remained stable within 2-3 ppm (which was within the experimental uncertainty) during accelerated aging and also during thermal cycling in a 160°C wide temperature range [107].

2.8 Mechanical loads

Mechanical shocks and vibration may be encountered during assembly, transport and operation of MEMS devices. For space applications the most significant events occur during take-off and stage-separation of the launcher and during entry into the atmosphere and landing of the spacecraft. The required test levels for mechanical shocks are on the order of 2000 g and the vibration levels reach up to 40 g, depending on the frequency range and the weight of the device [108], [89] (also see Table 2.3). In military applications the mechanical shocks of up to 100’000 g are possible [109].

The failure modes related to such transient or oscillating mechanical accelerations are fracture, stiction and delamination [109]. Delamination and fracture are caused by occurrence of stresses which are higher than the fracture toughness of the materials or material interfaces. Stiction, short-circuits and micro-welding may occur if the relative displacement of structures becomes as large as their separation and they come into contact. After ref. [110] three main types of shock response can be distinguished:

- Impulse response: The rise and fall time of the acceleration is shorter than the acoustic transit time. The acoustic transit time depends on the speed of sound in the material and usually is below 0.1 μs. The pulse duration of external shocks (and also vibrations) typically lies between 0.1 ms and 1 ms. As the pulse duration is much longer than the time required for internal stress equilibration the dynamical effects are negligible.
- Resonant response: If the pulse duration is comparable to the period of oscillation of a natural mode, these resonances may be excited and hence significantly higher levels of deflection and stress are provoked.
- Quasi-static response: If the acoustic transient time and the oscillation periods are much smaller than the external acceleration time scale the system follows the acceleration as a whole.

In ref [111] this approach was extended by including experimentally determined geometric and dynamical properties of the system to quantitatively determine the amplitude and stress at a given acceleration level. In this approach the device under test is modeled by a 1-degree-of-freedom system that’s mass, damping coefficient and stiffness are evaluated by characterization under controlled actuation. The as-obtained parameters are used to predict the deflection at an arbitrary external shock or vibration. The model has been validated through tests on devices which were electrostatically actuated by comb-drives, and good agreement was found between the predicted and experimentally observed effects.

In many cases MEMS devices are in the quasi-static regime and therefore are not very sensitive to shock and vibrations. However, even under these circumstances failure can occur due to delamination of the MEMS from its substrate or fracture of the wire-bonds and hence shock and vibration testing should be an integral part of a qualification procedure.

2.9 Hermeticity

Hermetic packaging is of utmost importance to preserve the MEMS device and the electronic circuitry in a controlled environment. Pressure equilibration and moisture penetration can either be caused by molecules migrating through cracks, voids and channels in the package or by permeation through the materials [112]. Corrosion leads to various failure modes and is accelerated by the presence of moisture and water. It is therefore required to keep the moisture content inside a hermetic package below a level where condensation occurs as this significantly enhances corrosion. In addition, moisture increases absorption (changing the optical properties of the device) and favors capillary stiction [38]. The 'dew-point' is a parameter combining the temperature, pressure and moisture level which allows assessing whether water condensation is relevant. At ambient temperature the moisture content must not exceed 5000 ppm at 1 bar [113].

Measuring the hermeticity and leak rate in small packages is very challenging. Due to the small volume the leak rates must be extremely small to ensure low (partial and absolute) pressure changes over long periods of time. Pressure equilibration can either be driven by absolute pressure differences or by a gradient of the partial pressure of one or several components of a mixture of gases. To illustrate this, consider a container with a volume V and an initial internal pressure $p_{int,0}$ of 1 mbar. The outside of the container is an infinite-acting reservoir at a pressure p_{out} of 1bar. The pressure inside the package slowly equilibrates to the outside pressure according to an exponential law that's time constant is related to the leak rate l, the cavity volume and the initial pressure difference [114]:

$$p_{\text{int}} = p_{out} + \left(p_{\text{int},0} - p_{out}\right) e^{-\frac{l}{V\left(\left|p_{\text{int},0} - p_{out}\right|\right)} t} \tag{2.4}$$

The left graph of Figure 2.6 shows the influence of the cavity volume at a leak rate of 10^{-12} mbar l s^{-1}. For a cavity with an internal volume of 10^{-4} l (0.1 cm^{-3}) the internal pressure after 10'000 days (27 years) still is below 30 mbar. In contrast to this, smaller cavities of sub-microliter volumes may already reach pressure equilibration after few months or days at the same leak rate. The internal pressure inside a cavity of 1 mm^3 (1 µl) for various leak rates is shown in the right graph of Figure 2.6. This graph illustrates that in order to ensure low pressure levels over several years the leak rate must be below 10^{-12} mbar l s^{-1}.

The standard **Helium fine leak test** is not sensitive enough to measure such small leak rates. The minimum leak rate accessible with this test is about 10^{-10} mbar l s^{-1} [115]. However, various alternatives exist or are under development. Each of the possible methods has its advantages and drawbacks:

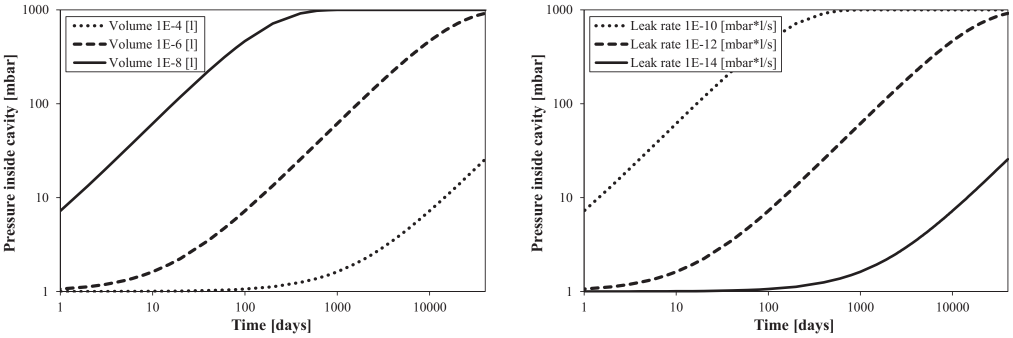

Figure 2.6: Evolution of the pressure inside a cavity as a function of time. The equilibrium pressure is 1 bar and the starting pressure inside the cavity is 1 mbar. In the left graph the leak rate is constant at 10^{-12} mbar l s^{-1} and the volume is varied while in the right graph the volume is constant (1 µl) and the influence of the leak rate is shown.

- **Residual gas analysis** is based on opening the package and measuring the escaping gases by means of a mass spectrometer. This allows identifying the composition and absolute amounts of gas in a cavity at partial pressures of 10^{-15} bar. A drawback of the method is its instrumental complexity and the fact that the test is destructive [116].
- The amount and composition of certain gases inside a cavity can also be measured by **Raman spectroscopy** (e.g. detecting N_2) or **Fourier Transform Infrared Spectroscopy** (FTIR), for instance detecting NO_2 and H_2S. Both techniques require optically transparent encapsulation. For FTIR spectroscopy the minimum leak rate sensitivity is on the order of 10^{-12} mbar l s^{-1}. Due to the large spot size of the FTIR spectrometers which is about 3 mm in diameter the method is not applicable to very small cavities [115], [117]. The NO_2 required for the FTIR measurement can either be introduced by encapsulation under controlled atmosphere or by bombardment of the cavities with the gas. Due to the difference in the pressure the gas will eventually penetrate into the cavity and lead to a detectable signal.
- This effect can also be used to build up pressure inside the cavity. If the device is capped by a membrane the pressure will cause it to deflect. This **membrane deflection** depends on the membrane size, shape, thickness and pressure difference. Although being very small (on the order of few nanometers) it may be detected by optical means such as white-light interferometry. The leak rate sensitivity is dependent on the geometry of the package but can be on the order of 10^{-12} mbar l s^{-1} or even lower [117]. Due to the low thickness of the membrane (≤ 100 µm) the encapsulation can be difficult and the mechanical stability of the package is limited.

- The presence of oxygen due to outgassing or leakage can also be measured by **chemical conversion**. Oxygen will react with metals to form oxides. In this process the optical transmittance of the material and its electrical conductivity will change. The leak rate can be determined by quantifying the amount and rate of the reaction [118]. Thin copper layers have been used to determine leak rates by measuring the optical transmission, and a leak rate sensitivity of 5 x 10^{-16} mbar l s^{-1} has been reported [119]. The difficulty with this method is related to the reaction rates. Obviously, it is required to avoid oxidation during the fabrication and packaging process. At the same time, the reaction rate after packaging must be higher than the supply of oxygen due to leakage and competing reactions. To increase the reaction rate of the oxidation the packages need to be heated to between 125°C and 150°C during several days [119]. Therefore this method may not be compatible with all types of MEMS.

A very promising method is the measurement of the **quality-factor of encapsulated microresonators**, which depends on the amount of air damping [120]-[122]. The detectable leak rates are very low ~10^{-14} mbar l s^{-1} [115]. Especially in small packages the correlation between quality factor and pressure is often complicated by the influence of the surrounding structures. While experimental calibration is possible, it is very desirable to develop and use theoretical models to predict the pressure dependency of the resonator [123]. The analysis of the air damping in wafer-level packaged piezoelectrically activated MEMS for leak rate measurements is discussed in Chapter 4.

2.10 Summary

In this chapter methods for investigating the Young's modulus and stresses in microsystems by HRXRD were presented and a selection of space-relevant environmental hazards, some of which were investigated in this thesis, was introduced. This comprised radiation damage, mechanical shocks and vibration, and thermal effects. In addition, the need for hermetic packaging of MEMS and the difficulty in assessing leak rates in small MEMS packages was briefly discussed. Additional effects which may pose challenges to reliability, but which would have exceeded the scope of this study are the storage and operation under non-ambient pressures (especially vacuum), the subjection to constant mechanical accelerations and microgravity or a combination thereof. In Table 2.3, an exemplary summary is given of the levels of exposure in space applications to the environmental hazards described above.

Together with the environmental hazards, the reported degradation effects in silicon and quartz resonators have been discussed. The maturity of the fabrication processes has allowed achieving major improvements of silicon resonators in recent years and the available data indicates that the reliability may be equivalent and possibly even superior to quartz. Moreover, promising results on the reliability of AlN-based resonators have been reported in literature. In the next chapters the contributions of this thesis to the reliability assessment of microsystems resonators are presented.

Table 2.3: Exemplary summary of environmental effects

Effect	Cause	Typical levels or requirements in space missions	Effects	Mitigation strategies	Main references
Radiation	- Ionizing and non-ionizing radiation originating from the sun or cosmic background radiation - Bremsstrahlung	- 1 krad/year in LEO and 10 krad/year in GEO of ionizing radiation dose [62]	- Charge accumulation in dielectrics - Modification of chemical structure and mechanical properties of materials	- No electrostatic actuation. - Avoid dielectrics in sensitive areas - Utilization of radiation-insensitive materials	[62], [65]
Mechanical shock and vibration	- Transportation - Launcher takeoff - Separation of launcher stages. - Spacecraft re-entry into the atmosphere - Spacecraft landing	- Up to 2000 g at 1-10 kHz [108] - Random vibration 12 g_{eff} at 2-2000 Hz [89] - Sinusoidal vibration: up to 20 g (0-peak) at 5-100 Hz [89]	- Fracture - Stiction - Delamination	- Avoid low-frequency resonances - Design for low mass or stiff springs	[110], [111]
Hermeticity / Leakage	- Storage - Operation	- Below 5000 ppm H_2O over the full life time (at 1 atm internal pressure) [113] - Leak rate which ensures maintenance of the pressure within the desired range	- Corrosion - Alteration of damping	- Use of getter - Bake out before wafer encapsulation - Use of materials with low moisture and gas permeability	[115], [38]
Thermal storage	- Non-ambient temperature during storage / operation	- Storage of several weeks to months after acceptance to launch - In-flight hibernation of several years (e.g. ESA Rosetta mission which was at approx. -55°C during 31 months [124])	- Premature failure due to accelerated aging - Defect migration and concentration - Corrosion	- Thermal isolation - Active thermal management	[87]
Thermal cycling	- Varying ambient temperature during storage / operation - Eclipses	- Temperature range of -87°C to -5°C on the surface of Mars [125] - Temperature of -233°C to +123° on the surface of Earth's Moon [125]	- Delamination - Cracking - Premature failure due to accelerated aging	- Avoid CTE mismatches - Thermal isolation - Active temperature control	[87], [89]
Mechanical deformation	- Exposure to mechanical forces (e.g. spring elements or systems on flexible substrates) - Residual stresses by adhesives	- Attachment needs to ensure long-term stability during launch and flight - Device-dependent	- Fracture - Fatigue - Strain relaxation		[38]

Chapter 3

Piezoelectrically Activated Silicon Microresonator – Design, Characterization and Residual Strain Analysis

In this chapter the basic principles of MEMS resonators are discussed. Thereafter the design and fabrication and the experimental setup for the dynamical characterization of the resonators investigated in this work are described. This is followed by the investigation on the residual strain analysis and the measurement of the packaging-related strains in the encapsulated devices.

A part of this chapter was published in T. Bandi, A. Dommann and A. Neels, *Proc. European Microelectronics Packaging Conf. 2013*, Grenoble, France, pp. 1-4 and in T. Bandi, J. Baborowski, A. Dommann, H. Shea, F. Cardot and A. Neels, *Proc. SPIE*, 2014, pp. 89750I (© 2014 Society of Photo Optical Instrumentation Engineers).

3.1 Basic concepts of MEMS resonators

Historically, the appearance of steels with constant elasticity over a wide temperature range such as Elinvar, has made it possible to fabricate tuning fork resonators with high frequency stability in the ppm-range [126], [127]. Nowadays quartz resonators are the state-of-the-art but competition from silicon-based microfabricated devices is growing due to the possibility of highly parallel batch processing, low fabrication tolerances, excellent material quality and high reliability as discussed in the last chapter. The most commonly used actuation principles used in MEMS resonators are capacitive, piezoelectric and electrothermal actuation [6]. Table 3.1 shows a comparison of various commercially available real time clock oscillators. The last two entries are developments made by CSEM and partnering institutions which are close to commercialization. The table shows that the trend of real time clock (RTC) oscillators is going towards low single-digit frequency stability, combined with ultra-low power consumption levels of 1 μW and below. In terms of power consumption and frequency stability AlN activated silicon resonators, based on the same technology as the resonators investigated in this work, are competitive in this segment.

Table 3.1: Comparison of Real-Time-Clock resonators with an output frequency of 32.768 kHz.

Manufacturer/Laboratory	Material	Frequency stability	Size [mm]	Power consumption	Ref.
Maxim Integrated	Not specified	±5 ppm	5.0x4.0x1.5	2 μA (2.3-5.5 V)	[5]
SiTime	Silicon	±10 ppm	1.5x0.8x0.55	0.75 μA (1 V)	[6]
Fortiming Corp	Quartz	±3 ppm / year	1.5 mm radius 9.4 mm length	1 μW	[7]
Silicon Labs	Silicon	±10 ppm	2x2.5 mm^2 footprint	1.7 mA (1.7-3.6 V)	[8]
Epson	Quartz	±5 ppm	3.6×2.8×1.2	0.35 μA (3 V)	[9]
Microcrystal	Quartz	±20 ppm	2.0x1.2x0.60	0.5 μW (max.)	[10]
Project Go4Time within EC FP7 research program (Quartz-resonator)	Quartz	±2 ppm	1.5x1.1x0.7 (targeted on wafer-level)	0.4 μA (1.0-3.3 V)	[128]
CSEM	AlN activated silicon resonator	±10 ppm	2.75x0.75*0.5 (resonator)	2 μA (1 V)	[129]

Micromechanical resonators can be modeled equivalently in the mechanical domain as well as in the electrical domain. The equivalent mechanical elements which capture the oscillatory properties of the resonators are a mass m, a spring with the spring constant k and a friction element with damping factor γ. In the electrical domain the resonators are described by a Butterworth-van-Dyke (BvD) equivalent circuit [130], [131]. A resistance R_s, an inductance L_s and a capacitance C_s are connected in series. In addition, a purely electrical capacitance C_p is connected in parallel to these three electrical elements to account for the capacitance between the actuation electrodes. The resonance frequency in such a system can be expressed as [6]

---

[5] [Online] http://www.maximintegrated.com/datasheet/index.mvp/id/6861 (Accessed on 04. Mar. 2014)

[6] [Online] http://www.sitime.com/products/32-khz-oscillators/sit1542#magictabs_2nwuQ_1 (Accessed on 04. Mar. 2014)

[7] [Online] http://www.4timing.com/specification/wxcp.pdf (Accessed on 04. Mar. 2014)

[8] [Online] http://www.silabs.com/Support%20Documents/TechnicalDocs/Si501-2-3.pdf (Accessed on 04. Mar. 2014)

[9] [Online] http://www5.epsondevice.com/en/quartz/product/rtc/serial3w/rx4574lc.html (Accessed on 04. Mar. 2014)

[10] [Online] http://www.microcrystal.com/images/_PDF/3_Crystal_Ceramic-Package/cm8v-t1a.pdf (Accessed on 06. Sep. 2014). According to the datasheed tighter frequency tolerances are available on request.

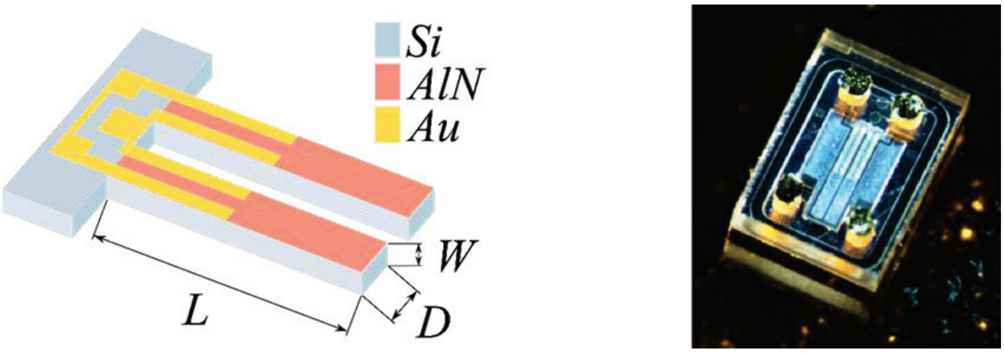

Figure 3.1 (Left) Schematic view of the tuning fork resonators (only the SOI device layer is shown). The length L of the resonators was 900 µm, the width W (normal to the direction of the oscillation) was 22 µm and the thickness D was 100 µm. (Right) Optical image of an encapsulated resonator. The size of the package is 1.5 x 2x 1.5 mm^3. Design and fabrication by CSEM (Div C) are gratefully acknowledged.

$$\omega = \sqrt{\frac{k}{m}} = \frac{1}{\sqrt{L_s C_s}} \,. \tag{3.1}$$

And the impedance Y is given by

$$Y(\omega) = i\omega C_p + \frac{1}{i\omega L_s + \frac{1}{i\omega C_s} + R_s} \,. \tag{3.2}$$

3.2 Resonator design, fabrication and electrical characterization

The resonators investigated in this work were tuning fork resonators based on AlN activated silicon resonator technology and were designed for pressure sensing in small cavities. The design and fabrication were not part of this thesis. Their mode of operation and functional layout were based on resonators presented by CSEM previously [130], [132], [133]. The resonators were fabricated on silicon-on-insulator (SOI) wafers and the fork tines were structured into the device layer by deep reactive ion etching. They had a length of 900 µm, a thickness (in the plane of oscillation) of 100 µm and a width of 22 µm. The width corresponded to the thickness of the SOI device layer together with the functional layers. A piezoelectric AlN layer with metallic top and bottom electrodes was used to drive the resonators. The devices were wafer-level packaged by eutectic bonding using a glass cap wafer with through-glass-vias, and the dies were then separated by diamond blade dicing. The left graph of Figure 3.1 shows a schematic view of the resonator. The right graph of Figure 3.1 shows an optical micrograph of a finished device. In the electrically active mode the tines oscillated in the plane of the wafer. Tuning fork resonators are commonly operated in the anti-resonance mode where the circuit impedance has a minimum. In the following this will be referred to simply as the resonance frequency.

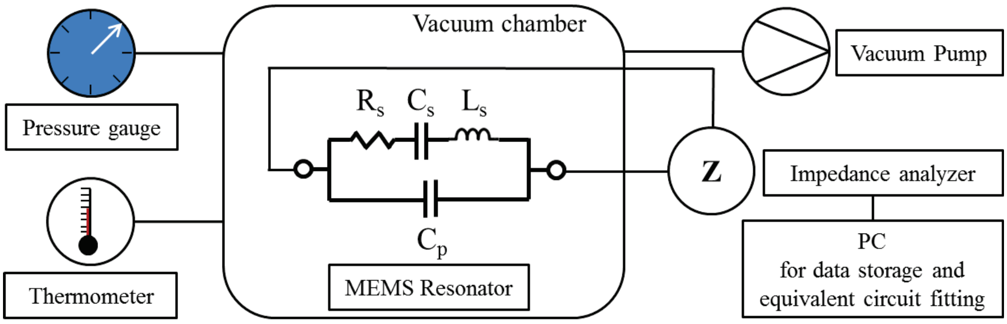

Figure 3.2: Schematic view of the measurement test setup.

The electrical characterization of the devices was made under controlled conditions using a measurement test setup as schematically shown in Figure 3.2. The impedance of the resonators was measured by sweeping the excitation frequency across the resonance and recording the impedance's absolute value and phase by a HP4192A impedance analyzer. A LabView™ program on a personal computer was used to control the impedance analyzer. From the impedance curves the four BvD parameters were extracted by non-linear fitting and were then used to calculate the resonance frequency and quality factor of the resonators.

The reliability investigations which are presented in this chapter and in Chapter 6, were made in packaged but non-hermetic devices under vacuum conditions ($p < 5 \times 10^{-3}$ mbar), in order to exclude the influence of air and to reveal the intrinsic performance of the resonators. The pressure sensitivity and leak rate sensitivity will be discussed in Chapter 4. Figure 3.3 shows a measurement of the phase and magnitude of the impedance of a tuning fork resonator near the operation frequency. The fitted curve of the BvD equivalent circuit is shown in the same graph. Good fits were obtained near the anti-resonance where the amplitude of the impedance had a minimum. At the resonance where the two tines moved in phase and the electrical impedance was at a maximum, the fitted line deviated from the experiment. This was related to parasitic elements in the circuit and the fact that the impedance was close to the specified limit of the impedance analyzer. However, as note earlier, the tuning fork resonators are commonly operated in the anti-resonance mode where good agreement between the fit and the measurements was obtained.

Throughout the measurements the temperature and pressure of the chamber were monitored. The temperature dependency of the resonance frequency was -3.5(±0.5) Hz/K while no temperature dependent variation of the quality factor was observed. A correction was applied to the resonance frequency, normalizing it to a reference temperature of 25°C. Neither the resonance frequency nor the quality factor was affected by a DC bias (up to ±5 V).

The measurement repeatability was composed from contributions from the error of the measurement technique, the fitting procedure and the variations of the experimental conditions

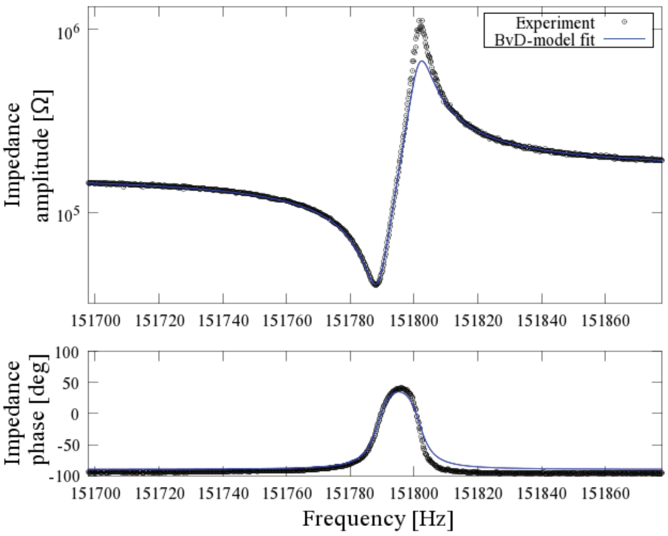

Figure 3.3: Impedance absolute value (above) and phase (below) of the resonator near the operation resonance frequency. The black circles are the measurement points and the blue line is a fit of the Butterworth-van-Dyke equivalent circuit.

(e.g. humidity, temperature). For the purpose of evaluating the repeatability uncertainty of the experiments the impedance characteristics of 34 devices was recorded three times with one week time between the measurements. The pooled standard deviation of the resonance frequency was 1.2 Hz, corresponding to 11 ppm. The repeatability uncertainty of the quality factor was 450.

During the proton irradiation tests (see Chapter 6) another impedance analyzer was used (Agilent 4292A). The repeatability uncertainty of this setup was inferior to the other setup due to a lower frequency resolution (2.5 Hz instead of 0.2 Hz). The repeatability uncertainty of the resonance frequency and the Q-factor were estimated to be 75 ppm and 2500, respectively.

3.3 Structural analysis of piezoelectric AlN layer

Hermetic encapsulation is a critical requirement for reliable microsystem because humidity may condensate, causing corrosion [113]. As outlined in section 2.9, monitoring the pressure inside small cavities is challenging and traditional methods such as Helium fine leak tests are not sensitive enough for many microsystems [115]. Miniaturized pressure sensors integrated in small packages could allow monitoring the inside pressure and pressure evolution even in cavities with internal volumes below 1µl. MEMS resonators with pressure-sensitive Q-factor are a promising technology to achieve this goal [133], [134]. Nevertheless, the resonance characteristics and aging properties depend not only on the vacuum level but

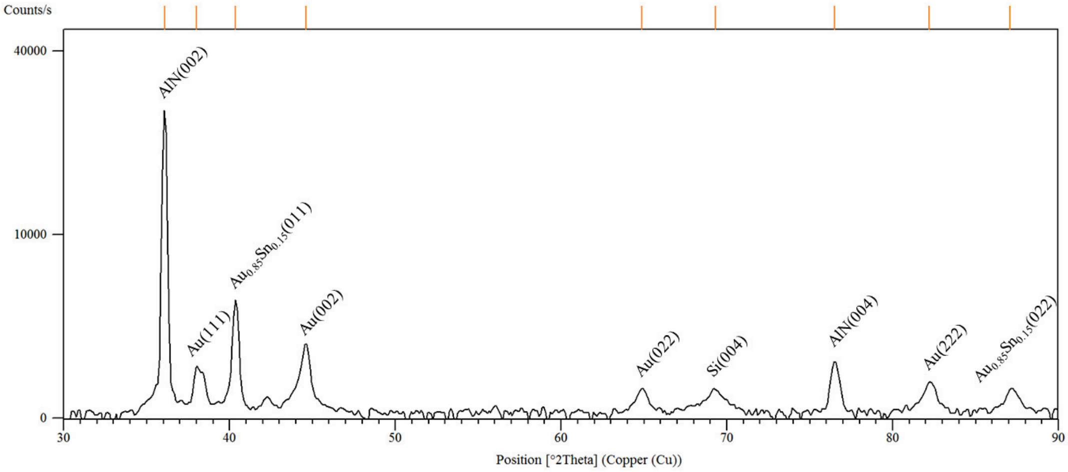

Figure 3.4: X-ray diffraction pattern of the silicon resonators without a cap.

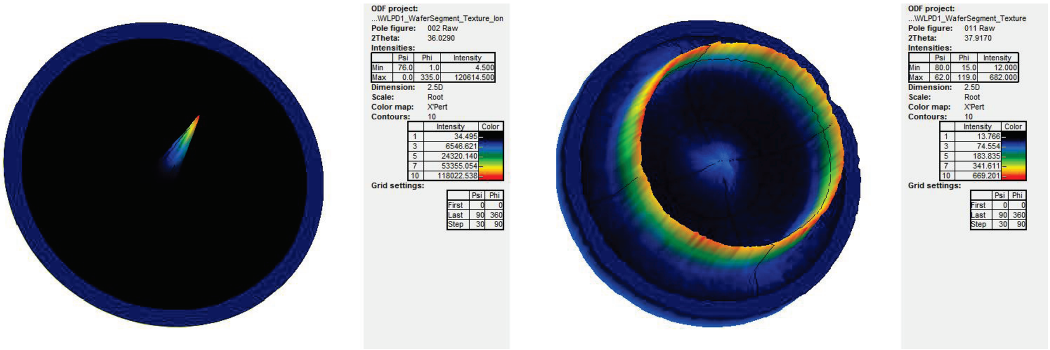

ODF project: ...\WLPD1_WaferSegment_Texture_lon
Pole figure: 002 Raw
2Theta: 36.0290
Intensities:

	Psi	Phi	Intensity
Min	76.0	1.0	4.500
Max	0.0	335.0	120614.500

Dimension: 2.5D
Scale: Root
Color map: X'Pert
Contours: 10

	Intensity	Color
1	34.495	
3	6546.621	
5	24320.140	
7	53355.054	
10	118022.538	

Grid settings:

	Psi	Phi
First	0	0
Last	90	360
Step	30	90

ODF project: ...\WLPD1_WaferSegment_Texture
Pole figure: 011 Raw
2Theta: 37.9170
Intensities:

	Psi	Phi	Intensity
Min	80.0	15.0	12.000
Max	62.0	119.0	682.000

Dimension: 2.5D
Scale: Root
Color map: X'Pert
Contours: 10

	Intensity	Color
1	13.766	
3	74.554	
5	183.835	
7	341.611	
10	669.201	

Grid settings:

	Psi	Phi
First	0	0
Last	90	360
Step	30	90

Figure 3.5: Pole figures of AlN(002) and AlN(011). The *c*-axis is highly oriented out of the wafer plane, while the AlN(011) diffraction peak shows a circular symmetry. This is characteristic for a fiber texture.

also on the stress state of the resonant structure, which in turn is influenced by the packaging process. Therefore a detailed analysis of the strains present in the system is required to evaluate their influence on the device performance.

For efficient piezoelectric actuation the AlN layer must be highly textured. Phase analysis and texture measurements were carried out on a PANalytical X'Pert PRO MRD instrument using copper K_α radiation. It was used in a parallel beam configuration and was equipped with a Göbel x-ray mirror and a 6-axis goniometer. The diffracted x-rays were counted by a xenon point detector. Figure 3.4 shows the diffraction pattern of the resonators. Only the AlN(002) and AlN(004) peaks were present in the diffraction pattern, which indicated a strong texture along the *c*-axis of the hexagonal AlN. This was in agreement with expectations, as the AlN was reported to grow in its hexagonal phase with a preferred orientation along its *c*-axis on amorphous silicon oxide and on (111)-oriented Pt, Al and Ru [135].The

Table 3.2: Material parameters used for the data analysis and FEA simulations. The

Material	Young's modulus [GPa]	Poisson's ratio	Coefficient of thermal expansion [ppm K^{-1}]	Density [g cm^{-3}]	X-ray mass attenuation coefficient (8 keV) [mm^{-1}]	Ref.
AlN	315 [136]	0.245 [136]	4.35 [137]	3.26 [137]	20.5 [138]	
Silicon	Orthotropic	Orthotropic	2.6	2.329	14.5 [138]	[139]
SiO$_n$	57 [140]	0.2 [10]	0.5 [141]	2.2 [140]	6.4 [138]	
Au-Sn eutectic	69	0.4	16.8	14.7	347 [138]	[142]
Pyrex	72.9	0.208	2.4	2.51	7.3 [138]	[11]

metallic electrodes and the bonding gold-tin solder also appeared in the diffractogram. It is noted that the diffraction peaks of the cubic metals of the Under-Bump-Metallization superpose. The high degree of texture in the AlN was confirmed by pole figures (Figure 3.5). The AlN(002) peak was fully oriented out of the wafer plane, while for the AlN(011) a circular symmetry was observed. This is a clear proof for a fiber texture. The width of the rocking curves (ω-scan) is linearly related with the piezoelectric coefficient of AlN [143]. In the investigated devices the rocking curve full width at half maximum (FWHM) was 1.8° which is comparable to state-of-the-art AlN layers.

The residual in-plane stress in the AlN was determined from the out-of-plane strain. The average size of the *c*-parameter of the hexagonal lattice was obtained from the angular positions of symmetric AlN(004) and AlN(006) diffraction peaks. High-angle reflections were selected because the strain resolution is given by $\Delta d / d = \Delta\theta / \tan(\theta)$ and hence increases at higher diffraction angles. The lattice constants were compared to reference values of unstrained AlN reported in literature ($a = 3.11197(2)$ Å and $c = 4.98089(4)$ Å [144]) to calculate the out-of-plane strain. For biaxial strain the in-plane stress $\sigma_{in-plane}$ is related to the out-of-plane strain $\varepsilon_{out-of-plane}$ by [145]

$$\sigma_{in-plane} = \varepsilon_{out-of-plane} \frac{(1-\nu)}{2\nu} E \tag{3.3}$$

where ν and E are the Poisson's ratio and the Young's modulus of AlN, respectively. These material parameters were obtained from literature and are listed in Table 3.2. It is noted that ideally the angular position of asymmetric peaks would be used in addition to the symmetric

---

[11] [Online] http://cmi.epfl.ch/organisation/files/D263T_d.pdf (Accessed on 06. Jul. 2014)

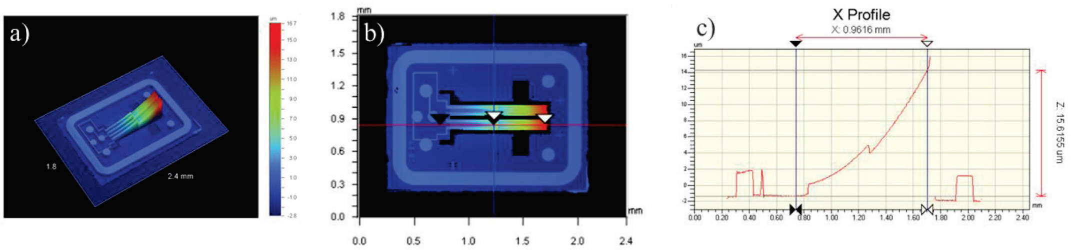

Figure 3.6: Deflection measurement of the tuning fork resonators measured by white-light interferometry. (Left) Pseuo-3D view of the topography of an open resonator the color indicates the height. The center graph shows a top view of the topography and the right graph shows the height profile along one tine of the tuning fork.

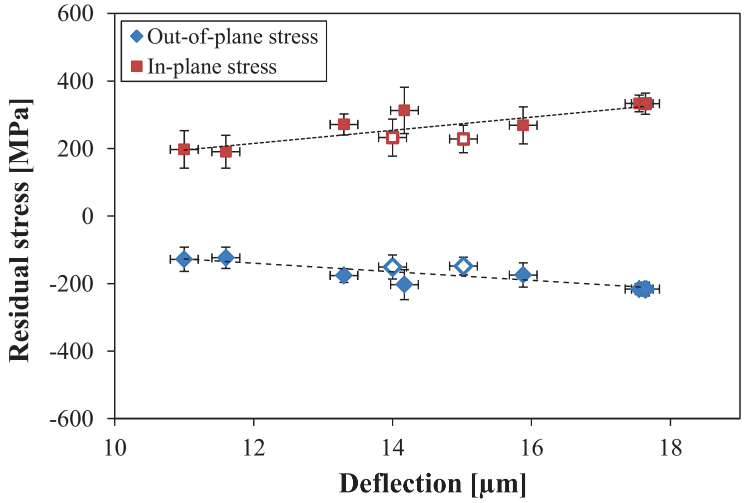

Figure 3.7: Residual strain in the AlN layer versus the deflection of the resonator beams. The open and filled markers are devices from two different wafers. The lines are guides to the eye.

diffraction peaks to directly access the in-plane lattice constant [145]. However, due to the generally decreasing intensity of high-angle reflections, the fiber texture and the small probe volume the respective diffraction peaks were not intense enough to allow for a sufficiently precise determination of the diffraction angles.

A second method to investigate the strain in the devices was the bending of the resonators, which acted as a passive strain gauge. The deflection was measured using a Wyko NT1100 white-light interferometer. An example profilometry measurement is shown in Figure 3.6. The deflection was determined by the sum of the strains in all functional layers, most notably the AlN and the silicon-oxide. Figure 3.7 shows the residual stress versus the resonator beam deflection. As expected, higher tensile residual stresses were correlated to higher deflections of the resonator beams. The measured stress levels were consistent with values reported in

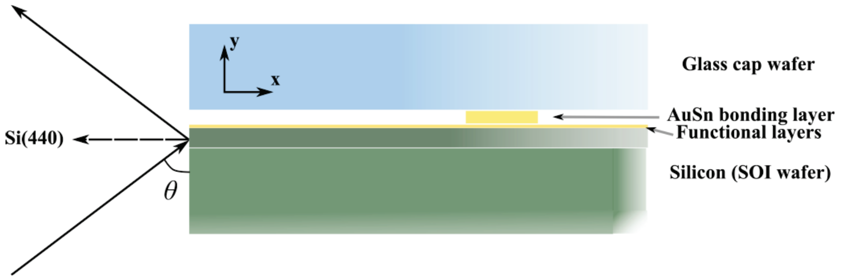

Figure 3.8: Schematic cross-section of the bonding interface region and the HRXRD measurement configuration. The microresonator is fabricated in the device layer of the SOI wafer. Note that the image is not to scale; the thickness of the bonding layer is about 5 µm and the distance to the package surface is about 100 µm.

literature. For instance in ref. [143] stress levels between +2 GPa and -10 GPa were reported and only at stress levels in excess of -1.8 GPa delamination occurred. The slopes of the in-plane stress and out-of-plane stress versus deflection were 19.7±6.4 MPa/µm and -12.8±4.2 MPa/µm, respectively. While the latter is directly based on measurements, the in-plane stress was calculated using the Poisson's ratio and the Young's modulus of AlN, which were 0.245 and 315 GPa as given in ref.[136].

Investigations on the mechanical properties of the metallic layers by scratch tests and nanoindentation have been performed. A good homogeneity of the mechanical properties (hardness, elasticity and scratch resistance) of the devices prior to bonding has been found. The sealing rings were investigated prior to bonding and after bonding by polishing cross-sectioning, SEM and EDX and were found to be composed by about equal parts from of the Au_1Sn_1 phase (δ-phase) and the $Au_{0.85}Sn_{0.15}$ phase (ζ-phase). These results have been reported on in more detail elsewhere [146]. In addition, mechanical tests of the strength of the sealing rings (Pull test and shear test) have been conducted. The fracture has been observed to occur almost exclusively in the glass, indicating a high strength of the sealing after bonding. Detailed accounts of these experiments can be found elsewhere [147].

3.3.1 Packaging strain investigation

To investigate the influence of the packaging process on the strain distribution, a measurement setup which is applicable to both open and capped devices was required. For this purpose the Si(440) reflection was selected. The corresponding atomic planes were parallel to the sidewalls of the devices and hence it was possible to directly access the in-plane strain in the silicon. Figure 3.8 shows the resonator package and a schematic view of the diffraction geometry used to investigate the bonding interface between the resonator device and the glass cap.

The HRXRD measurements were carried out on a PANalytical X'Pert PRO MRD instrument using copper $K_{\alpha 1}$ radiation. It was used in a parallel beam configuration and was equipped

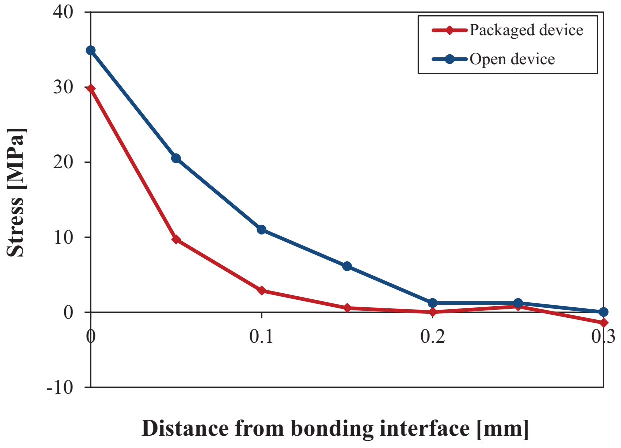

Figure 3.9: Stress gradient in mechanical devices.

with a Göbel x-ray mirror and a Bartels 4-crystal monochromator. The diffracted x-rays were counted by a xenon point detector. For the RC measurements an open detector was used. A secondary monochromator in front of the detector was utilized for the RSM measurements.

At first, mechanical devices were investigated by HRXRD. The mechanical wafers followed essentially the same fabrication process as for the functional devices, but without carving out the resonator. In Figure 3.9, the results of x-ray rocking curve measurements are shown. Using a beam width of 50 µm, rocking curves were measured at different positions along the devices sidewalls. At the bonding interface a stress level of 35 MPa was determined for the open devices. After bonding, the stress level was slightly reduced to ~30 MPa. The strain state in the devices was thus dominated by residual stresses in the functional layers deposited during fabrication and the packaging caused only a small reduction of the overall stress level.

As discussed in section 3.2, the functional devices were based on SOI wafers where the resonator structures were etched into the device layer. In SOI wafers the device layer and the handle wafer are two separate monocrystals, separated by a thin layer of amorphous SiO_n, and are generally not perfectly aligned. In the diffraction measurement their peaks were therefore offset in reciprocal space and the handling wafer could be used as an internal reference. Figure 3.10 shows a typical reciprocal space map of an open device. The diffraction peaks of the substrate and the device layer were offset by about 0.5 degree in the y-axis (Omega) which corresponds to a rotation of the crystal. The horizontal axis denotes Omega/2Theta which is related to the spacing of the atomic planes (d_{440}-spacing). Consequently, strain and strain gradients can be monitored. The substrate peak had a low FWHM (~0.006° in $\omega/2\theta$ and ~0.005 in ω). This is comparable to the reference value measured in bulk silicon, which indicated that the handle wafer was unstrained. The diffraction peak of

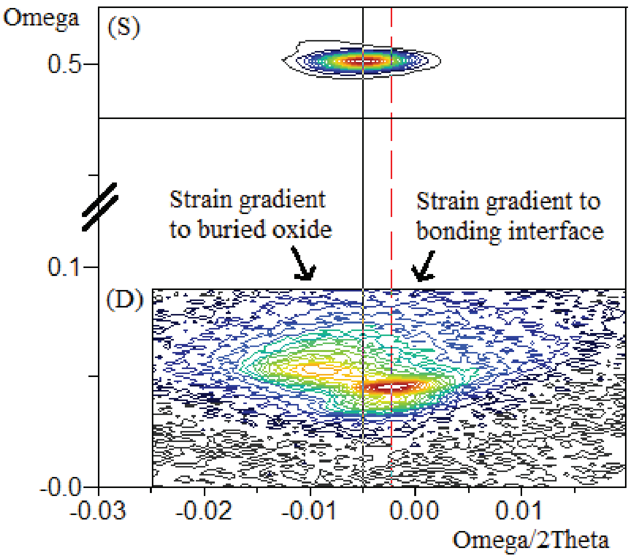

Figure 3.10: HRXRD RSMs of the bonding interface of an open resonator. *Omega* and *Omega/2Theta* axes show degrees on a relative scale. The upper peak is the diffraction peak of the handling wafer (S) and the peak at lower Omega values is the diffraction signal of the device layer (D). The diffraction peak of the device layer exhibits a strain gradient related to the strain gradients towards the buried oxide on one side and the functional layer on the other side.

the device layer exhibited a strain gradient related to the different strain levels at the interfaces with the buried oxide on one side (hereafter denoted SOI_{bottom}) and the functional layer (SOI_{top}) on the other side. In addition, a tilting component between the two interfaces was observed. The black vertical line in the RSM shows the position ($\omega/2\theta$ value or *d*-spacing) of the substrate wafer and the red dashed line denotes the position of the diffraction peak of the device layer towards the functional layers (SOI_{top}). The strain gradient between the two peaks (substrate-SOI_{top}) was related both to the strain distribution in the functional layers as well as the bonding-induced strains, as will be shown below.

In Figure 3.11, a comparison of the measured reciprocal space maps of three open resonators with different beam deflections are presented. With increasing resonator deflection the strain gradient between the substrate and the device layer went over from negative to positive. This means that for low deflections a tensile strain was present in the silicon near the functional layers. Higher tensile residual stress in the functional layers was correlated with a shift of the SOI_{top} diffraction peak to higher angles, and hence compressive stress in the silicon. In contrast, the strain gradient between SOI_{bottom} and the substrate wafer was constant.

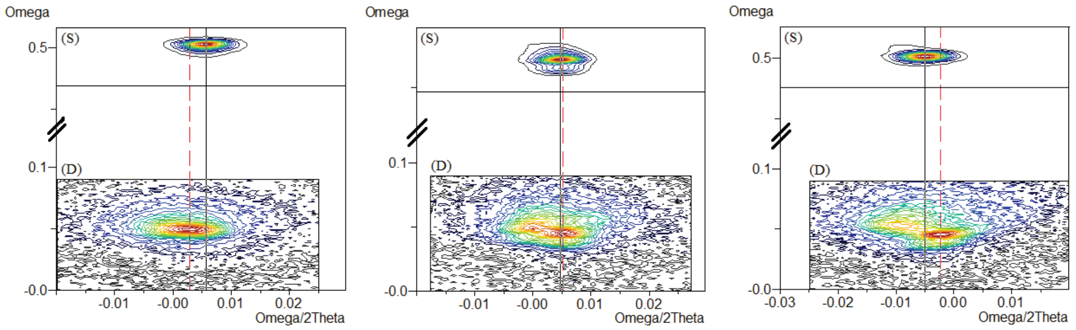

Figure 3.11: Comparison of three RSM’s measured on open resonators. *Omega* and *Omega/2Theta* axes show degrees on a relative scale. The three devices differ in the deflection of the resonator beams, and hence the strain in the functional layers. From left to right the deflection (and residual in-plane stress in the AlN) of the resonators was 11 µm (195 MPa), 13.3 (270 MPa) µm and 17.6 µm (335 MPa).

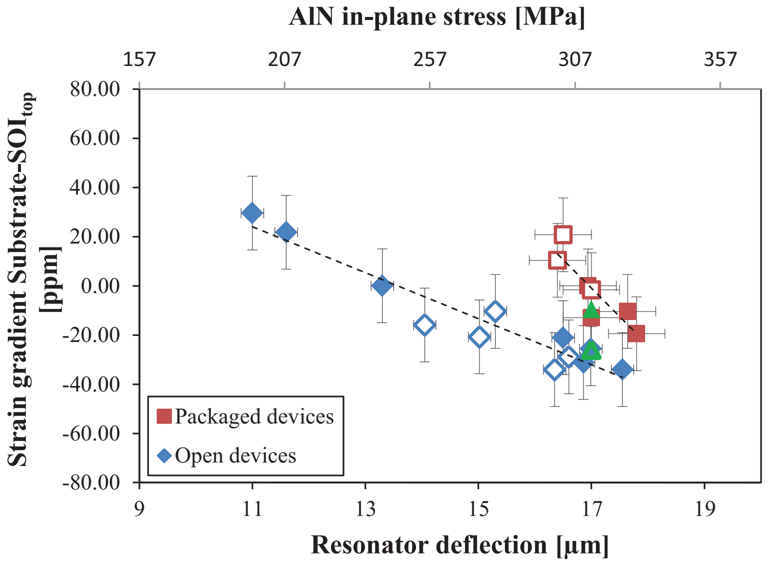

Figure 3.12: The strain gradient between the substrate and SOI_{top} for open resonators (♦) and packaged resonators (■). The green markers (▲) show the strain gradient of a packaged device (upper point) and after removing the cap (point at more negative strain gradient). The filled and empty markers are samples from two different wafers, respectively. The lines are guides to the eye.

For the purpose of clarifying the dependence of the strain distribution to the packaging and the properties of the functional layers, a series of open devices and packaged devices originating from two different wafers was measured. The strain gradient between the substrate and SOI_{top} is shown in Figure 3.12. A clear correlation between the resonator deflection and the peak separation was found in the open devices. In the packaged devices a trend with the deflection was also observed present but the available samples did not allow determining a clear relationship. In addition, the error on the deflection measurement was rather large (about ±1 µm as estimated from the variation between repeated measurements) as it had to be determined by compensation of the glass caps in the white light interferometry, which deteriorated the measurement repeatability.

The results presented in Figure 3.12 show that the strain gradient in the devices was related both to the residual stress in the functional layers as well as the strain induced by the packaging. This was also clearly demonstrated by measuring the strain distribution in a device both in the packaged state and after removal of the cap (green markers in Figure 3.12). For the open devices the slope of the strain gradient versus deflection relationship was 9.3±0.9 ppm/µm and for the strain gradient vs. in-plane stress the slope was 0.48±0.05 ppm/µm. In the packaged devices a shift towards more tensile strains by about 20 to 40 ppm was found. Nevertheless, these stress levels were low enough not to significantly influence the resonance frequency of the resonators. In over 20 devices investigated in the radiation tests (see Chapter 6), no significant correlation between the deflection and the Q-factor or the resonance frequency was found. The frequency variations were within the range estimated from the fabrication tolerances (~ 1 µm).

3.3.2 Finite element analysis of packaging strains

A simplified 2D model was implemented in COMSOL Multiphysics® and was used for the analysis of the strain distribution in the open and the packaged devices. The two-dimensional model corresponded to a cut through the center of the device and was discretized using tetragonal elements. The structure of the resonators was simulated using an orthotropic elasticity tensor for silicon and isotropic elasticity for the other materials. The material properties used as an input to the simulations are listed in Table 3.2. The simulation was made using the solid mechanics module and consisted of a stationary solution with a temperature equilibration and initial in-plane stresses and strains. The starting and end temperatures were 280°C and 20°C, respectively, which corresponded to the bonding process, i.e. the temperature difference between the solidification temperature of the gold-tin eutectic and room temperature. Due to the large difference in the aspect ratio between the bulk silicon and glass wafers and the functional layers only the main functional layers (SiO_n and AlN) were considered while the metallic electrodes were neglected. Boundary conditions which had minimal influence on the strain distribution were selected. One corner on the backside of the devices was fully constrained while the motion of the other corner of the backside was restricted in the y-direction to avoid a rotation of the device. The mesh consisted of 88k and 125k triangular elements for the open and the capped devices, respectively. Biaxial strains in the functional layers were imposed at the start of the simulation. Their magnitude was varied to investigate the influence of individual parameters on the strain distribution and the diffraction pattern. After convergence was attained the deformation gradient was extracted and the reciprocal space maps were calculated, including the photoelectric absorption effect

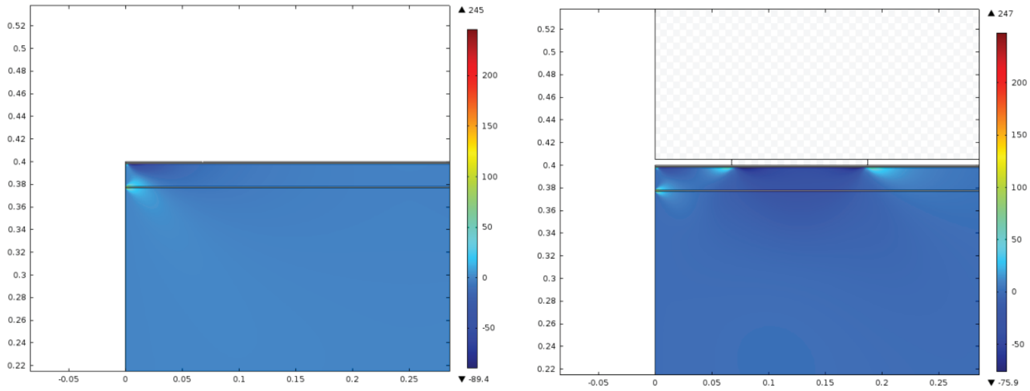

Figure 3.13: Finite element model of the MEMS package. The graphs show a cross-section of the bonding interface region (scale: millimeters). The color indicates the value of the *x*-component of the stress in the silicon after convergence of the simulation (in MPa). The left graph shows an open device while the right graph shows a device with a cap, which changes the strain distribution in the device layer. For clarity the cap and the sealing ring are highlighted by a checkerboard pattern. The x-components of the strain in the SiO_n and the AlN were -300 MPa and 750 MPa, respectively.

as outlined in section 2.5. The x-ray mass attenuation factors μ_i of the materials are given in Table 3.2.

The initial parameters in the simulation were the following. The biaxial in-plane stress in the SiO_n layer was compressive and was varied between -100 MPa and -500 MPa. These stresses originate from the mismatch of the coefficient of thermal expansion between silicon and the SiO_n. The simulated values fully covered the range of experimentally determined values which lie between about -200 MPa and -400 MPa [141], [148], [149]. The in-plane stress in the AlN was simulated between 0 MPa and 2000 MPa. The distance between the surface and the sealing ring was about 65 µm, and the width of the sealing rings was 120 µm.

Figure 3.13 shows the simulated strain distribution in the MEMS package. No significant difference in the maximum stress level was found. However, in the packaged device the strain induced by the sealing ring and the cap were visibly altering the strain distribution. The strain distribution change related to the bonding was localized within a distance of about 100 µm away from the sealing rings and therefore the bonding did not directly influence the tuning fork resonators. This was also confirmed by the experiments where no significant difference of the pressure vs. Q-factor dependency was observed between the packaged and the open devices (see Chapter 4).

In Figure 3.14 a comparison of the experimental measurement and the simulation of the RSMs is presented for a MEMS device which was measured both in its capped state and after removal of the cap. The strain gradient between the encapsulated state and after removal of the cap were already shown in Figure 3.12 and discussed above. The color maps of the experiment and the simulations were equal, i.e. linear for the substrate peak and square-root

Opened device

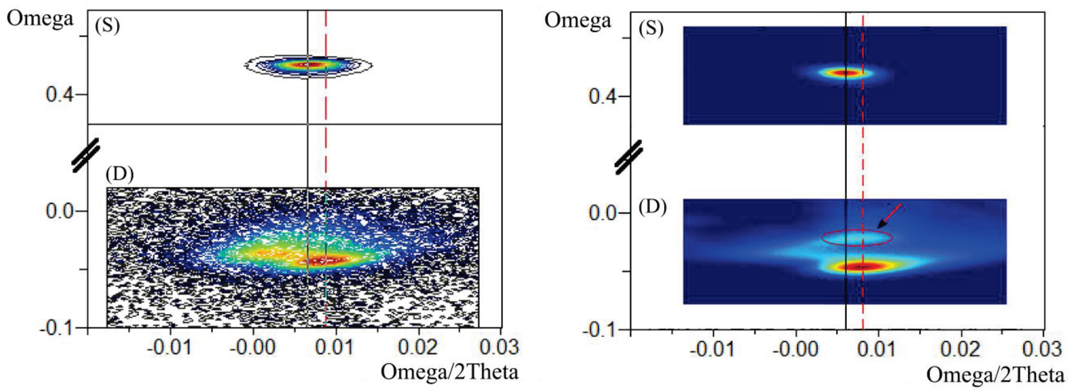

Packaged device

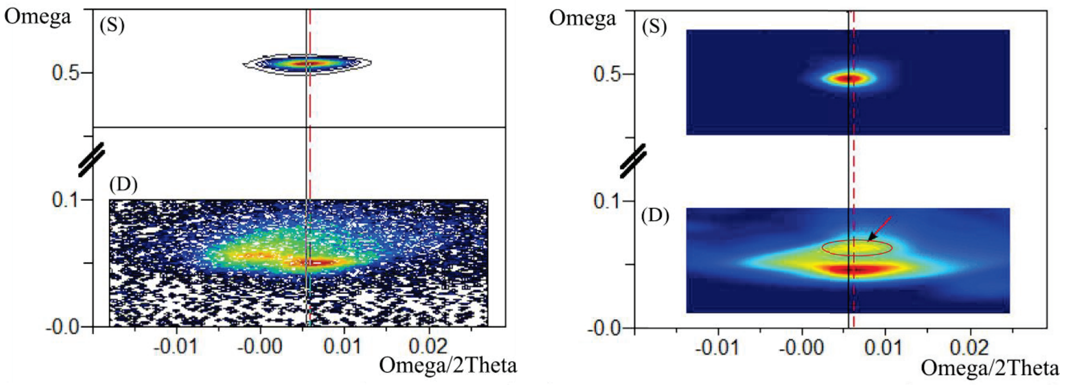

Figure 3.14: Comparison of the experimental and simulated RSM's for a device which was packaged (lower two graphs) and then opened (upper two graphs). *Omega* and *Omega/2Theta* axes show degrees on a relative scale. The scale of the color map is on a linear scale for the substrate layer (S) and a square-root scale for the device layer (D). The vertical black solid line and red dashed line show the $\omega/2\theta$ position of the substrate and the SOI_{top}-peak, respectively. The x- and y-axes are on the same scale for the simulation and the experiment. The arrows and circles in the simulated RSMs are discussed in the text.

for the device layer peak. The strain in the AlN was 300 MPa in the experiment and in the simulation the strain was -300 MPa in the SiO_n layers and -750 MPa in the AlN layer. Similar to the experimental RSM's, the simulated diffraction pattern also exhibited the deformation of the diffraction peak related to the different strain distribution near the buried oxide and the surface of the SOI wafer. In addition, using these parameters a good agreement between the strain gradient (Substrate-SOI_{top}) was obtained for the packaged and the open device. The strain gradients and the difference between open and packaged state were equivalent between the experiment and the simulation.

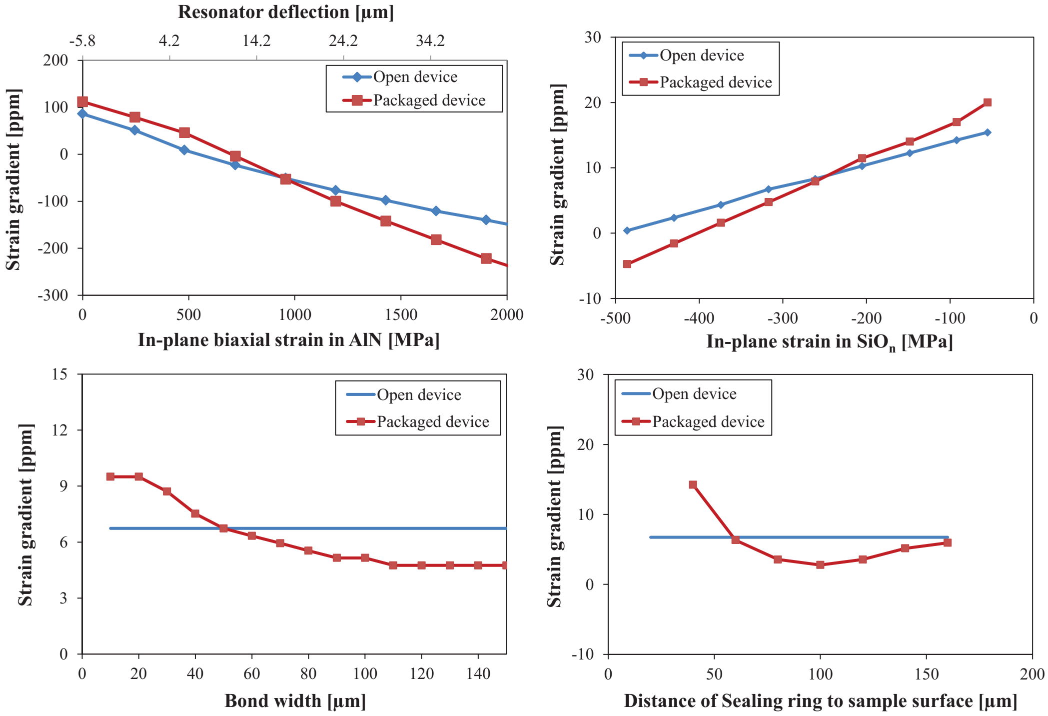

Figure 3.15: Finite element model of the MEMS package. The graphs show a section through the device whose sidewall is at x=0. The color indicates the level of the *x*-component of the stress in the silicon after convergence of the simulation. The left graph shows an open device while the right graph shows a device with a cap, which changes the strain distribution in the device layer.

Figure 3.15 shows the strain gradient (substrate – SOI_{top}) in dependence of four different parameters: Residual bi-axial stress in the AlN layer, residual stress in the SiO_n layers, distance between the surface and the sealing ring and width of the sealing ring (i.e. width of the bond). Clearly the residual strain in the AlN layer has the strongest influence on the diffraction pattern. In the range of stresses relevant for this study, the strain gradient in the packaged devices was more tensile than in the open devices, and the slope of the strain gradient versus residual stress was also higher in the packaged devices. Therefore the same trend was obtained in the simulation and the experiment. However, the slopes were a factor of 2.5-3 smaller than in the experiment. While a part of the difference may be caused by other parameters, the large difference must also be due to limitations of the model. There are several shortcomings of the simulations, which are discussed in the following:

1) In the simulations an additional peak was obtained (indicated by the red arrows and circles in the right graphs of Figure 3.14). This peak originated from the strain relaxation in the silicon at the surface of the device layer. When the first few micrometers of material below the surface were excluded from the simulation, this peak vanished (Figure 3.16). There is evidence that this may be justified by the damage induced at

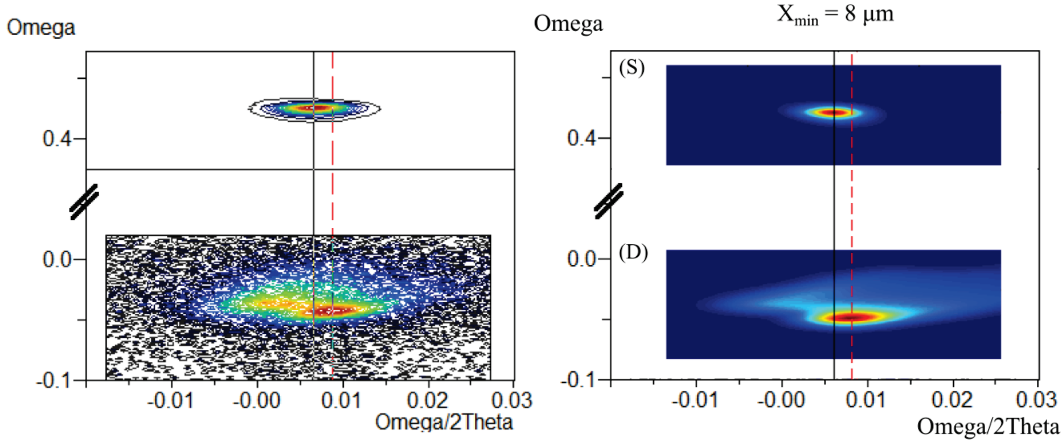

Figure 3.16: Comparison of the experimental (left) and simulated RSM's for an open device – the same device as shown in Figure 3.14. The right graph shows the simulation of the RSM after removal of the diffraction signal from the first 8 µm below the (sidewall) surface. *Omega* and *Omega/2Theta* axes show degrees on a relative scale.

the surface of the device by the sawing process. The diamond sawing process can be considered to be equivalent to polishing [150]. During the dicing process large compressive stresses are formed when the diamond grits scratch the silicon. Under these pressures a phase transformation into amorphous silicon and various other crystalline phases of silicon occurs and a damaged sub-surface layer is formed [151]-[153]. Depending on the size and size distribution of the diamond grits, the speed of the tool and the normal load, ductile or brittle abrasion dominates. For instance, in ref. [151] the sub-surface damage caused by rough grinding (320 mesh grid) and ultrafine grinding (diamond grit with few micrometers diameter) has been investigated. Ductile abrasion has been found to dominate in ultrafine grinding and caused a quite uniform layer structure consisting of amorphous silicon (few nanometers) on top of plastically deformed silicon (~2 µm) and strained silicon (~2 µm). The brittle abrasion which dominated in rough grinding led to much deeper-reaching damage where the plastic deformation reached about 3.5 µm and the strained silicon layer and sub-surface cracks extended approximately 20 µm below the surface. A method to verify if sawing damages are the reason for the absence of the additional peak would be to use another dicing method such as stealth laser dicing which is known to induce less damage at the cut surface [154],[155].

2) As mentioned above, the difference between the strain gradients (substrate–SOI_{top}) was similar in the experiment and the simulation, and the general trend of the strain gradient versus residual stress in AlN was reproduced in the simulation. (Upper left graph in Figure 3.15). However, the biaxial strain in AlN which was required to obtain the respective strain gradient was much larger than the experimentally measured

strain. In addition, the slope of the deflection (or residual stress) versus strain gradient curve differed significantly between the experiment and the simulation. This was presumably due to the two-dimensional nature of the model which was not capable of reproducing the biaxial strain distribution of the system.

3) A third point is the intensity distribution of the simulated reciprocal space maps. As discussed, photoelectric absorption has been implemented in the model. However, in quasi-perfect crystals such as single crystal silicon additional attenuation due to dynamical scattering effects occurs. This is due to multiple scattering, refraction and extinction (attenuation due to loss of intensity of the incident beam into the diffracted beam) [156]. Extinction only affects a very narrow angular range around the Bragg peaks (on the order of 0.01°) [157]. As the diffraction peaks of the substrate (handle wafer) and the device layer are heavily offset in reciprocal space extinction is only expected within the individual silicon layers. For intensity matching and advanced analyses such as defect density investigations dynamical diffraction theory would have to be implemented.

3.4 Conclusions and chapter summary

In this chapter the piezoelectrically activated silicon resonators were introduced, their fabrication and electrical characterization outlined and structural analyses which have been performed were discussed. The obtained results show that it is possible to access detailed information about the strain distribution in MEMS devices and packages by x-ray diffraction techniques. This includes the analysis and quantification of residual stresses in the silicon and the functional layers, the analysis of the texture of the materials and the determination of the packaging-induced stresses in buried structures. It was shown that although the sealing ring was located at a large depth below the specimen surface, it is possible to obtain valuable information on the strain distribution and strain level in the device. The strain distribution was found to be dominated by the residual stresses in the SiO_n and the AlN layers. Only small changes were observed after packaging, showing that the applied packaging method, the Au-Sn eutectic bonding, is a suitable packaging method and influences the devices only in a minor manner.

Finite element simulations support the analysis and allow comparing theoretical models of the system with the experimental results. The stress levels and the influence of bonding were also qualitatively reproduced by the simulations. In addition, finite element simulations allow evaluating the influence of individual parameters on the strain distribution in the devices.

As discussed in sections 2.3 and 2.7.1.1, stresses and stress relaxation are an important contributing mechanism for aging in microresonators. By making such effects accessible, the discussed method supports the interpretation and analysis of diffraction patterns related to complex deformations.

Chapter 4
Air Damping in Tuning Fork Resonators

This chapter focuses on the air damping of the piezoelectrically activated silicon tuning fork resonators. As noted in section 3.2, these devices had been designed for sensing the leak rate in very small cavities. The resonance frequency and the quality factor of the resonators are influenced by the material properties, the strain distribution and the air pressure. The former factors have been discussed in the previous chapters and to complete the discussion this chapter is dedicated to the investigation of the influence of air damping on the resonance characteristics, as well as the functional characterization of the device in the view of its purpose, pressure sensing.

The applicability of tuning forks for pressure sensing [158], [159], gas density measurement [160] and force sensing [161] has been investigated previously in quartz tuning fork resonators, which were relatively large (~3 mm length). Resonators based on SOI-wafers enable miniaturization, high die density on the wafer and wafer-level encapsulation with nanoliter-package volumes. However, similar to residual stresses which can radiate and affect neighboring structures, the small size and close proximity of structures leads to mutual influences mediated by the surrounding gas. The proximity of the two tines and the frame around the resonators, which provides mechanical stability and carries the sealing rings for the wafer level-encapsulation, gives rise to additional damping by air being squeezed in the small gaps. As noted in section 2.9 monitoring the resonance frequency and quality factor variations over time can be used to determine the hermeticity and leak rates in very small packages where the traditional helium leak test method fails because the relevant leak rates are below its sensitivity [115]. This is of crucial importance in high-reliability applications such as space exploration and medical technology where hermeticity must be ensured over decades [113]. Understanding the pressure sensitivity allows efficient design of the pressure-sensing resonators and also enables the determination of admissible pressure levels in resonator packages (other than pressure sensors) above which the performance is deteriorated by air-damping.

The following section contains an overview over the pressure regimes which characterize the air damping, namely the structural-damping regime where air damping is negligible, the free molecular regime and the viscous regime. The damping models for the framed tuning fork geometries are developed based on previous works reported in literature. Thereafter the experimental results are presented, compared to the models and discussed.

4.1 Air damping in microresonators

4.1.1 Equation of motion for a damped Euler-Bernoulli beam

If squeeze-damping is negligible, the tuning fork resonators can be considered to be equivalent to single fixed-free cantilevers [158]. The energy dissipation in resonators is mediated by various processes, which either depend on the internal structure and geometry of the system or on the surrounding environment. The quality factor of the resonator is related to the energy dissipated in one cycle *ΔE* divided by the total energy of the resonator E_0. The total energy dissipated is the sum of the contributions of all damping factors ΔE_i

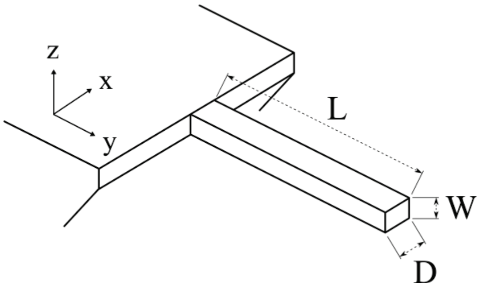

Figure 4.1: Schematic representation of the cantilever dimensions. The beam performs an oscillation along the *x*-axis.

$$Q = \frac{2\pi E_0}{\Delta E} = \frac{2\pi E_0}{\sum_i \Delta E_i}. \tag{4.1}$$

The contributions of all damping processes can therefore be calculated separately and then be combined to yield the overall quality factor. The force per unit length F_d acting on a cantilever beam moving in the *x*-direction consists of a dissipative component f_1 related to the velocity, and an inertial component f_2 which is related to the acceleration of the beam [162]

$$F_d = f_1\dot{x} + f_2\ddot{x}. \tag{4.2}$$

The effect of damping on the motion of a cantilever according to the Euler-Bernoulli beam theory can be evaluated by solving the equation of motion for a driven resonator [163]:

$$(\rho_b DW + f_2)\frac{\partial^2 x(\xi,t)}{\partial t^2} + f_1\frac{\partial x(\xi,t)}{\partial t} + EI\frac{\partial^4 x(\xi,t)}{\partial \xi^4} = F\cos(\omega_F t). \tag{4.3}$$

The deflection *x* in the *xy*-plane is dependent on the time *t* and the position ξ along the beam (Figure 4.1). For small amplitudes the *y*-deflection can be neglected. The variable ξ is the position along the beam, and runs from the base $(\xi = 0)$ to the tip of the beam $(\xi = L)$. The beam cross-section is *DW*, ρ_b is the mean density of the cantilever, ω_F is the driving frequency, *E* is the Young's modulus and *I* is the second moment of inertia. A separation of variables yields $x(\xi,t)=X_n(\xi)X_1(t)=X_n(\xi)\cos(\omega t+\varphi)$, where $X_n(\xi)$ is the shape function of the harmonic modes. Based on the above equations the following identities for the resonance frequency and the quality-factor can be obtained:

$$\omega_0=\sqrt{\frac{EI}{(\rho_b DW+f_2)}\frac{\alpha_n^4}{L^4}-\frac{1}{2}\frac{f_1}{(\rho_b DW^2+f_2)^2}}\approx\frac{\alpha_n^2}{L^2}D\sqrt{\frac{E}{12\rho_b}}\left(1-\frac{1}{2}\frac{f_2}{\rho_b DW}\right), \tag{4.4}$$

$$Q=\frac{(\rho_b DW^2+f_2)\omega_0}{f_1}=\frac{\rho_b DW^2\omega_0}{f_1}. \tag{4.5}$$

The factor α_n equals to 1.8751 for the first resonance mode. If f_2 is small, the frequency ω_0 may be approximated by the undamped resonance frequency

$$\omega_0\cong\frac{\alpha_n^2}{L^2}D\sqrt{\frac{E}{12\rho_b}}. \tag{4.6}$$

The left and right expressions in (4.4) and (4.5) are the exact solutions and the weak-damping approximations ($f_2 \ll \rho_b DW$), respectively. Similar expressions have been used by various researchers to analyze the motional behavior and damping of microresonators [160], [164], [165]. The resonance frequency and quality factors can be calculated directly from (4.4) and (4.5) if the damping parameters f_1 and f_2 are known. However, in most cases one has to recur to (4.1) and sum up the individual contributions of all relevant damping effects, which will be discussed in the following.

4.1.2 Air damping regimes

Three major regimes of pressure dependency can be discriminated [158], as shown in Figure 4.2. In the intrinsic damping regime the pressure of the surrounding air is sufficiently low so that the damping by air is negligible compared to other friction processes. Only if the air density is increased, the momentum transfer between air molecules and the oscillating structure becomes significant and leads to detectable changes in the damping characteristics. At low pressures the interactions between the air molecules can be neglected, and the physical properties of the air are described by statistical mechanics. Consequently this pressure range is termed the free molecular damping regime. At higher gas densities where the assumption of non-interacting particles breaks down, the air is considered as a continuum and fluid dynamics describes the motion of air and it's damping effect on the resonators. This is called the viscous damping regime.

This categorization is rather coarse but captures many of the essential features of air damping. The range in which one of the damping mechanisms is dominant depends not only on the absolute pressure (and hence the gas mean free path) but also on the dimensions of the system. The ratio of the two length scales is called Knudsen number K_n. It relates the mean

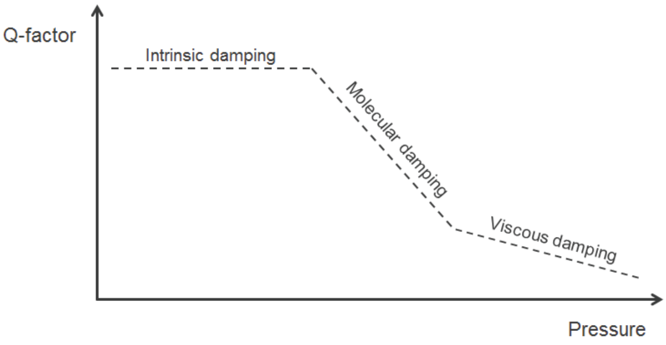

Figure 4.2: Quality factor versus air pressure scheme showing the three damping regimes of intrinsic damping, molecular damping and viscous damping. Adopted from [158].

free path of gas molecules λ with the characteristic size of the system d which here is the width of the gap separating the tuning fork tines and separating the tines from the frame. The Knudsen number is defined as [166]

$$K_n = \frac{\lambda}{d} = \frac{k_B T}{\sqrt{2} d \pi d_m^2 p} . \tag{4.7}$$

where d_m is the molecule diameter (3.7 x 10^{-10} m for air [167]), k_B is the Boltzmann constant, T is the temperature and p is the pressure. Based on the Knudsen number the pressure regimes are generally classified as follows: If the mean free path of the gas is small ($K_n < 0.01$) the air is considered as a continuum and viscous damping prevails. Between 0.01 and 10 the transition occurs into the molecular regime which itself covers all pressures where the Knudsen number is above 10 [166].

4.1.3 Intrinsic damping

The intrinsic friction processes contribute to damping at all pressures but dominate only at low pressures. Depending on the system various friction processes may be relevant [168], [6]:

- Thermo-elastic damping: The cyclic compression and expansion of the material during the oscillation leads to temperature gradients in the resonator. The resulting heat flows cause energy losses. For tuning forks with designs similar to the ones used in the present work, this loss mechanism was reported to be dominant for devices in the resonance frequency range between 30 kHz to 80 kHz [132].
- Clamping losses: Dissipation of vibrational energy into the supporting structure. This damping mechanism is effectively reduced in the tuning forks due to the anti-phase motion of the two tines [158].

- Internal friction and/or enhanced dissipation in a surface layer (functional layer or native oxide) [169]. In AlN-activated resonators the main contribution to intrinsic damping has been attributed to losses in the metallic electrodes [170], [171].

Considering the various possible damping mechanisms and the fact that these processes heavily depend on the material properties and the fabrication processes, it is usually not possible to predict the intrinsic damping. It must be determined, analyzed and optimized for each system individually.

4.1.4 Molecular damping

Air molecules scattered on the resonator surfaces will undergo a momentum transfer which leads to damping of the oscillation. At small amplitudes the resonant structure can be considered to move along a single axis and the net effect of the scattering on the walls parallel to the direction of the oscillation will be zero. The movement of the resonator leads to a pressure difference between the front side and the backside of the resonator which to the author's knowledge was first derived in [172]. At low pressures the probability of a particles to be at a velocity *v* in a given direction, here the *x*-axis, is given by the Maxwell-Distribution

$$f(v_x) = \sqrt{\frac{m}{2\pi k_B T}} e^{-\left(\frac{m v_x^2}{2 k_B T}\right)} dv_x \qquad (4.8)$$
,

where *m* is the mass of a gas molecule. The momentum transfer of a molecule hitting a static surface is $mv_x^2 - (-mv_x^2) = 2mv_x^2$. In the case of a resonating cantilever the speed of the molecules colliding with the cantilever surface which is moving at a velocity $\dot{x}$ is $v_x - \dot{x}$ and $v_x + \dot{x}$ for the front- and backside respectively. The pressure is defined as the momentum transfer per unit area and therefore differs between the front side and the backside. This pressure difference obviously depends on the number of collisions (and hence the pressure) and the speed of the moving surface. It is given by

$$\Delta p = 4\sqrt{\frac{2}{\pi}} p\dot{x} \sqrt{\frac{RT}{M}}, \qquad (4.9)$$

where the conversion into molar units has been made, so *R* is the gas constant and *M* the molar molecular weight (for air *M* = 0.029 kg/mol). The force resulting from this pressure difference has been used to calculate the molecular damping of vanes and oscillating fibers [172], [173]. This approach of calculating the quality factor is commonly referred to as Christian's model:

$$Q_{Christian} = \left(\frac{\pi}{2}\right)^{\frac{3}{2}} \rho_b D f_0 \sqrt{\frac{RT}{M}} \frac{1}{p}. \tag{4.10}$$

Here D is the thickness of the resonator and f_0 the un-damped resonance frequency. It can be seen from (4.10) that the quality factor is proportional to the thickness of the resonator. A thin cantilever possesses a lower mass and inertia and is therefore sensitive to air-damping at lower pressures than thicker resonators. If the total mass and the density of the resonator are held constant, a higher thickness results in smaller surface areas in the direction of motion and thus also less air damping. This theory has been successfully used to model the molecular damping in microresonators by several authors [158], [174], [175].

4.1.5 Squeeze-film damping in the molecular damping regime

While the results of Christian's model are generally in very good agreement with the experimental results for free-standing thin resonators, the influence of the surrounding structures must be accounted for if the mean free path of the gas is similar to their separation distances. In this case, the velocity distribution of the gas molecules is no longer in equilibrium but is influenced by the resonator itself, which gives rise to squeeze-film damping. There are two main approaches for the analysis of squeeze film damping: The continuum fluid based approach based on Reynolds equation and the molecular damping based on the energy and energy transfer of individual gas particles. The continuum fluid approach is justified in the pressure range where the mean free path is much smaller than the characteristic length scale of the system and continued efforts have been made to extend the model also to lower pressures in the molecular regime (e.g. [123], [176], [177]). However if the mean free path is much longer than the system it is more physically meaningful to consider individual gas particles. Bao et al. [178] have developed a model of squeeze-film damping in resonant structures in the free molecular regime based on the collision of gas particles with the solid walls of the system. They considered a plate parallel to a wall, oscillating in the direction normal to the plane of the wall (Figure 4.3). As the particle travels through the gap it repeatedly collides with the wall and the resonator. Under the assumption of elastic collisions, the particle will be accelerated (or decelerated) due to the motion of the plate. The total energy taken up (or given off) by the air molecules in the gap in one oscillation cycle is related to the total internal energy of the resonator to calculate the Q-factor.

The model for the analysis of the air damping in the molecular damping regime used in this work is based on Bao's model and therefore this model is outlined in the following. The coordinate system is chosen such that the plate is resonating in the xy-plane (Figure 4.3). Per unit time the number of particles moving into the gap with the area Ld is [178]

$$\frac{1}{4} n_0 \bar{v} L (d - x), \tag{4.11}$$

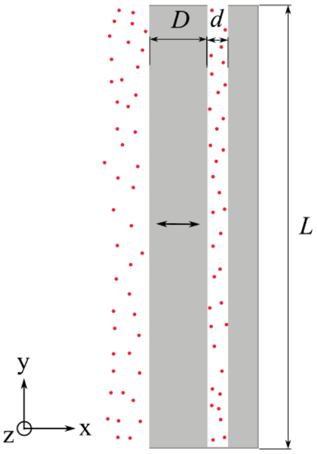

Figure 4.3: Schematic representation of a plate oscillating near a static wall. The plate is oscillating in the plane of the page. The red dots represent the air particles. The distance between the beam and the wall is *d*, the plate length is *L*, the thickness is *D* and the width out of the image plane is *W*.

where n_0 is the air molecule number density and $\bar{v} = \sqrt{8RT / M\pi}$ is the average speed of the molecules. If it is assumed that the deflection x is much smaller than the gap spacing, the gap size d can be assumed to be constant. Equation (4.11) is the well-known relationship for the number of collisions occurring per unit time on the wall of a box containing a diluted gas [167]. The energy of a gas particle entering the gap is $v_{x,0}$ in the x-direction and v_{yz} parallel to the plate. During the passage through the gap the absolute value of the velocity of the gas molecule in the x-direction changes by $2\dot{x}$ each time it collides with the beam. The geometrical parameter l_t describes the average distance a particle passes in the gap in the yz-plane and is equal to $\sqrt{2LW / \pi}$ [178]. Therefore the number of collisions is the total dwell time in the gap $\left(t_d = l_t / \bar{v}_{yz}\right)$ divided by the time between two collisions with the moving resonator $\left(2d / \bar{v}_{x,0}\right)$. Hence, after passing through the gap the average energy is the sum of its initial energy $v_{x,0}$ and the energy change it accumulated in N collisions

$$\bar{v}_x = \bar{v}_{x,0} + N2\dot{x} = \bar{v}_{x,0} + \frac{l_t}{\bar{v}_{yz}} \frac{\bar{v}_{x,0}}{2d} 2\dot{x} \,. \tag{4.12}$$

In terms of energy, the kinetic part E_{kin} of the molecule entering into the gap is

$$E_{kin,0} = \frac{1}{2} m\left[\bar{v}_{x.0}^2 + \bar{v}_{yz}^2\right] \,. \tag{4.13}$$

and after passing through the gap E_{kin} has become

$$E_{kin,end} = \frac{1}{2} m \left[\bar{v}_{yz}^2 + \left(\bar{v}_{x.0} + \frac{l_t}{\bar{v}_{yz}} \frac{\bar{v}_{x,0}}{d} \dot{x} \right)^2 \right] = \frac{1}{2} m \left[\bar{v}_{yz}^2 + \bar{v}_{x,0}^2 + 2 \frac{l_t}{\bar{v}_{yz}} \frac{\bar{v}_{x,0}^2}{d} \dot{x} + \frac{l_t^2}{\bar{v}_{yz}^2} \frac{\bar{v}_{x,0}^2}{d^2} \dot{x}^2 \right] \cdot \tag{4.14}$$

This energy change is multiplied by the number of particles entering the gap per unit time (4.11) and integrated over one oscillation cycle

$$\Delta E_{cycle} = \frac{1}{8} m n_0 \bar{v} L d \int_0^{2\pi/\omega} \left(\left[2 \frac{l_t}{\bar{v}_{yz}} \frac{\bar{v}_{x,0}^2}{d_1} \dot{x} + \frac{l_t^2}{\bar{v}_{yz}^2} \frac{\bar{v}_{x,0}^2}{d_1^2} \dot{x}^2 \right] \right) dt \, . \tag{4.15}$$

The velocities are related by $\sqrt{2}\bar{v}_{x.0} = \bar{v}_{yz}$ and the density of the air is $\rho_{air} = n_0 m = pM / RT$. The $\dot{x}$-term in (4.14) and (4.15) cancels out over one cycle of the resonator. For $\dot{x} = A\omega \sin(\omega t)$ this results in

$$\Delta E_{cycle} = \frac{\pi}{16} \rho_{air} \bar{v} L \frac{l_t^2 A^2 \omega}{d} \, . \tag{4.16}$$

As noted on page 78 the Q-factor of the resonator is given by the ratio of the internal energy to the energy dissipated during one cycle according to (4.1). The internal energy E_0 is the sum of the kinetic and the potential energy of the resonator

$$E_0 = E_p + E_k = \frac{1}{2} EIx^2 + \frac{1}{2} \rho_b WDL\dot{x}^2 \, . \tag{4.17}$$

The potential energy is zero when the kinetic energy is maximum (at the moment when the resonator passes the equilibrium position (x=0), and where $E_0 = E_k = \frac{1}{2} \rho_b WTLA^2 \omega^2 \sin^2(\pi / 2)$. This leads to

$$Q_{Bao} = \frac{2\pi E_0}{\Delta E_{cycle}} = 16\pi \frac{d}{L} \left(\frac{\pi}{2} \right)^{\frac{3}{2}} \rho_b D f_0 \sqrt{\frac{RT}{M}} \frac{1}{p} \, . \tag{4.18}$$

This is the Q-factor of a plate oscillating near a wall (Figure 4.3) in the molecular damping regime as given by Bao's model [178]. The Q-factor in Bao's model therefore is decreased by a factor of *16πd/L* in comparison to Christian's model.

4.1.6 Refinement of Bao's model

Hutcherson and Ye [179] have presented molecular dynamics simulations (MD) of squeeze-film air damping in microstructures. In their simulations some of the rigid assumptions made by Bao and co-workers have been relaxed [179]:

- Constant particle velocity: The number of collisions was calculated based on the initial particle velocity. However, this overestimates the number of collisions when the particle velocity v_x is slowed down by the plate because it will take the gas particle longer to bounce back and forth between the wall and the plate, while v_{yz}, which defines the dwell time in the gap, remains unchanged. Similarly the number of collisions is underestimated when the gas particle is accelerated by the resonator.

- Constant gap size: The amplitude of the oscillation is neglected. Non-negligible amplitudes will influence the number of particles entering the gap and vary the number of collisions a gas particle undergoes.
- Constant plate velocity: The speed of the plate is considered to be constant throughout the time the gas particle travels through the gap. This is only valid if the dwell time in the gap is much shorter than the oscillation period.

The MD simulations resulted in a quality factor which was reduced by a factor of about two and agreed better with the case considered (experimental data from Zook et al. [180]). The more recent MD simulations reported in ref. [181] point into the same direction. While providing better insight into the molecular damping mechanisms, such simulations require specialized software and implementation efforts. As will be shown in the following, the above assumptions can also be accounted for analytically.

The starting point is again a gas particle entering the gap with the initial velocities v_x and v_{yz}. However, now the gap size d and $\dot{x}$ are a function of time, so the change of velocity in the x-direction is given by

$$\frac{dv_x}{dt} = t\frac{v_x}{\left(d - A\cos(\omega t + \phi)\right)} A\omega \sin\left(\omega t + \phi\right), \tag{4.19}$$

where ϕ is the phase of the resonator and A is the amplitude. The boundary condition is that the velocity v_x is equal to $v_{x,0}$ at the time when the particle enters the gap, i.e. $v_x(t=0) = v_{x,0}$. The solution for this differential equation takes the form

$$v_x(t) = \frac{v_{x,0}\left(d + A\cos(\phi)\right)}{\left(d + A\cos(\omega t + \phi)\right)}. \tag{4.20}$$

After its passage through the gap the average velocity of a gas particle therefore reads

$$\bar{v}_x(t_d) = \frac{\bar{v}_{x,0}\left(d + A\cos(\phi)\right)}{\left(d + A\cos(\omega \frac{l_t}{\bar{v}_{yz}} + \phi)\right)}. \tag{4.21}$$

As done above, the change in kinetic energy is multiplied by the number of gas particles entering the gap and integrated over a full oscillation cycle:

$$\Delta E_{cycle} = \frac{1}{8}\rho_{air}\bar{v}L\int_0^{2\pi}\left[-v_{x,0}^2\left(d - A\cos(\phi)\right) + \left(\frac{\bar{v}_{x,0}\left(d + A\cos(\phi)\right)^2}{\left(d + A\cos(\omega\frac{l_t}{\bar{v}_{yz}} + \phi)\right)}\right)^2\right]d\phi \,. \tag{4.22}$$

This integral can be solved analytically and results in

$$\Delta E_{cycle} = \frac{1}{4}\rho_{air}\bar{v}L\frac{\bar{v}_{x.0}^2}{\omega}\pi\begin{pmatrix} -2d\left(4\cos^3(\omega t_d) - 3\cos^2(\omega t_d) - 3\cos(\omega t_d) + 2\right)\left(1 - \frac{d}{\sqrt{d^2 - A^2}}\right) + \ldots \\ \ldots A^2\frac{\left(3A^2\cos^3(\omega t_d) - 4d^2\cos^3(\omega t_d) + 3d^2\cos^2(\omega t_d) - 3A^2\cos(\omega t_d) + d^2\right)}{\left(d^2 - A^2\right)^{3/2}}\end{pmatrix}. \tag{4.23}$$

If the dwell time is much smaller than the oscillation period this formula may be approximated by using $\cos(\omega t_d) \approx 1 - \frac{1}{2}\left(\omega t_d\right)^2$ and conducting a Taylor expansion to the second order at $\omega t_d = 0$. This leads to

$$\Delta E_{cycle} = \frac{3}{16}\rho_{air}\bar{v}L\omega l_t^2\pi\frac{A^2}{d} \,. \tag{4.24}$$

Finally the Q-factor is obtained (the subscript *m-Bao* stands for 'modified Bao's model'):

$$Q_{m-Bao} = \frac{2\pi E}{\Delta E_{kin}} = \frac{8}{3}\frac{d}{L}\pi\rho_b\frac{T\omega}{\bar{v}\rho_{air}} = \frac{16}{3}\pi\frac{d}{L}\left(\frac{\pi}{2}\right)^{\frac{3}{2}}\rho_b D f_0\sqrt{\frac{RT}{M}}\frac{1}{p} \,. \tag{4.25}$$

From the previous considerations the following conclusions can be drawn. The quality factor obtained by the Christian's model, Bao's model and modified Bao's model (this work) are related to each other by

$$Q_{Christian} = 16\pi\frac{d}{L}Q_{Bao} \approx \frac{16}{3}\pi\frac{d}{L}Q_{m-Bao} \,. \tag{4.26}$$

If the gap size ratio *d/L* is larger than *3/16π* then $Q_{Christian}$ will dominate over the squeeze-film air damping. For the quartz tuning fork geometries whose pressure sensitivity was reported in literature the *d/L* ratios were significantly larger than this threshold (about $(4\pi)^{-1}$) [182], [183] (in [182] the groove width was not explicitly specified, and was therefore estimated from the image of the tuning fork). For the silicon tuning forks investigated here the *d/L*-ratio was about 4 times smaller than the limiting value, positioning the system far inside the squeeze-film air damping regime.

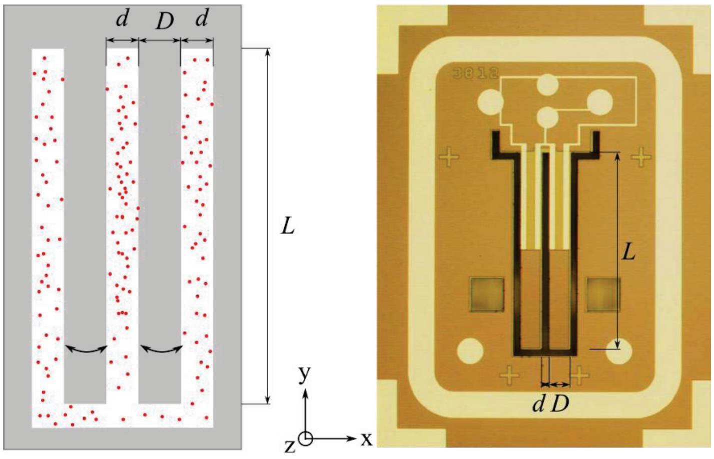

Figure 4.4: Top view of oscillating beam resonators. The tines of the resonator are oscillating in the plane of the page. (Left) Schematic representation of a tuning fork resonator with two times and a surrounding frame. (Right) Top view of a piezoelectrically activated silicon resonator. The distance between the two tines is 30 µm and is equal to the distance to the frame. The length *L* is 900 µm, the thickness *D* is 100 µm and the width *W* (out of the image plane) is 20 µm.

The above models can also be easily applied to a framed tuning fork geometry as it is the case in the piezoelectrically activated resonators considered here[12]. Figure 4.4 shows an optical micrograph of the silicon tuning fork and the schematic representation used for the analysis. The Q-factor of this geometry is

$$Q_{m-Bao} = \frac{32}{15}\pi\frac{d}{L}\left(\frac{\pi}{2}\right)^{\frac{3}{2}}\rho_b D f_0 \sqrt{\frac{RT}{M}}\frac{1}{p}, \tag{4.27}$$

which is a factor of 2/5 smaller than the case of a beam oscillating near a static wall due to the additional damping between the two oscillating tines. In the results section the new model will be compared to the experimental result of Zook et al. [180] as well as the quality factors of the silicon tuning fork resonators in the molecular damping regime.

---

[12] A note on beam mode shape may be appropriate at this point: As described above, Bao et al [178] have considered a plate oscillating near a wall at a constant amplitude. It has been claimed (e.g. in ref. [122]) that this molecular damping model is not applicable to cantilever beams due to the variation of the amplitude along the beam. However, the influence of the amplitude on the quality factor is very small above a gap-to-amplitude higher than ~5 (a variation of 4% of the quality factor over a gap-to-amplitude range from 5 to 100 was estimated based on the graphs shown in [179]), and hence also a small variation of the amplitude is expected to have a neglgible influence on the damping.

The above considerations presuppose the absence of interactions between the air molecules. However, when the pressure is raised the mean free path of the gas molecules decreases and this assumption breaks down. During its passage through the gap, which on average lasts $\Delta t = l_t / \bar{v}_{yz}$, the gas particle covers on average a distance of

$$\frac{l_t}{\bar{v}_{yz}} \bar{v} = \sqrt{\frac{3}{2}} l_t \quad . \tag{4.28}$$

It is reasonable to assume that the cross-over into the transition regime starts when the mean free path falls below this distance. At $K_n = 4.4$ or $p = 0.5$ mbar this condition is fulfilled for the tuning fork resonators studies in this work.

4.1.7 Viscous damping

The viscous damping regime is governed by continuum motion of fluids, described by the Navier-Stokes equation. For small separations between surfaces in relative motion the Navier-Stokes equation can be approximated by the Reynolds equation. For a review of viscous squeeze film damping it is referred to [123]. A condition for the applicability of the Reynolds equation is that the Reynolds number ($R_s = \omega \rho_a d / \mu$) related to squeeze motion is much smaller than unity (μ is the viscosity of air). In the viscous damping regime ($K_n < 0.01$) the R_s number of the silicon tuning forks investigated here is constantly larger than ten. Therefore squeeze-film effects are not relevant in the viscous damping regime.

The Navier-Stokes equations can only be analytically solved for simple shapes like a harmonically oscillating sphere [162]. The 'string of beads' model, in which the dissipative drag on a cantilever is related to a string of oscillating spheres, has been first introduced in ref. [182], to relate the air pressure to the impedance of a quartz tuning fork. The model was refined thereafter by the same group [184], [185] then extended to the quality factor of single-beam resonators [164], [165], and applied to various systems by other researchers [186], [187]. In the original work by Kokubun and co-workers [182] the cross-sectional aspect ratio of the tines was close to unity (W/D = 0.6 mm / 0.5 mm). A close agreement between the model and the experimental data was found with the diameter of the sphere being equal to the width of the tines. For cantilever beams Hosaka et al. [165] have given a formulation for the quality factor based on spheres with the diameter b equal to the width of the beam W, independently of the thickness of the beam. The Q-factor of the resonator beam in this model is given by

$$Q = \frac{\rho_b D W^2 \omega}{f_1 W} = \frac{\rho_b D W^2 \omega}{3\pi\mu b + (3/4)\pi b^2 \sqrt{2\mu(M/RT)\omega p}} , \tag{4.29}$$

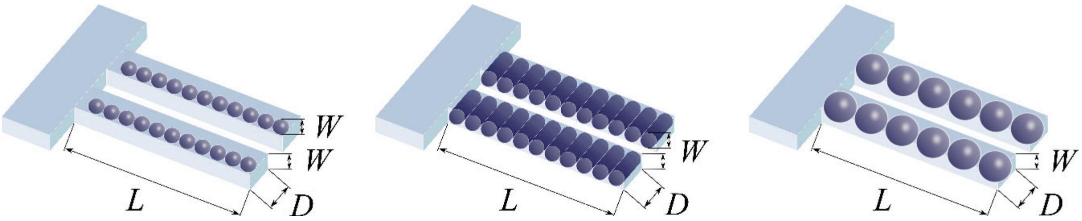

Figure 4.5 Representation of the resonators by a 'string of bodies'. (Left) Spheres with diameter equal to the width *W* of the beams [165]; (Center) Cylinders with length *D* and diameter *W*; and (Right) Spheres with the same volume as the cylinders in the center figure.

which was obtained by neglecting the inertial part of the drag. The denominator in (4.29) is the dissipative component of drag of an oscillating sphere [162]. Note that it is composed of a frequency-independent part (called Stokes-drag) and a frequency-dependent part.

Setting the sphere diameter equal to the beam width offers a clear definition of the radius of the spheres which is directly related to the geometry of the cantilever. However, in the case of thick resonators as used here ($D/W = 5$) this theory is not directly applicable because the drag along the side-walls parallel to the direction of oscillation is not well-described. The resonator is more appropriately represented by a string of cylinders than a string of spheres (Figure 4.5). It is not possible to analytically calculate the drag on short cylinders in motion parallel to their axis, but numerical studies may provide insight. The creeping flow (or Stokes flow) of a viscous fluid past solid particles of arbitrary shapes has been studied previously [188], [189]. The Stokes drag on a sphere is $F_S = 6\pi\mu R$ and is equal to the frequency-independent part of f_1. It was found that the drag on a cylinder moving parallel to its axis is related to the drag on a sphere with the same volume by a drag factor *K*. The factor *K* for various length-to-thickness ratios from the data given in [188] is shown in Figure 4.6. The radius of the sphere is $r_s = \sqrt[3]{3/16\, DW^2}$. This correlation can be used to determine the radius r_s of a sphere that's damping is equivalent to the rectangular beam. Using this relationship leads to

$$Q = \frac{\rho_b D W^2 \omega}{\frac{1}{K}\left(6\pi\mu r_s + 3\pi r_s^2 \sqrt{2\mu (M/RT)\omega p}\right)}. \tag{4.30}$$

It is repeated here that for the determination of the *K*-factor in refs. [188], [189] only the Stokes drag was considered, and it is not certain that the same factor is valid for the frequency-dependent part of drag. Therefore this approach is expected to be more robust at low frequencies and pressures, where the first summand is dominating. The frequency-dependent part increases with the pressure and is larger than the frequency-independent part above a pressure of 200 mbar for the resonators considered here. However, for the cross-sectional

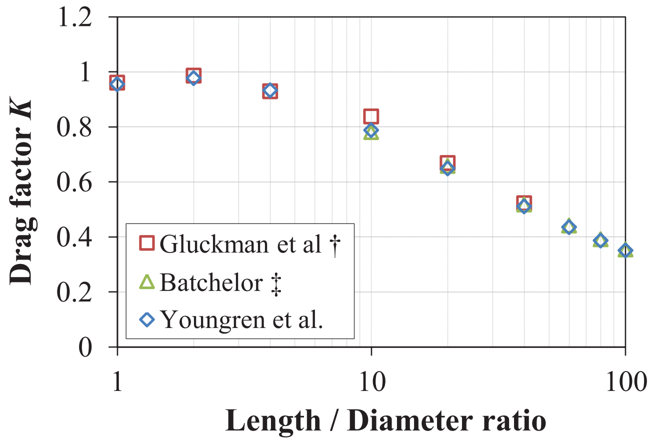

Figure 4.6: The drag factor *K* which denotes the ratio between Stokes drag force on a sphere and a cylinder with the same volume. The cylinder is translating parallel to its axis. The figure is a representation of the tabular data given in [188], including data from [190](‡) and [191](†). Where simulations with varying mesh sizes were made, the results shown here are the ones obtained with the maximum number of elements.

aspect ratios relevant here (which was 5) the *K*-factor is close to unity and does not very significantly influence the results. The equivalent sphere radius and the drag factor for the tuning fork resonators were 20.2 µm and 0.88, respectively.

Resonance frequency

While the effect of air-damping on the resonance frequency is negligible in the molecular regime it becomes significant in the viscous regime. The resonance frequency (4.4) is mostly influenced by the inertial drag parameter f_2 which characterizes the added mass due to the boundary air layer around the cantilevers. In the viscous regime Hosaka and coworkers [165] have also proposed a model for the resonance frequency. In analogy to the considerations made above on the quality factor the drag forces are calculated based on the inertial drag parameter of cylinder-equivalent spheres

$$f_2 = \frac{1}{KW}\left(\frac{2}{3}\pi\rho_a r_s^3 + 3\pi r_s^2\sqrt{\frac{2\rho_a\mu}{\omega}}\right). \tag{4.31}$$

4.2 Experimental results and discussion

An experimental result reported in literature which was often used for comparing damping models was published by Zook et al. [180]. They investigated resonant polysilicon microbeams which were separated by a small gap from a membrane on both sides. The microbeams had a length of 200 µm a width of 40 µm and the gap on both sides was 1.1 µm. The thickness of the microresonator was 1.8 µm [178]. Figure 4.7 shows a comparison of

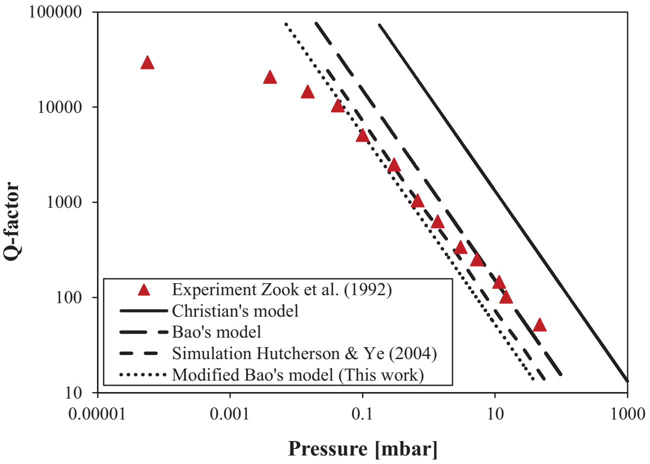

Figure 4.7: Comparison of the quality factor results between different models for molecular air damping in microbeams. The red triangles show the experimental results reported by Zook et al. [180]. The quality factors of the MD simulations by Hutcherson and Ye were extracted from figure 6a in ref. [179].

the experimental quality factors and the quality factors from Christian's model, Bao's model, the molecular dynamics simulations by Hutcherson and Ye [179] and the modified Bao's model presented above. At low pressures the quality factor approached a constant Q-factor of about 25000 which was determined by intrinsic damping. At higher pressures the damping was influenced by air damping. Figure 4.7 shows that the proposed analytical model for free molecular damping, which accounted for some of the simplifications made by Bao et al. [178] is in good agreement with MD simulations [179] and the experimental results obtained by Zook et al. [180].

With these encouraging results in mind the analysis of the framed piezoelectrically activated tuning fork resonators is discussed in the following. The frequency of the anti-resonance of the tuning fork resonators in vacuum was 152 kHz, which is about 10% lower than the theoretical value after (4.6). This discrepancy was comparable to reports in literature [192], [193] and was attributed to a combination of several factors. First, the density and dimensions of the tines were dominated by the silicon but the functional layers and fabrication tolerances influence the resonances. Further factors were the resonance splitting between the (lower-frequency) anti-resonance and the (higher-frequency) resonance, as well as the sturdiness of the resonators which caused the Euler-Bernoulli beam theory to overestimate the resonance frequency [194]. Although advanced elasticity theories like the Timoshenko beam theory would more accurately capture the resonance frequency of the system, the simple Euler-Bernoulli-theory can nevertheless provide valuable insight into the damping mechanisms, as shall be discussed below.

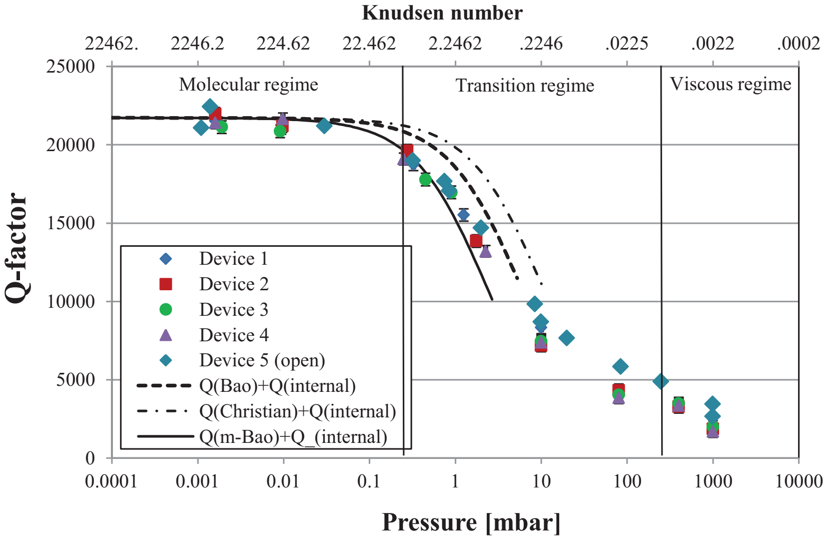

Figure 4.8: Experimental quality factors of four resonator devices versus the pressure. The dash-dotted line shows the Q-factor according to Christian's model. The dashed line is the model which includes squeeze-damping according to Bao's model [178]. The solid line shows the quality factor obtained in the modified Bao model (this work).

The quality factor of the resonators was measured in the range of 10^{-3} mbar to 1 bar on four encapsulated but non-hermetic resonators which originated from different regions on the same wafer, as well as one open resonator. Figure 4.8 shows the measured quality factors versus the pressure. The experimental errors were approximately equal to the size of the markers. The low variance in the quality factor values over the full investigated pressure range indicated that the fabrication was homogeneous over the wafer surface. The packaging also did not cause a significant change of the pressure sensitivity of the quality factor or the resonance frequency. In addition, no hysteresis effect was observed between decreasing and increasing pressure. The intrinsic damping limited the maximum quality factor to about 22'000. The graph also shows a comparison of Christian's model based on (4.10), Bao's model and the modified Bao's model of this work. In all cases the quality factors of the molecular damping were combined with the Q-factor under vacuum using (4.1) on page 78. The intrinsic damping dominated the quality factor almost up to the transition regime. Nevertheless, the pressure at which molecular damping started to significantly influence the resonators, and the pressure-dependency of the quality factor in the transition regimes were much closer correlated to the modified squeeze-film damping model than to Christian's model or Bao's model. These results indicate that the modified Bao's model is capable of capturing the onset of pressure sensitivity in microresonators subjected to squeeze film air damping in the case of a framed tuning fork geometry.

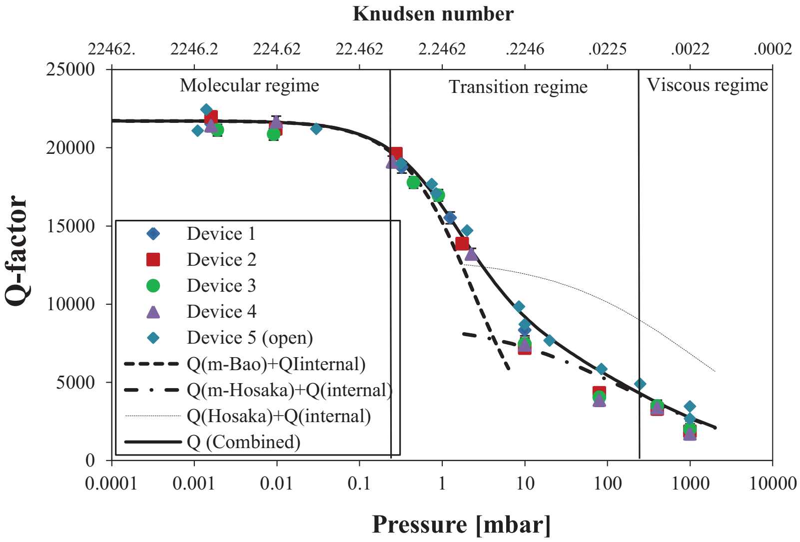

Figure 4.9: Experimental quality factors of four resonator devices versus the pressure. The dashed line is the model which includes squeeze-damping in the molecular regime. The dash-dotted line shows the Q-factor according the proposed viscous damping model and the dotted line shows the Hosaka's model. The solid line is the combined Q-factor.

At pressures above 1 bar the model starts to deviate from the experimental results, which is related to the transition to the viscous regime. In Figure 4.9 the viscous damping models after (4.29) and (4.30) are shown. Hosaka's model, which neglects the thickness D of the beams, significantly overestimated the quality factor of the tuning forks. In contrast, the experimental data was well correlated to the proposed model of (4.30).

To estimate the pressure in which the squeeze-film effects become important, the Knudsen layer may be considered. The thickness of the Knudsen layer denotes the distance from a moving structure in which the air is influenced by its motion and is, depending on the model, between 0.9 to 4.6 mean free paths [166]. This suggests that the Knudsen-layers of the two resonator tines overlap at pressures below 5-20 mbar, which lies in the transition regime. During the transition between molecular and viscous damping the dominance of one damping mechanisms is slowly replaced by the other. A heuristic approach introduced in ref. [175] for the combination of the quality factors of the two models in the form of $Q_{total}^{-1} = \left(Q_{internal}^{-1} + (Q_{viscous} + Q_{molecular})^{-1}\right)^{-1}$ was used. Although not physically meaningful this approach allows obtaining a good agreement between the model and the experiment over a large pressure range.

The effect of pressure on the resonance frequency was smaller than the experimental uncertainty in the molecular regime. Measureable variations only occurred at pressures

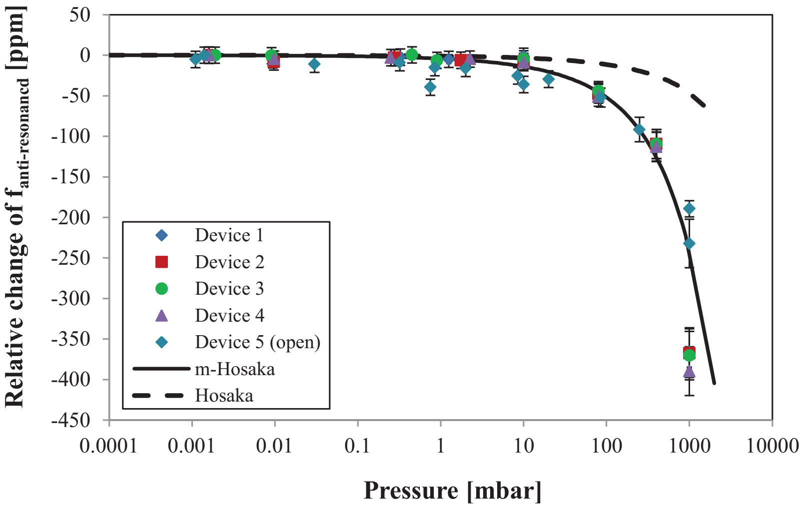

Figure 4.10: Relative change of the resonance frequency versus the pressure.

above ~100 mbar. The resonance frequency shifted by approximately 400 ppm between vacuum and ambient pressure, which corresponded to 55-60 Hz. Figure 4.10 shows the experimental data together with the calculation based on the proposed model which accounts for the rectangular cantilever cross-section (string-of-cylinders). The model was in good qualitative agreement with the experimental data, which indicated that reasonable estimations of the relative resonance frequency variations can be obtained using this approach. In contrast, the string-of-spheres model (Hosaka's model [165]) did not agree well with the experiment.

These results suggest that the proposed models are able to capture the characteristics of air damping in the framed tuning forks investigated in this work. Nevertheless, there are several aspects remaining open and of interest for future investigations: Firstly, only one type of resonators has been investigated in this work (in addition to the comparison with the experimental work by Zook et al. [180]). It would be required to assess the adequacy of the model also on other types of resonator geometries. Secondly, it must be noted that the model of squeeze film damping in the free-molecular regime is based on purely elastic and specular collisions. This assumption does probably not entirely correspond to the reality due to thermal accommodation and tangential momentum accommodation. Thermal accommodation means the probability (between 0 and 1) of a gas particle to equilibrate with the temperature (and hence velocity) of the surface during a collision. A model for full thermal accommodation has been proposed by Suijlen and co-workers [195], [196]. In their model the squeeze-film damping was considered as a variation of the pressure in the gap between a moving resonator and a static wall. However, their model is not applicable to the situation studied here because the pressure equilibration is much shorter than the oscillation period. In addi-

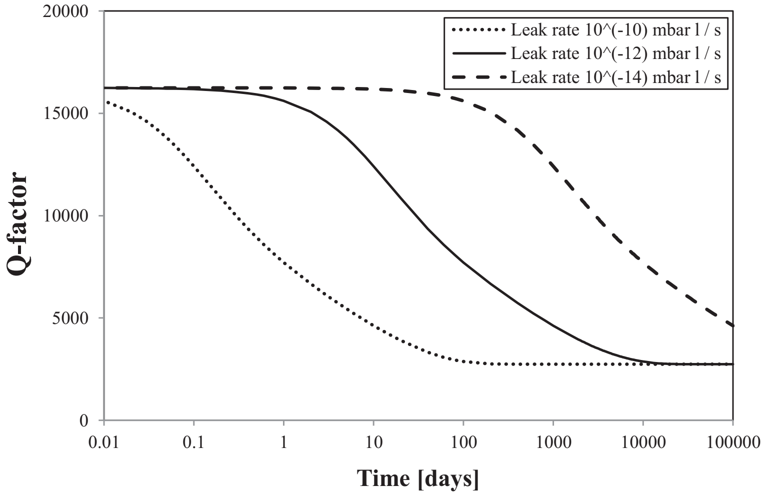

Figure 4.11: Q-factor of the encapsulated resonator as a function of time for three different leak rates. The curves are calculated based on the modeled Q-factor vs. pressure dependency and the pressure evolution for a starting pressure of 1 mbar and a given leak rate.

tion, full thermal accommodation does probably not reflect reality either. In literature thermal accommodation coefficients between 0.05 for H_2 on a silicon surface [197] and 0.96 for argon on various metallic surfaces [198] have been reported.

Tangential momentum accommodation coefficient (TMAC) relates to the proportion of diffusely reflected gas molecules (in contrast to specular reflection). The TMAC can take values between zero, where all impacts lead to specular reflection, and one, where only diffuse reflection occurs. As for the thermal accommodation, the results reported in literature are not fully conclusive. The TMAC also depends on the gas-surface pair, the roughness and the Knudsen number [166], [199], [200]. It would therefore be of great interest to investigate the influence of thermal accommodation and tangential momentum accommodation on the free-molecular damping. In addition, packaging under different gas atmospheres would be a promising approach for studying the dependence of the gas-surface pair on air damping.

Nevertheless, the model used here fitted the experimental data very well and can be used to estimate the leak-rate sensitivity, based on the above obtained Q-factor versus pressure relationship. For a cavity volume of 300 nanoliter, which is the internal volume of the piezoelectrically activated silicon resonators, and a hypothetical starting pressure of 1 mbar, the evolution of the pressure inside the cavity can be calculated for a given leak-rate. Based thereon the Q-factor was calculated. Figure 4.11 shows the Q-factor as a function of time for three different leak rates. Leak rates of 10^{-10} mbar l s^{-1} and 10^{-12} mbar l s^{-1} lead to a significant reduction of the Q-factor in the first days after encapsulation. For the case of a leak rate of 10^{-14} mbar l s^{-1} a change of the Q-factor could be detected after about three months, which still is a reasonable time-scale for reliability testing of devices which maintain a pressure during tens of years.

4.3 Chapter summary

In this chapter the influence of air damping on the quality-factor and the resonance frequency of tuning forks has been analyzed theoretically and experimentally from the free molecular regime to the viscous damping region. The pressure-sensitivity of the resonators was characterized by measurements of the resonance frequency and the quality factor as a function of the air pressure from 10^{-3} mbar to 1 bar. The resonators were found to be highly suited for leak rate measurement down to 10^{-14} mbar l s^{-1}.

A framework for the prediction of the resonance frequency and the Q-factor based on accessible geometrical and physical parameters was developed in the free molecular regime and the viscous regime. In comparison to the state-of-the art two main contributions were made. The first contribution is a further development of the molecular damping based on Bao's model [178]. In 2007 Hutcherson and Ye [179] have presented molecular dynamics simulations of squeeze-film air damping in microstructures. They have found that Bao's model underestimated the damping by a factor of approximately two caused by the underlying assumptions of Bao's model. In this work Bao's model is analytically refined and important effects previously neglected are included. This provided a simple analytical model for molecular squeeze-film damping and a significantly improved agreement with experiments was observed. The second advancement was made in the viscous damping regime. The 'string of beads' theory commonly used to describe the damping of microresonators in the viscous regime was adapted using a phenomenological correction factor to account for the rectangular cross-section of the beams, leading to the 'string-of-cylinders' model. The only unknown parameter of the models is the pressure-independent intrinsic damping coefficient, which cannot be predicted accurately, and needs to be assessed by experiment.

This chapter concluded the analysis of the mechanical properties influencing the resonance frequency and the quality factor of the piezoelectrically activated resonators, i.e. the materials mechanical properties, the strain distribution and the energy dissipation due to air damping. The models presented deepen the understanding of the air damping effects in the economically important tuning fork resonators and could support device design by allowing to predict the pressure sensitivity of MEMS resonators from vacuum conditions to high pressures, based on their geometry, the package and the utilized materials. However, clearly further efforts are required to assess the robustness of the model and its applicability to different device dimensions and geometries.

Chapter 5

Proton-Radiation Tolerance of Silicon and SU-8 as Structural Materials for High-Reliability MEMS

Following the discussion on the environmental challenges which must be faced in space applications in Chapter 2, the electrical characterization and strain analysis in the piezoelectrically activated microresonators in Chapter 3, and the analysis of the influence of the pressure level inside the cavity on the energy dissipation in the resonators, this chapter details the tests performed to investigate susceptibility of single crystal silicon to radiation-induced changes of the Young's modulus. The aim of the chapter is to investigate the radiation tolerance on the materials level, before the radiation tests on the system level will be discussed in the following Chapter 6. In addition to silicon also SU-8 was investigated, a commonly used structural MEMS material from the family of polymers.

Section 5.1 summarizes the radiation related effects in MEMS structural materials relevant in this context which were discussed in detail in Chapter 2. In section 5.2 the fabrication of the MEMS devices and the experimental setup for the dynamical characterization of the resonators is described. This section also contains the test conditions for the irradiations. Based on the selected proton energies and fluences the resulting absorbed doses were calculated. The results of the structural and dynamical investigations after irradiation are reported in section 5.3. This section also contains a discussion of the observations, in the context of reported radiation effects in silicon and polymers.

The essence of this chapter is published in T. Bandi, J. Polido-Gomes, A. Neels, A. Dommann, L. Marchand and H. R. Shea, *J. Microelectromech. Syst.*, vol. 22, no. 6, pp. 1395-1402, 2013 (© 2013 IEEE) and in T. Bandi, J. Polido-Gomes, A. Neels, A. Dommann and H. R. Shea, *Proc. SPIE*, 2013, pp. 86140M (© 2013 Society of Photo Optical Instrumentation Engineers).

The initialization of this activity by Dr. Joao Polido-Gomes and Prof. Dr. H. R. Shea is gratefully acknowledged. J. Polido-Gomes conducted the fabrication of the silicon and SU-8 devices as well as the planning and execution of the proton irradiation. The post-irradiation characterization of the silicon devices and the irradiation campaign of the SU-8 chips were carried out together with J. Polido-Gomes. The data analyses and writing of the above mentioned articles were then carried out by the author of this thesis.

5.1 Radiation related effects on structural MEMS materials

As outlined in Chapter 2, micro-electromechanical systems for applications in environments with high radiation levels must be fabricated from materials that are able to resist degradation by ionizing- and displacement damage mechanisms. Ionizing damage causes the formation of excitations and electron-hole pairs, inducing charge trapping or altering chemical bonding structures. If the momentum transfer to the target atoms is sufficiently high, displacement damage occurs, leading to structural defects in the atomic lattice. Protective shielding of microsystems could be envisaged but for radiation-sensitive systems this quickly becomes prohibitive in mass and size, outweighing the advantages of miniaturization.

Single crystal silicon is widely used as a structural material in MEMS. It is highly suitable for microsystems due to its versatility in fabrication and the high mechanical and chemical stability it offers. Radiation-induced damage has been investigated extensively in regards of its electrical properties. While being largely immune to ionizing damage, displacement damage has been reported to change minority carrier lifetimes and concentrations in electronic components. For a review on this topic see ref. [201]. However, in MEMS devices where silicon is used as a structural material, the functionality of the system is much more sensitive to changes in Young's modulus. As described in Chapter 2 the elasticity directly influences the vibrational modes of resonant structures which are standard building elements in MEMS devices. The mechanical properties are of particular interest in systems exploiting resonances for pressure-, acceleration- or rate-of-rotation- sensing, actuation of devices such as micromirrors or resonators for signal processing or conditioning. The accuracy of these systems is dependent on the stability of the vibrational modes over time (and hence radiation dose).

Related to radiation damage in single crystal silicon, it has been previously reported that the resonance frequency of micromirrors had changed shortly after proton irradiation of 1 MeV and 4.3 MeV protons at 100 Mrad total ionizing dose [9]. After three weeks the devices had recovered the resonance frequency prior to irradiation. This observation was explained by the introduction of defects which were mobile at room temperature and therefore annealed out after the irradiation. Surface-micromachined polysilicon resonator beams irradiated by gamma- and electron radiation have been investigated in [83], [84]. A decrease of the resonance frequency and an increase of resistance were observed. The results were attributed to a combination of displacement damage, injection annealing and thermal spike effects. The effect of fast neutrons on the electromechanical properties of several materials used in microsystems has been studied and reported recently [85].

A promising candidate for polymer MEMS is SU-8, which was first developed as a negative photoresist but it has quickly been recognized as a promising structural material [202]. The large number of crosslinking points in the precursor molecules lead to high chemical and mechanical stability of the cured resin. The curing reaction of the epoxy is initiated by exposure to UV, gamma-rays or proton radiation which allows the fabrication of very high-aspect ratios and 3D-structures [203], [204]. Due to its biocompatibility and mechanical elasticity it is a candidate for microfluidics, sensing and actuating applications [205], [206]. Radiation tolerance in polymer MEMS devices is often very limited and large changes of over 150% in the Young's modulus of Poly(methyl methacrylate) (PMMA) have been reported after irradiation with ^{60}CO gamma-rays and protons [207]. The effect of neutron irradiation on the hardness of SU-8 coatings, i.e. the ability of the material to resist plastic deformation, was investigated in [208]. No significant change of hardness was observed in the coating after irradiation. To the best of knowledge, no studies of the influence of proton radiation on the mechanical properties of SU-8 MEMS devices have been conducted to date.

The extent to which a space system is exposed to radiation can be modeled over the full lifetime of the system, taking into account the trajectory and the radiation shielding. The total ionizing damage dose absorbed by a space system shielded by 4 mm of aluminum is on the order of 1 krad/year in low Earth orbits and 10 krad/year in geostationary orbits [62]. The total dose level usually requested in the qualification testing of generic EEE parts is 100 krad [76]. For comparison, the expected ionizing dose of a tracking detector in the Large-Hadron-Collider at CERN is 1 Mrad, obtained after 1.5 years of operation, which is much higher than most space doses [77].

Protons were selected for the irradiation campaign because they are the most abundant ionic species of irradiation in space [65], as discussed in section 2.6. The energy of protons lies principally between 0.1 MeV and 400 MeV and they are more difficult to shield than electrons and heavier ions. SRIM 2008 [209] simulations show that protons of 10 MeV can penetrate 0.6 mm of aluminum. For MEMS material screening they offer the advantage of inflicting both ionization damage and displacement damage [62], [76].

5.2 Experimental

The resonance frequency is very sensitive to changes in the material elasticity as $\Delta f / f = 1/2 * \Delta E / E$ (see section 2.1). By monitoring the radiation-induced change of the resonance frequency, the change in Young's modulus was calculated. This method is an elegant way to investigate mechanical properties of materials in structures whose geometry, dimensions and fabrication processes are relevant and directly applicable to MEMS technology. For the purpose of isolating radiation-induced effects in the materials themselves, the device structures were designed such that no additional materials (dielectric, coils, etc.) were required for operation and characterization.

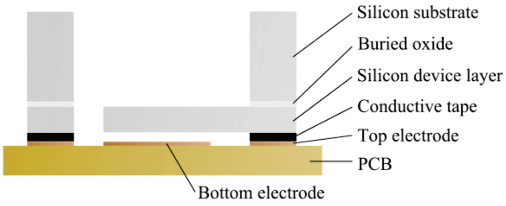

Figure 5.1: Schematic cross-section of the silicon resonator chips. The devices were placed with the device layer on the PCB. Conductive tape was used to attach the devices and to electrically connect the device layer for electrostatic actuation of the resonators. Design and fabrication by J. Polido-Gomes are gratefully acknowledged. (© 2013 IEEE)

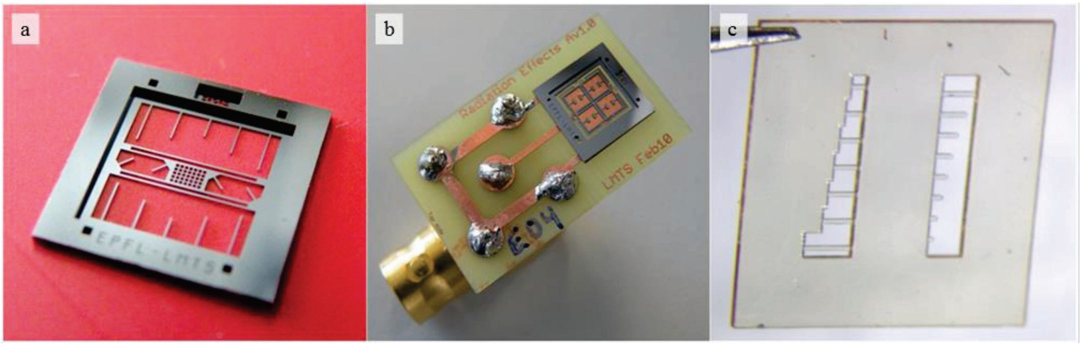

Figure 5.2: (a) One type of Single crystal silicon resonator chip (chip is 10 mm on a side, 14 cantilevers), (b) different chip with same outer dimensions mounted on a PCB. The PCB contains copper lines for electrostatic actuation of the resonators. (c) SU-8 resonator chip. The size of the chip is 9 mm x 9 mm. Only the longest and second-longest SU-8 resonators were used for this research. Design and fabrication by J. Polido-Gomes are gratefully acknowledged. (© 2013 IEEE)

To investigate the chemical structure of the SU-8 infrared spectroscopy was used. IR-spectroscopy exploits the fact that light with specific wavelength excites characteristic vibrational and rotational modes of chemical bonds and functional groups [210]. The absorption spectrum of a material therefore allows identifying the chemical bonds and functional groups which are present in the system. Attenuated-Total-Reflection FTIR (ATR-FTIR) vibrational spectroscopy measurements were performed using a Bruker Hyperion 3000 instrument. The infrared absorption was measured in the spectral range between 600 cm^{-1} and 4000 cm^{-1}. X-ray diffraction measurements were made on a PANalytical X'Pert Pro MRD instrument.

5.2.1 Fabrication of silicon cantilevers

Resonators with lengths of 1.5 mm and 2 mm, width 80 µm, and thickness 50 µm were fabricated on Si(001) silicon-on-insulator wafers. The chip substrate formed a frame enclosing an area of 1 cm^2. The resonators were patterned into the device layer, pointing inwards along the (110) crystal direction (Figure 5.2a). Standard lithography and deep reactive ion etching was used to form the resonators. Subsequently they were released by dry etching of the silicon substrate wafer from the backside followed by a hydrofluoric acid etching step to remove the buried oxide. As schematically depicted in Figure 5.1 the chips were placed on prited-circuit board (PCB) substrates for testing. The PCB plates were lined with copper electrodes for electrostatic actuation of the resonators. Table 5.1 summarizes the geometries of the resonators used. Figure 5.2a and Figure 5.2b show a single crystal silicon device chip and a silicon chip mounted on the PCB respectively. In addition to the clamped-free cantilevers also paddle-type resonators were used. This geometry consisted of a rectangular tab suspended by a cantilever arm (as shown in Figure 5.2b). Despite the differences in the geometry always the same component of the elastic modulus tensor was measured because all resonators were only operated in the first out-of-plane mode.

5.2.2 Fabrication of SU-8 resonators

The polymer devices were fabricated using commercial SU-8 (GM1075) obtained from Gersteltec. The fabrication process is schematically shown in Figure 5.3. A sacrificial layer of dextran was deposited on a silicon handling wafer. The devices were formed by spinning of SU-8 precursor onto the handling wafer, soft-baking at 95 °C, exposure to UV-light (200 mJ/cm^2) and subsequent post-baking at 120 °C. This process was repeated twice to first form the device layer with the resonators and then the chip substrate. After this the un-exposed SU-8 was dissolved in PGMEA (propylene glycol methyl ether acetate). The chips were released in de-ionized water and glued on a PCB for handling and testing. During the whole test campaign the SU-8 chips were not removed from the PCB support. Piezoelectric

Table 5.1: Dimensions and average resonance characteristics of the resonators tested. (© 2013 IEEE)

Resonator type	Material	Length (µm)	Width (µm)	Thickness (µm)	Clamping	Resonance frequency (kHz)	Quality factor in vacuum (p~10^{-3}mbar)
Cantilever	Si	2000	80	50	clamped - free	24.6	900
Cantilever	Si	1500	80	50	clamped - free	14.8	4200
Paddle	Si	Paddle area 0.18 mm^2 Arm length 800 µm Arm width 80 µm Arm thickness 50 µm			clamped - free	22.7	6100
Cantilever	SU-8	1000	120	100	clamped - free	32.6	35
Cantilever	SU-8	800	120	100	clamped - free	49.1	23
Cantilever	SU-8	1500	120	100	double clamped	86.0	19
Cantilever	SU-8	1000	120	100	double clamped	192.8	27

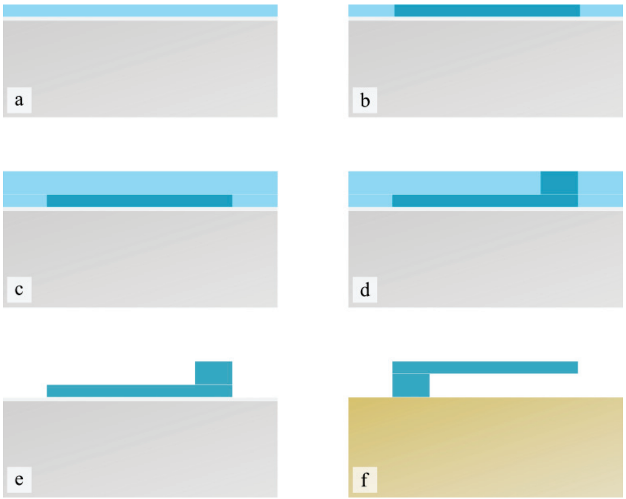

Figure 5.3: Schematic representation of the fabrication process of the SU-8 devices. (a) The process started with a silicon wafer that served as a substrate for the fabrication (gray). Next a sacrificial layer of dextran was deposited and the spinning of the first layer of SU-8 took place (in light gray and blue, respectively). (b) After soft-baking the first SU-8 layer was exposed to the UV-light to define the resonators. Then the post-exposure bake (PEB) was made. The exposed region is shown in dark blue. (c) Spinning of the second layer of SU-8 on top of the first layer. (d) Soft-baking and selective exposure to UV-light was made to form the body of the chip. This was followed by the second PEB. (e) The unexposed SU-8 was then developed in PGMEA. (e) The dextran layer was dissolved in de-ionized-water to release the chip. (f) For testing the chips were attached to a PCB by carbon-loaded tape. Design and fabrication by J. Polido-Gomes are gratefully acknowledged. (© 2013 IEEE)

elements obtained from NOLIAC A/S were used to actuate the SU-8 beams. The plate actuators (model CMAP 09) were 10 mm large, 10 mm wide and 2 mm thick. The tested resonators were 100 µm wide, 120 µm thick. Their lengths were 0.8 mm and 1.0 mm for the clamped-free resonators and 1.0 mm and 1.5 mm for the clamped-clamped beams (Table 5.1 and Figure 5.2c).

5.2.3 Resonance characterization

The dynamical response of the resonators to actuation was determined by Laser Doppler Vibrometry (LDV) using a Polytec MVS-400 instrument. A detailed description and characterization of the measurement setup has been reported previously [9]. During the resonance measurements the samples were placed inside a vacuum chamber ($p < 3.5 \times 10^{-3}$ mbar) and the temperature was kept constant at 45 ± 0.2 °C after a bake-out at 80 °C. Constant temperatures throughout all measurements were used to suppress the effect of temperature on the resonance frequency. The bake-out served to minimize the effects of humidity variations over the duration of the test campaign. A frequency resolution of 0.5 Hz was used on the silicon resonators and ≤ 200 Hz on the SU-8 resonators. This was mainly limited by the width of the resonance curves. The standard deviation of the resonance frequency in un-irradiated resonators was determined by repeated measurements and was below 0.05% for the silicon resonators and 0.5% in the SU-8 resonators. Typical resonance frequencies and quality factors of the resonators are shown in Table 5.1. The quality factor of the SU8 resonators was comparable to values of SU-8 microresonators reported in literature [211]. This indicates that the energy dissipation was dominated by the same mechanism as identified there, i.e. intrinsic material damping. The double-clamped cantilevers possessed quality factors similar to the single-clamped resonators, suggesting that they were not under large internal tensile stresses, which would result in string-like oscillation characteristics and higher Q-factors [211]. The absence of buckling caused by excessive compressive internal stresses was confirmed by white-light interferometry (Wyko NT1100).

5.2.4 Proton irradiation conditions

SRIM 2008 [209], [69] was utilized to simulate the effect of proton irradiation on the materials and to calculate the absorbed doses. The total ionizing dose (TID) was calculated from the ionizing (electronic) stopping power dE_e/dx:

$$TID\left[MeV/g\right] = \frac{dE_e/dx}{\rho} * \Phi \tag{5.1}$$

Φ is the particle fluence and ρ is the density. The Total Displacement Dose (TDD) was deduced based on the Non-Ionizing Energy Loss (NIEL) using the Kinchin-Pease relationship [212]:

$$TDD\left[MeV/g\right] = \frac{M(dE_n/dx)}{\rho} * \Phi \tag{5.2}$$

where

$$M = \frac{1}{1000}\left(\frac{T_n}{4} + 2\right). \tag{5.3}$$

T_n is the threshold energy for vacancy formation. In silicon T_n is 21 eV [212]. For polymers it is difficult to estimate the exact displacement damage threshold as they contain more than one type of chemical bonds but it typically lies in the range of 10-30 eV [213]. A value of 28 eV was used for SU-8. These calculations served as a basis for the selection of the proton fluences.

The irradiations were carried out in two campaigns at the Proton Irradiation Facility (PIF) of the Paul-Scherrer Institute (Villigen, CH). Each chip, containing several resonators, was irradiated under different proton radiation conditions.

Proton energies of 10 MeV and 60 MeV and fluences between 10^{11} cm^{-2} and 10^{13} cm^{-2} were used for the irradiation of the silicon resonators. The large fluences selected required an

Table 5.2: Irradiation parameters for the silicon devices. (© 2013 IEEE)

Sample	Proton energy (MeV)	Flux ($cm^{-2}s^{-1}$)	Fluence (cm^{-2})	TID (krad)	TDD (rad)	# Resonators tested
1	10	10^{11}	10^{13}	5900	1500	7
2	60	10^{9}	10^{11}	14	2	8
3	60	10^{10}	10^{12}	140	17	4
4	60	10^{11}	10^{13}	1400	167	7
Control	-	-	-	-	-	4

Table 5.3: Irradiation parameters of the SU-8 devices. (© 2013 IEEE)

Sample	Proton energy (MeV)	Flux ($cm^{-2}s^{-1}$)	Fluence (cm^{-2})	TID (krad)	TDD (rad)	# Resonators tested
1	10	10^{8}	10^{10}	7	1.4	4
2	10	10^{8}	10^{11}	74	14.1	3
3	10	10^{8}	10^{12}	740	141	3
4	19	10^{8}	3×10^{12}	1360	228	3
5	30	10^{8}	10^{10}	3	0.4	4
6	30	10^{8}	10^{11}	29	3.8	4
7	30	10^{8}	10^{12}	290	38.3	2
8	30	10^{8}	3×10^{12}	880	115	4
9	60	10^{8}	10^{10}	2	0.2	4
10	60	10^{8}	10^{11}	17	1.6	4
11	60	10^{8}	10^{12}	170	15.7	3
12	60	10^{8}	3×10^{12}	500	472	3
13	200	10^{8}	10^{10}	1	0.02	2
14	200	10^{8}	10^{12}	70	1.8	2
Control	-	-	-	-	-	3

adaptation of the dose rate, which was between 10^{9} cm^{-2} s^{-1} and 10^{11} cm^{-2} s^{-1}. Four chips were irradiated and 26 resonators were investigated in total. The activity of the samples abated to safe levels three months after proton irradiation, after which the post-irradiation measurements were carried out.

The SU-8 resonators were irradiated using protons of 10 MeV, 19 MeV, 30 MeV, 60 MeV, and 200 MeV and fluences between 10^{10} cm^{-2} and 3×10^{12} cm^{-2}. To prevent dose-rate dependent effects this parameter was equal for all samples (10^{8} cm^{-2} s^{-1}). The first measurement of the SU-8 resonators was made two weeks after irradiation, when the samples were released by the irradiation facility. Three months after the irradiation the dynamical characterization was repeated. 14 SU-8 chips were irradiated on which a total number of 45 resonators were tested. The irradiation conditions of the silicon and SU-8 devices are summarized in Table 5.2 and Table 5.3 respectively.

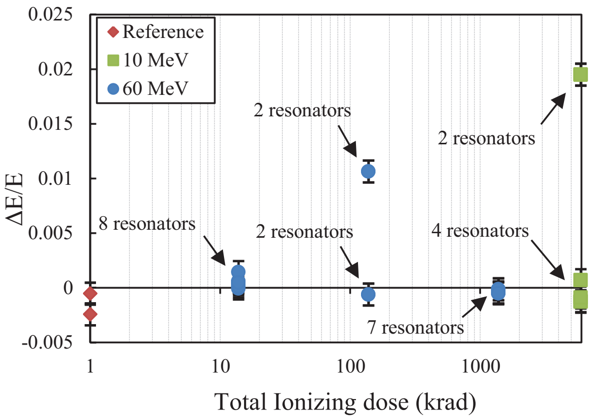

Figure 5.4: Relative change in Young’s modulus of the individual silicon cantilevers after 10 MeV and 60 MeV proton irradiation. For clarity the number of resonators is indicated where several measurement points overlap. (© 2013 IEEE)

5.3 Results and Discussion

5.3.1 Single Crystal Silicon

In the irradiated silicon no discoloration was observed. The results of the resonance characterization are summarized in Figure 5.4, which shows the relative change in Young’s modulus of the irradiated resonators.

Most of the resonators showed a *ΔE/E*-value similar to the measurement uncertainty, but in 4 resonators a larger deviation was measured. Two of these resonators were irradiated at 140 krad and two at 6 Mrad, but none at 1.4 Mrad. In both cases the resonators in question were not direct neighbors in the chip and the proton beam was much larger than the sample, thus a misalignment of the chip and the proton beam was ruled out as a possible reason for these observations. The deviation in the resonance frequency did not smoothly increase with the dose (notice the log-scale in Figure 5.4) and the values in question were heavily displaced from the majority of data points. Therefore these data points were probably rather related to experimental side effects such as airborne dust particles than to radiation-induced change of Young’s modulus. The variation of the quality factor tended to increase with the total dose, however, the data were not conclusive on this and clearly further experiments must be made to clarify the effect of radiation on the resonator damping. As the quality factors of the silicon resonators were large, changes of the damping had only a negligible effect on the resonance frequency. These results suggest that the Young’s modulus of single-crystal silicon was not significantly altered by proton fluences of up to 10^{13} cm^{-2} which corresponds to a dose of 5900 krad TID for 10 MeV protons.

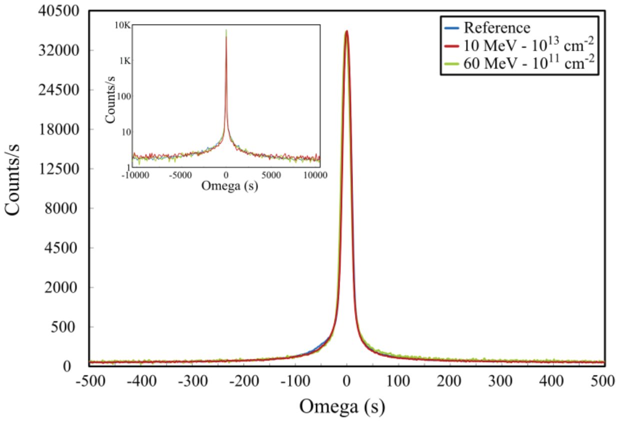

Figure 5.5: HRXRD diffractogram of (004)-reflection of the silicon samples. The graphs shows RC measurements (ω-scans) in the vicinity of the Bragg peak. The FWHM of the reflections is 0.0045°. The inset shows a wide ω-scan using a larger step size. Within the experimental uncertainty no significant difference in the diffraction patterns was observed. (© 2013 IEEE)

It can be pointed out that the doses used in this study were about 100 times higher than typical space qualification levels and that possible degradation effects would be expected to be amplified accordingly.

The effect of proton irradiation on the crystal structure was investigated by high-resolution x-ray diffraction. The shape and width of the 004-Bragg peak were analyzed. These properties depend on the quality of the crystal, i.e. the concentration of structural defects such as dislocations, vacancies and interstitials and on strain gradients. Figure 5.5 shows the Si(004) diffraction peak before and after irradiation, both near the vicinity of the Bragg reflection and in a wide-range scan (inset). Neither an increasing diffuse scattering, a peak broadening nor the appearance of a peak asymmetry indicating additional crystal defects or strain gradients were observed.

This indicated that the proton irradiation did not introduce significant amounts of stable lattice defects unlike heavier ion irradiations as reported before in ref. [59]. In that work the effect of irradiation on single-crystal silicon resonant structures was investigated in devices irradiated by 5.5 MeV alpha-particles (originating from an ^{241}Am source) to a total fluence of only approximately 8.7 x 10^{10} cm^{-2}. The diffuse scattering observed near the Si(224) reflection was attributed to displacement damage. The projected range of 5.5 MeV He^{+} of silicon is 27 μm which is inside the device layer. The high stopping power at the end of the ion trajectory leads to higher defect concentrations and terminal subclusters [201] where larger and more stable defects are formed [214]. However, due to the large stopping power, these He-ions would not reach MEMS inside a spacecraft.

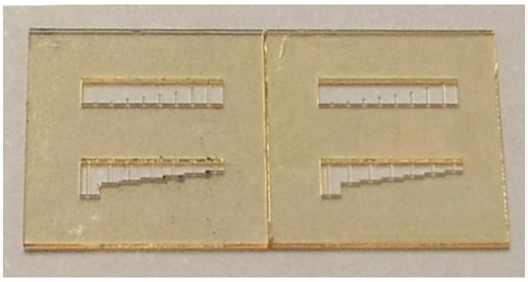

Figure 5.7: Comparison between irradiated SU-8 chip and a reference sample. The left chip has been irradiated by 30 MeV protons and a total fluence of 10^{10} cm^{-2}. The size of the chips is 9 mm x 9 mm.

5.3.2 SU-8

No discolorations were observed after irradiation of the polymer samples (Figure 5.7). The changes in resonance frequency after irradiation were in the range of -2.7% to 2.1% (maximum positive and negative change measured in any of the resonators). This corresponded to a variation of the Young's modulus between -5.4% and 4.2%.

In agreement with observations of the effect of irradiation on polymers reported in literature [213], [215], the effect of radiation on SU-8 could not be simply related to the total ionizing dose or to the total non-ionizing dose. The left graph in Figure 5.6 shows the relative change in elasticity versus the proton fluence. No clear trend with regards to the particle fluence was observed (Left graph of Figure 5.6). However, the evolution of the resonance frequency was found to be correlated with the proton energy and the electronic stopping power.

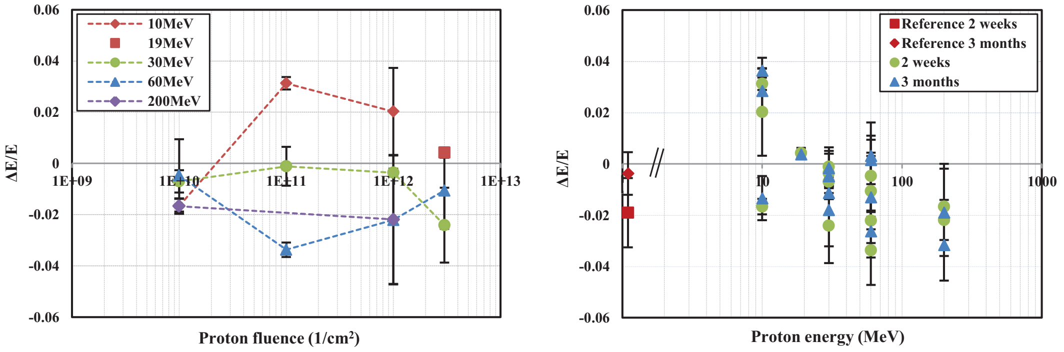

Figure 5.6: Change in Young's modulus (average and standard deviation of all measured resonators on one chip) of SU-8 resonators after proton irradiation. The left graph shows the changes versus the proton fluence. The dashed lines are a guide for the eye. The right graph shows the change in elasticity versus the proton energy, (●) 2 weeks after irradiation and (▲) 3 months after irradiation. Points with equal proton energy are devices irradiated at different total fluences. (© 2013 IEEE)

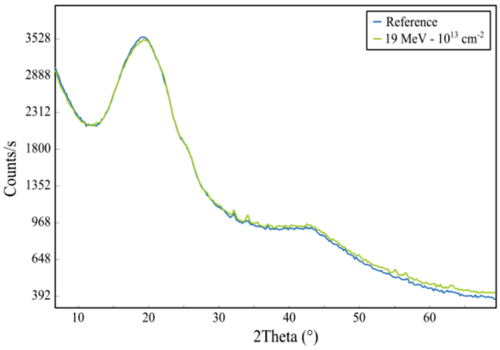

Figure 5.8: X-ray diffraction pattern of SU-8. The figure shows an un-irradiated sample (blue) and a sample irradiated at 3 x 10^{12} cm^{-2} at 19 MeV proton energy. No change in the diffraction pattern was observed after irradiation. The faint peaks at 32° and 34° are artifacts from the sample holder.

Figure 5.6 right, shows the relative change in elasticity versus the proton energy. The data points with equal proton energy are the samples irradiated at different total proton fluences. At proton energies of 30 MeV and higher, a softening of the material was observed (negative $\Delta E/E$). At the lowest proton energies (10 MeV and 19 MeV) the Young's modulus was increased. An exception to this general observation was the sample irradiated at 10 MeV and 10^{10} cm^{-2}, where a softening was observed.

The threshold energy for the crossover from positive to negative $\Delta E/E$ was 20-25 MeV which corresponded to a stopping power of approximately 3 eV/nm. Although the quality factors of the SU-8 resonators were lower than in the silicon resonators, the variation of the quality factor did not significantly influence the resonance frequency shifts.

5.3.2.1 Data from the SU-8 control samples

On the proton-irradiated chips the average and standard deviation of the change in $\Delta E/E$ between the measurements 2 weeks and 3 months after the irradiation was 0.003±0.006. However, on the control chip this difference was -0.015 (see left graph of Figure 5.6), which is larger than in any of the irradiated chips. This was caused by one of the three resonators on the control chip which showed a large change of the resonance frequency between the measurements. It is not possible to prove with certainty whether this was a genuine result or if it may have been caused by a dust particle lying on the resonator. However, it can be noted that this effect was transient and that the other resonators on the control chip were not showing such a behavior.

5.3.2.2 X-ray diffraction and IR-spectroscopy

SU-8 was investigated by x-ray diffraction and by ATR-FTIR spectroscopy. The amorphous structure of the polymer was confirmed by x-ray diffraction, as shown in Figure 5.8. A halo (near-order) peak was observed at 2-Theta angles in the range of 18-20°. No difference in

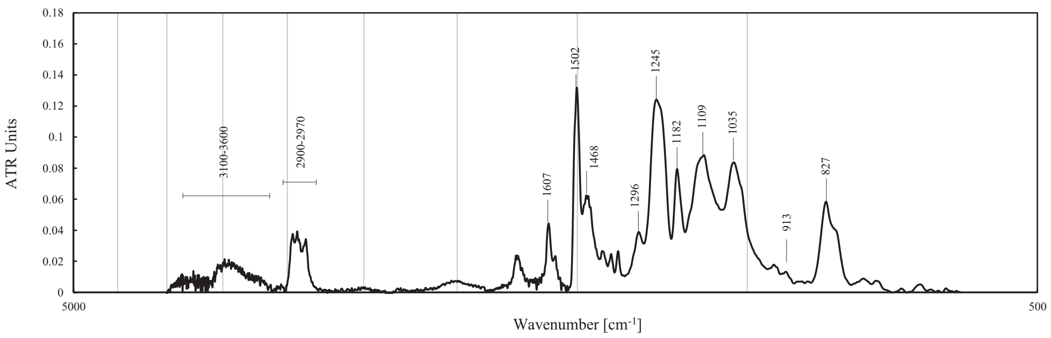

Figure 5.9: Infrared absorption spectrum of an un-irradiated SU-8 sample.

Table 5.4: Infrared spectroscopy peak assignment for SU-8. The peaks were assigned following [216] and [217].

Peak wavenumber [cm^{-1}]	Assignment
3100-3600	O-H stretch (water)
2860-2980	Aliphatic C-H stretches
1610, 1500	Aromatic ring C-C stretch modes
1470	CH_2 bend (scissoring)
1390, 1365	Aliphatic CH_3 doublet bends
1295, 1180	Aliphatic C-O stretches
1250, 915, 860	Epoxy ring modes
1245	Phenol C-O stretch
1110	Aliphatic C-O stretch (ether bond)
1035	Aromatic C-H in-plane bend
830	Aromatic C-H out-of-plane bend
660	Aromatic C-C out-of-plane bend

the diffractograms was observed after irradiation. This indicates that no crystallization occurred and that the near-order structure of the polymer remained unchanged by the radiation.

It has already been reported by various authors that FTIR spectroscopy was used to support the optimization of SU-8 fabrication parameters, such as temperature, ramp rates and duration of soft bake and post-exposure bake as well as the exposure dose [216]-[218]. Also it has been shown that FTIR can support the functionalization of SU-8 surfaces with various molecules for bio-MEMS [219], [220]. Figure 5.9 shows the ATR-FTIR absorption spectrum of an un-irradiated SU-8 control sample. Its peak positions and intensities were in qualitative agreement with works reported in literature and were assigned to the chemical groups according to Figure 5.9 and Table 5.4, based on the analyses made in refs. [216] and [217].

The peak at 918 cm^{-1} which was attributed to the epoxy rings was found in the polymerized SU-8, indicating that the cured SU-8 still contained epoxy groups, which had not reacted during the post-exposure bake. The other two epoxy modes were near other IR bands and

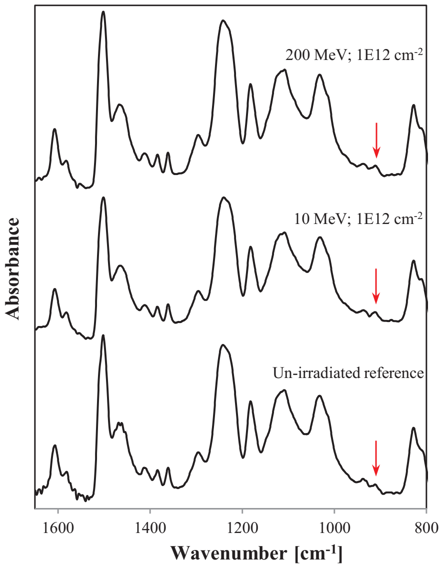

Figure 5.10: Comparison of the IR spectra of an un-irradiated SU-8 chip and two irradiated specimen. The spectra are offset vertically for clarity. The red arrow shows the position of the peak at 918 cm^{-1} which was attributed to the epoxy rings.

were therefore not clearly discernible. The presence of epoxy groups in the cured resin is in agreement with the findings reported in [219] where it was observed that the epoxy peaks did only completely disappear after an extended hard bake of 16 hours at 200 °C. In [219] residual epoxy groups at the surface of the cured SU-8 were used as attachment points for functional layers. The concentration of residual epoxy groups was enough to allow the formation of coatings which enabled cell adhesion and growth. In the irradiated SU-8 specimen no additional peaks or significant changes of the IR absorption spectrum were observed (Figure 5.10). The peak at 918 cm^{-1} which was attributed to the epoxy rings was also present in irradiated samples and its intensity had not significantly changed. This suggests that the irradiation did not lead to heavy disintegration or modification of the polymer structure.

5.3.2.3 Radiation-induced degradation in polymers

In this paragraph radiation-induced degradation mechanisms in polymers are briefly reviewed and then the observations on the SU-8 samples are discussed in this context.

Changes in the structural properties of polymers are caused by ionization, radical formation and atomic displacement. All of these processes can lead both to chain scissioning and cross-linking [213]. The chemical structure of the polymers determines the susceptibility to radiation damage and the dominance of specific radiation effects. For instance, aromatic compounds act as energy sinks due to the electronic delocalization. Transfer of energy from excited species to aromatic compounds thus effectively reduces the energy available for

Table 5.5: Parameters of proton-irradiation damage in SU-8: Column1 contains the electronics stopping power and column 2 the nuclear stopping power. These parameters were calculated using SRIM 2008. (© 2013 IEEE)

Radiation	dE_e/dx (eV/nm)	dE_n/dx (eV/nm)
10 MeV H^+	5.6	1.0×10^{-3}
30 MeV H^+	2.2	2.9×10^{-4}
60 MeV H^+	1.3	1.2×10^{-4}
200 MeV H^+	0.5	1.4×10^{-5}

chemical damage [221]. The average SU-8 precursor molecule is based on four ‘Bisphenol-A’-like subunits, each of which contains two aromatic rings. This may contribute to the good radiation tolerance of SU-8. Energy dissipation in the form of heat increases the mobility of active species and can influence the defect formation and annealing as well as the chemical reactions occurring. A significant heating effect during the irradiation of SU-8 was ruled out by analysis of the SRIM stopping power calculations: Under the (unlikely) assumption that all ionizing energy was transformed into thermal energy and that the full dose was applied instantaneously the change of temperature at the highest fluences was 19 K in SU-8 (80 °C in the silicon devices).

The degree of damage imparted by electronic and nuclear stopping depends on the mass and energy of the impinging particles. Table 5.5 shows the stopping powers of protons in SU-8, as determined from SRIM calculations. The highest vacancy formation rate due to the passing H^+-ions and the recoil atoms occurred at 10 MeV and was $\sim 10^{-5}$ vacancy/nm. Thus, although the nuclear displacement leads to chain disruptions and therefore can contribute to structural modifications, the effect of nuclear damage was very low in the present case and was assumed to be negligible in the tests.

Electronic stopping causes the formation of excited and ionized species. The susceptibility of polymers to irradiation has been reported to be dependent on the extent of electronic stopping power dE_e/dx i.e. the amount of energy converted to excitations and ionization per unit path length of the particle trajectory (similar to the effect of ionizing damage in dielectrics as discussed in section 2.6). Such observations are also referred to as ‘LET effects’ as the total stopping power dE/dx is closely related to the linear energy transfer (LET). The LET describes the energy loss from the perspective of the particle, whereas the stopping power is a measure of the energy absorbed by the material. LET-dependent radiation effects, in which the observed damage is correlated to the electronic stopping power of the radiation were investigated in various polymers including aromatic and aliphatic compounds [213], [215], [222], solid alanine [223] polystyrene and polysilanes [224], [225]. However, [226] reported similar effects on the elongation to break in Ultem and Kapton irradiated by three different types of radiation, namely 3 MeV protons, 2 MeV electrons and gamma-rays. Thresholds for the appearance of LET effects were also reported. In PMMA the critical LET value was found to be 15 eV/nm. Below the threshold LET the scissioning efficiency was fairly constant. At higher stopping powers the scissioning efficiency was reduced [213], [215], which was related to elevated crosslinking efficiency due to higher ionization densities. LET thresholds were observed to be lower in aromatic polymers than in aliphatic compounds [222], [227].

LET effects have been explained by overlapping of ion tracks (inter-track effects) or by interactions between ionization events caused by the same ion (intra-track effects). The onset of track overlapping has been reported to occur at fluences of 10^{12} cm^{-2} to 10^{13} cm^{-2}, depending on the particle LET [215], [223], [228]. As deviations of the Young's modulus were already observed at lower fluences in this work, it was assumed that the observed change in elasticity was related to the concentration of ionizations within single tracks and the following scenario appears to be most realistic: At high energies, i.e. lower stopping powers, the ionizations were isolated events and chain-scissioning dominated. Lower energy protons which deposited more energy in their track created higher concentrations of active species and favored crosslinking. The threshold for the dominance of one over the other process was found to be at proton energies of 20-25 MeV (see right graph in Figure 5.6), corresponding to a stopping power of approximately 3 eV/nm. This value is comparable to the findings of a previous study of poly(di-n-hexylsilane) where a threshold value of 10 eV/nm was reported [225].

Although the LET is a valuable concept for quantifying the energy deposited in ion tracks, it ignores the density distribution of the absorbed energy, which determines the distribution and concentration of active species in the material [224]. A theory which allows estimating the track radii of ions in water has been proposed in [229]. In this approach the energy distribution around the track is considered to be separated into the 'core' and the 'penumbra' regions. The radius of the core region delimits the area in which the initial electronic excitations occur. Creation of secondary electrons (δ-rays) leads to a transport of energy into the penumbra region. The total average energy density $\rho(r)$ deposited within a specific radius r around the ion track is [225]:

$$\rho(r) = \frac{LET}{\pi r^2}\left\{1 - \frac{1}{2}\left[\ln\left(\frac{e^{1/2} r_p}{r_c}\right)\right]^{-1} \ln\frac{r_p}{r}\right\} \tag{5.4}$$

The core and penumbra radii are denoted by r_c and r_p respectively and e is an exponential factor. In a given target the variables r_c, r_p and e depend on the particle velocity only and were given for water in ref. [229]. Figure 5.11 shows $\rho(r)$ for the proton irradiation at the energies used in the irradiation campaign (assuming that the parameters given in [229] are valid in SU-8 as well). In the single-track model the threshold proton energy of 20-25 MeV corresponds to a $\rho(r_c)$ of 0.09-0.12 eV/nm^3. In case track overlapping had played a significant role, the actual energy density threshold could be higher because of the accumulation of energy and active species by several ions passing the same volume.

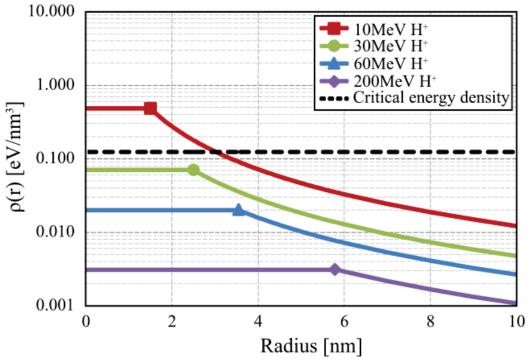

Figure 5.11: Average density of energy deposition around particle track of different proton energies. The track core radius r_c is shown as a filled circle. Inside the track core radius the energy density is homogeneous. At higher radii the energy density is determined by secondary electrons and decreases monotonically.

However, it is argued here that the critical energy density $\rho(r_c)$ obtained by the single track model explains the obtained results best, as explained in this paragraph. A model for estimating the probability of track overlapping has been proposed in [230]. The total fractional area covered by ion tracks [224] and the probability of n-fold track overlapping is calculated based on the track cross-section and the total fluence. Applying this approach to the data (setting the track radius to r_c) indicates that at the lowest fluences (10^{10} cm^{-2}) track overlapping was negligible at all proton energies. For the 10 MeV protons a significant hardening was already observed at a fluence of 10^{11} cm^{-2} at which less than 3% of tracks were overlapping. At a fluence of 10^{12} cm^{-2} the track overlapping was over 99% for the 200 MeV protons and 25% for the 10 MeV protons, reflecting the different track sizes. Other publications reported the track overlapping to occur at fluences of 10^{12} cm^{-2} to 10^{13} cm^{-2}, depending on the particle LET [223], [228], [215]. This suggests that at high proton energies and high fluences track overlapping did occur, however, the accumulated energy density was still below the threshold for the dominance of cross-linking over scissioning.

It is of value to also compare the critical energy density with the polymerization reaction of SU-8: the activation energy for the SU-8 polymerization has been reported to be 14.56 kJ/mol [231]. This corresponds to 0.15 eV per monomer. The density of SU-8 is 1218 kg/m^3 [232] (of which 10 wt% photoacid [202]) and the average molecular weight of one SU-8 unit is 1.4 kDa (assuming an average molecular formula of $C_{88}O_{16}H_{100}$). The volume taken by a single unit of SU-8 therefore is approximately 2.2 nm^3 and the threshold energy density deposited on a single SU-8 monomer is 0.15 eV / 2.2 nm^3 = 0.07 eV/nm^3. An underlying assumption is that the solvent content of the final polymer is negligible. This estimation shows that the activation energy density for polymerization is on the order of the critical energy deposition density $\rho(r_c)$ which was determined from the change in elasticity in the irradiated SU-8 samples as shown above. One possible hypothesis is that the proton irradiation could have caused stiffening in the material by inducing further epoxy crosslinking reactions. Such a mechanism would require the presence of epoxy groups in the hardened resin. This is supported by the FTIR-spectroscopy measurements (Figure 5.9 and Figure 5.10) in which the peak assigned to the epoxy groups was present in the cured resin.

Although this scenario qualitatively fits the experimental observations and is in agreement with concepts reported in literature, several uncertainties remain. For instance, the change in Young's modulus was correlated with the proton energy but at a given energy no clear trend with the proton fluence was found. In addition, the observed effects were small ($|\Delta E/E| \leq 5.5\%$), not much larger than the experimental variance. Therefore more detailed investigations would be required to clarify the fundamental processes by which proton radiation interacts with SU-8.

5.4 Conclusions

In the presented experiments the susceptibility of the Young's modulus of single crystal silicon and SU-8 MEMS structures to proton radiation damage was systematically investigated. Microfabricated silicon resonators were irradiated with proton beams of energy 10 MeV and 60 MeV and doses up to 10^{13} cm^{-2}. No changes in the resonance frequency or Young's modulus were observed. Investigations using high-resolution x-ray diffraction methods did not indicate the presence of elevated levels of structural defects or strain gradients within the material. The obtained results thus suggest that the elasticity of single crystal silicon is highly stable at proton radiation levels comparable to many years in most orbits around the Earth.

The Young's modulus of SU-8 was found to vary less than ±5.5% at proton fluences of up to 3 x 10^{12} cm^{-2}. A correlation of the sign and degree of change in elasticity with the proton energy was observed. It was put forward that this is related to the radiation stopping power and the energy which is deposited in the ion tracks and a possible model for explaining the experimental results was proposed. In this approach the dominance of either cross-linking or scissioning was related to the energy deposited in the ion tracks. Chain-scissioning dominated above the threshold energy of 20-25 MeV whereas at lower energies the stopping power was sufficiently high to establish active species concentrations which allowed further crosslinking. Further investigations are required to clarify the processes on the molecular level. Nevertheless, the SU-8 resonators remained intact and fully functional, showing that the polymer is highly tolerant to proton irradiation.

The measurement of the dynamical properties of micro-resonators is a powerful method for the investigation of material properties in structures relevant to microsystems technology. This work shows that single crystal silicon and SU-8 are tolerant to high doses of proton radiation and are very well suited for MEMS in space applications. The selected geometry, fabrication process and operation mode add to the relevance and allow for transferability of these results to other types of MEMS devices.

Chapter 6

Susceptibility of Piezoelectrically Activated MEMS to Radiation Damage and Mechanical Loads

With the encouraging results from the radiation tests on the single-material resonators in mind, this chapter takes the step from the material level to the system level. The reliability analyses which were performed on the piezoelectrically activated tuning fork resonators presented in Chapter 3 are reported in the following.

The relevant radiation conditions for space applications and the consequential choice of radiation sources have been discussed in section 2.6. The next section contains the detailed specifications of the radiation and mechanical tests which were selected for the environmental test campaign. At the end of this chapter the results are presented and discussed.

The essence of this chapter is published in T. Bandi, J. Baborowski, A. Dommann, H. Shea, F. Cardot and A. Neels, *Proc. SPIE*, 2014, pp. 89750I (© 2014 Society of Photo Optical Instrumentation Engineers).

6.1 Environmental test conditions

The materials in the piezoelectrically activated silicon resonators which were supposedly most susceptible to radiation damage are the silicon-dioxide and the piezoelectric AlN. Charge accumulation in these layers could lead to biasing of the piezoelectric material. This would reduce the driving force of the actuator and thus higher driving voltages would be required to drive the resonator. Trapped charges in the piezoelectric layer could affect the resistance and capacitance of the AlN. With regards to the silicon which makes up for the bulk of the tuning fork tines and dominates their mechanical properties, a displacement-damage induced change in Young’s modulus may be possible. However, as described in Chapter 5 experimental evidence suggests that single-crystal silicon is highly resistant to such an effect.

6.1.1 ^{60}Co Total Ionizing Dose test

The irradiation of the resonators with γ-rays from a ^{60}Co-source was carried out to study the susceptibility of the devices to ionization damage and charge trapping in the functional layers. The radiation campaign was conducted following a radiation test plan based on the ESCC radiation test procedure [76]. A total number of 28 devices were irradiated and 3 devices were used as a non-irradiated control group. The total ionizing doses to which the devices were exposed ranged from 3 krad(Si) to 170 krad(Si). Four samples were irradiated at each irradiation level. Biasing can significantly influence the radiation tolerance of microsystems because the electric field influences the probability of initial recombination of electron-hole pairs and the buildup of charge in dielectrics [67], [233]. To test different bias conditions, two devices in each group were floating (non-defined potential) and two were biased at 50mV (defined potential), which corresponds to the AC voltage applied during operation.

The devices were electrically characterized directly after the irradiation. The electrical characterization was subsequently repeated after one week and after 4 weeks. The devices were annealed at room temperature between the measurements.

6.1.2 Proton irradiation

Proton irradiation simultaneously inflicts ionizing and non-ionizing damage as discussed in section 2.6. For radiation tests with protons it is essential to ensure that the protons fully penetrate the device package and reach the radiation-sensitive parts. The penetration depth increases with the ion energy. On the other hand, the stopping power, which (along with the flux) determines the duration of the irradiation, is inversely related to the ion energy. Therefore, a compromise needed to be found with regards to the penetration depth, the relevant energy range and the stopping power.

Using SRIM-2008 [209] the proton irradiation of the packaged devices was simulated. In this model the sample structure consisted of a simplified material stack of 0.5 mm Pyrex, 20 µm air and 0.48 mm Silicon. The resonators were located at the surface of the silicon layer, right below the air gap. A proton energy of 50 MeV resulted in full penetration of the protons into the device and over 99.9 percent of ions fully crossed the simulated layers (Figure 6.1). In the simulations 10^6 ion impact events were calculated. The effect of the cap was to reduce the energy of the protons on their trajectory towards the silicon microresonator due to the energy losses in the Pyrex. As the stopping power increases with decreasing ion energy, the energy loss in the silicon was slightly higher in the shielded devices than it would be in directly irradiated silicon (Figure 6.2). However, the difference of only 2% lied within the uncertainty of the beam flux and energy, therefore the effect of shielding by the cap was negligible. Adding the AlN and the other functional layers had an even smaller influence on the stopping power of the protons (<< 1%).

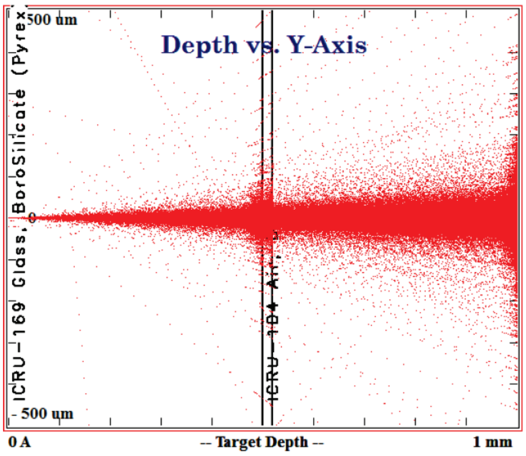

Figure 6.1: Results from SRIM 2008 simulations of the MEMS package, showing the trajectories of the protons hitting the sample. The protons enter the sample cap at $x = 0$ and then penetrate the device (0.5 mm glass / 5 µm air gap and 0.48 mm silicon).

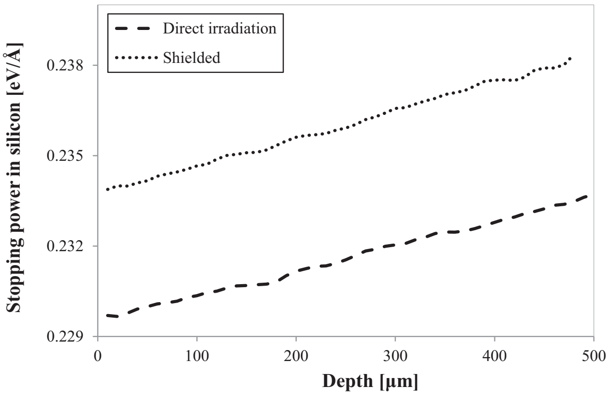

Figure 6.2: Comparison of the stopping power [eV/A] of directly irradiated silicon (dotted line) in comparison with the silicon microresonator under the Pyrex cap (dashed line).

In total, 19 resonator devices were used for the irradiation campaign. They were repartitioned into 6 sample groups which were irradiated at different doses (Table 6.1). One sample group was used as an un-irradiated reference. The MEMS components were floating during the irradiation and the post-irradiation annealing. In each sample group (except group 2) one device was biased at 200 mV during the irradiation.

The proton flux was approximately 1 x 10^8 p^+ cm^{-2} s^{-1} and the proton energy was 50 MeV. At these conditions the stopping power (i.e. the energy deposited per unit path length) was 0.23 eV/Å near the irradiated surface (Figure 6.2). The corresponding dose rate of 16 rad/s resulted in an irradiation time of 62 s for 1 krad.

Table 6.1: Sampling of piezoelectric resonators in the proton irradiation

	Proton energy (MeV)	Flux ($cm^{-2}s^{-1}$)	Fluence (cm^{-2})	TID (krad)	# Resonators tested	Comment
Group 1	50	1×10^8	6.3×10^{10}	10	4	1 biased (200mV)
Group 2	50	1×10^8	1.3×10^{11}	20	2	
Group 3	50	1×10^8	2.5×10^{11}	40	3	1 biased (200mV)
Group 4	50	1×10^8	5.0×10^{11}	80	4	1 biased (200mV)
Group 5	50	1×10^8	9.5×10^{11}	150	3	1 biased (200mV)
Group 6	-	-	-	-	3	Control

The electrical characterization of the devices was made directly after the irradiation and repeated 3 days and 2.5 weeks thereafter. Between the measurements the devices were annealed at room temperature.

6.1.3 Mechanical tests

The aim of the mechanical vibration and shock tests was to evaluate the stability of the devices under the mechanical loads which may be encountered during assembly, transport and operation. For space applications the most significant events occur during take-off, stage-separation and landing. The test procedures carried out were based on the ECSS standard *ECSS-E-10-03A* [89] and the Military Standard 883H [234].

The effect of mechanical shock on the functioning of the resonators was tested using a L.A.B SD-10 free fall shock tester. The specifications of the test procedure are shown in Table 6.2. For both directions of three orthogonal axes the samples were subjected to three consecutive shocks so that the total number of shocks at every test level was 18. After each shock level the samples were optically inspected and electrical impedance measurements were carried out.

After the mechanical shock tests the devices were exposed to mechanical vibrations, which were based on the ECSS test standard [76]. For each of three orthogonal axes the devices were tested with sinusoidal vibrations followed by random vibrations. Sinusoidal vibrations were applied in the frequency range between 5 Hz and 100 Hz. The test frequency was swept from 5 Hz to 100 Hz and back at 2 octaves per minute and the acceleration parameters used are defined in Table 6.3. In the frequency range between 20 Hz and 2000 Hz random vibration was applied. A root mean square acceleration of 37 g was imposed during 2.5 min for each axis. The vibration tests were conducted on a TIRAvib TV 50350 instrument.

Table 6.2: Parameters of the mechanical shock tests

Test level	Peak acceleration [g]	Pulse duration [ms]
1	500	1
2	1500	0.5
3	2000	0.3
4	3500	0.3

Table 6.3: Parameters of the sinusoidal vibration tests. The test was made without notching. The parameters were adopted from the ECSS-E-10-03A standard [89].

Frequency [Hz]	Test level
5-21	22 mm (peak-to-peak)
21-60	20 g (0 - peak)
60-100	6 g (0 – peak)

6.2 Results

No change of the optical appearance was observed after the irradiation tests. The resonance characteristics of the devices after ^{60}Co irradiation and after proton irradiation are shown in Figure 6.3 and Figure 6.4, respectively. In both figures the left graph displays the relative change of the resonance frequency while the right graph shows the absolute change of the quality factor, relative to the state before irradiation. Each data point in the graphs corresponds to one resonator measured at one time after the irradiation. The areas shaded in gray limit the values which lie within one standard deviation of the repeatability of the measurement technique[13].

The irradiation did not induce a significant change in any of the measured parameters neither for the proton irradiation nor for the γ -rays. No difference was found between the floating and the biased devices. Moreover also after one week and after four weeks no deviations in the resonances were observed.

Although the resonance frequencies and quality factors measured after irradiation were mostly within one standard deviation of the experimental repeatability, the irradiated devices showed a higher scattering of the measurement points than the control specimen, especially

---

[13] This mode of presenting the data was chosen in order to optimize the readability of the graphs. The width of the shaded area corresponds to the error bars on each of the measurements, hence the data points within this area did not differ from the initial value by more than the repeatability uncertainty.

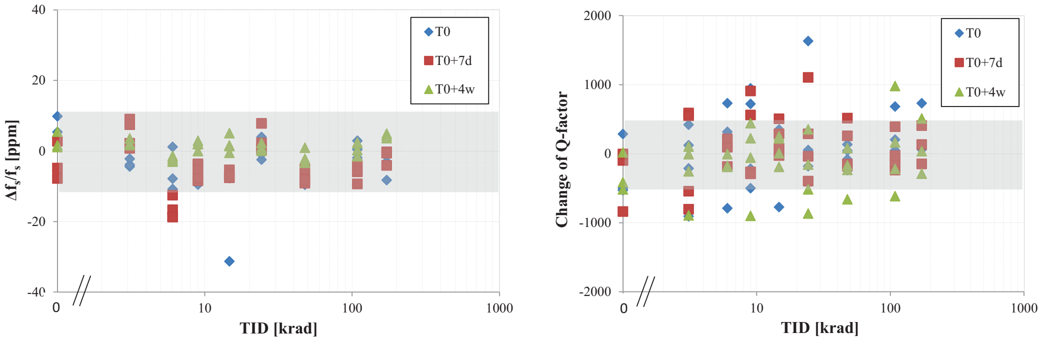

Figure 6.3: Resonance characteristics of the tuning fork resonators after irradiation with ^{60}Co γ-rays. The x-axis denotes the absorbed dose. (Left) Relative change in the serial resonance frequency (Right) Absolute change of the quality factor, relative to the pre-irradiation value, which was about 20000. (◊ Directly after the irradiation, □ 7 days after the irradiation, and Δ 4 weeks after the irradiation).

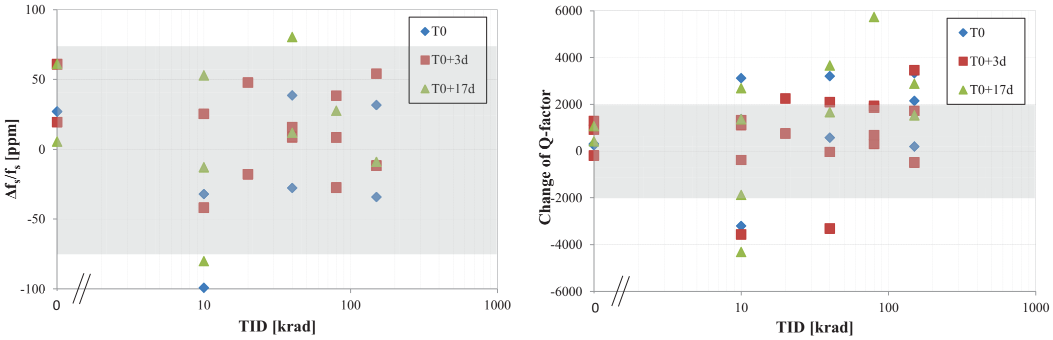

Figure 6.4: Relative change of the anti-resonance frequency (left) and absolute change of the quality factor (right) during the proton irradiation campaign, relative to the pre-irradiation value, which was about 20000. (◊ Directly after the irradiation, □ 3 days after the irradiation, and Δ 17 days after the irradiation).

the in the Q-factors after the proton irradiation tests (Figure 6.4). Further experiments, preferably at higher doses, would be required to assess the repeatability of this observation and clarify the fundamental processes by which radiation damage is induced and accumulated in the system. Nevertheless, these results indicate that the tuning fork resonators are highly resistant to ionizing damage and may perform well under radiation conditions relevant for space applications.

6.2.1 Mechanical tests of tuning fork resonators

Figure 6.5 shows the resonance frequency and quality factor of the tested devices after each test level. Again, the left graph shows the relative change of the resonance frequency and the right graph shows the absolute change of the quality factor, relative to the state before irradiation. Each data point in the graphs corresponds to one resonator, measured after each

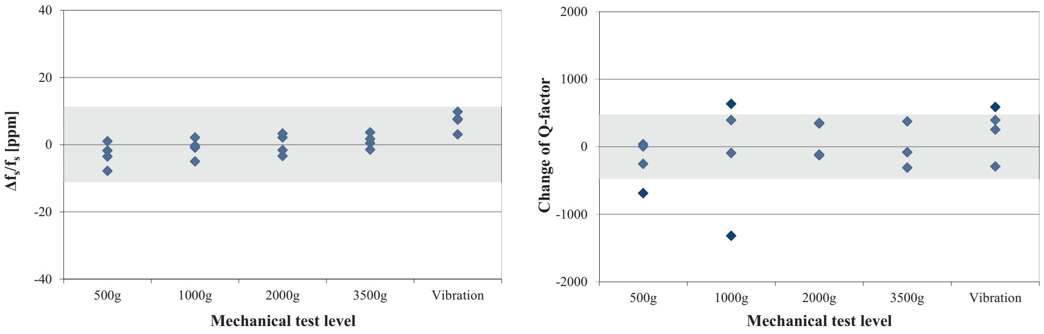

Figure 6.5: Resonance characteristics of the tuning fork resonators after mechanical shock and vibration tests. (Left) Relative change in the serial resonance frequency. (Right) Absolute change of the quality factor.

of the mechanical test levels. The areas shaded in gray limit the values of $\Delta f_{res}/f$ and ΔQ which lie within one standard deviation of the repeatability of the measurement. The results obtained indicate that the mechanical loads have not caused a significant degradation of the devices and that the specimens have remained unaffected by the tests.

6.3 Discussion

The piezoelectrically activated tuning fork resonators fabricated by CSEM present a very good resistance to irradiation both for ionizing radiation and displacement damage effects. The resonance frequencies did not significantly deviate from the pre-irradiation values within the experimental uncertainty, which were ±11 ppm and ±75 ppm for the gamma-ray tests and the proton tests, respectively. This is explained by the fact that the MEMS device is not dependent on electrostatic actuation, where charge trapping by dielectrics can induce serious degradation of the device performance [62]. In the tuning fork devices tested here, a charge trapping could lead to screening of the actuation voltage. However, only small energies are required to actuate the tuning fork in its resonance, and the doses tested did not induce measureable deteriorations of the actuation mechanism. The results also confirmed that the ionizing damage and displacement damage have only little effect on the Young's modulus of the materials, most notably on the silicon, which accounts for the bulk of the tuning fork tines and dominates the mechanical properties of the resonators. The measurement uncertainty was also significantly improved in comparison to the single-material resonators presented in Chapter 3 where the measurement uncertainty was 0.5% (but where on the other hand much higher doses were used). In the Cobalt-60 irradiation campaign the uncertainty was ±10 ppm and in the proton irradiation tests it was ±75 ppm due to the need to use another test instrument, as discussed in section 3.2.

The quality factors of the resonators did not significantly shift either, however the repeatability was not optimal; the measurement uncertainty was about 3% of the absolute Q-factor value for the gamma-ray tests and 12% for the proton tests. It would be of great interest to further study the influence of radiation on the damping in MEMS materials and the underlying mechanisms. Resonators with high quality-factors, and hence minimized intrinsic damping, would be especially suited for this purpose [238].

The mechanical tests of the resonators have shown that the devices are resistant to high levels of mechanical shocks up to 3500 g and vibrations of up to 37 g_{rms}.

6.4 Chapter Summary

In this chapter the effect of space-relevant radiation and mechanical loads on silicon tuning fork resonators driven by piezoelectric AlN has been investigated. It was found that the devices were highly resistant to radiation induced degradations of doses of up to 170 krad(Si)) up to which no degradation was observed within the experimental uncertainty. This indicates that the system as a whole, but also the silicon, which makes up for the majority of the resonator volume, is highly tolerant to radiation damage. In addition, the devices were immune to mechanical shocks of up to 3500 g and vibrations of 37 g_{rms}. This work supports the efforts taken towards design and fabrication of highly reliable MEMS devices and demonstrates that silicon tuning fork resonators may be well suited for space applications.

Chapter 7
Conclusions

The study was set out to explore the analysis of the mechanical properties of MEMS structural materials and their reliability under environmental hazards. Although countless microsystems have been developed in recent years, several vital questions related to the reliability of MEMS systems and MEMS materials remain open to date. Two topics which merit special attention were at the center of this study. Firstly, it is crucial to deepen our understanding of the influence of the packaging on the functioning and the reliability of microsystems. Packaging is of utmost importance to protect the device from its environment and prevent contamination and corrosion. In addition, the integration of the packaging into the fabrication process on the wafer-level can lead to a significant reduction of process time and cost. On the other hand, a miniaturized packaging gives rise to new challenges including the difficulty to measure the leak rate of the package and the proximity of structural elements, which influences the strain distribution in the system and leads to additional air damping by air being squeezed in small gaps. The second area of interest is the reliability of microsystems under the harsh environmental conditions imposed by space applications. MEMS offer huge advantages over macrosystems in space applications, most notably the significant reduction of mass and energy consumption. However, in order to successfully penetrate the space market, the reliability of MEMS needs to be improved and – what is easy to be forgotten, but what ultimately makes the difference – proved. The study sought to answer three questions out of this area of interest:

A) Is high-resolution x-ray diffraction a suitable method for investigating the packaging-related strain in microsystems?

B) How is the elasticity of MEMS structural materials affected by space-relevant radiation doses?

C) Is it possible to analytically describe the pressure dependency of the resonance characteristics of tuning fork resonators which are in close vicinity to the package?

7.1 Synthesis of thesis findings

The main findings were summarized within the respective chapters: Chapter 3 on the design, characterization and structural analysis of piezoelectrically activated silicon tuning fork resonators; Chapter 4 on the air damping in tuning fork resonators, Chapter 5 on the investigation of the elasticity of silicon and SU-8 exposed to proton radiation and Chapter 6 on the reliability of piezoelectrically activated silicon resonators under space-relevant radiation levels and mechanical loads. This section will synthesize the empirical findings to answer the study's three research questions.

A) Is high-resolution x-ray diffraction a suitable method for investigating the packaging-related strain in microsystems?

Packaging-induced stresses and residual stresses from fabrication can pose a serious threat to the long term functioning of microsystems. High-resolution x-ray diffraction allows analyzing the crystal lattice with high precision. This is especially beneficial in the case of single crystals with low defect- and impurity concentrations such as silicon, germanium and sapphire. In such systems, strain levels on the order of 10^{-4} and below can be analyzed routinely using laboratory HRXRD equipment. The stress equilibration between adjacent structures allows using HRXRD as a tool for also measuring the stresses in amorphous layers and layers with lower crystalline quality. In this study, advantage has been taken of the high penetration depth of x-rays to nondestructively investigate the strain in buried structures, namely the strain distribution near the bonding interface of an Au-Sn solder.

As a direct consequence of the deep penetration of x-rays into the material, the measured diffraction pattern is the sum of the diffraction intensity distribution of a relatively large volume of several tens of cubic micrometers. This makes the interpretation of reciprocal space maps difficult. The use of finite element analysis to simulate the strain distribution in the system and the calculation of diffraction patterns based thereon allows comparing the experimental RSM's with models. Simulated reciprocal space maps were used to interpret structural features related to the complex deformation fields and to investigate the influence of individual parameters of the system on the strain distribution and the diffraction pattern. A limitation was that restrictions on the model size and computation resources have limited the accuracy of the FEA model. In addition, the utilized technique to calculate the diffraction pattern does not capture all relevant aspects of diffraction. Nevertheless, the obtained results were in good qualitative agreement with the experiments which underpins the suitability of the approach.

B) How is the elasticity of MEMS structural materials affected by space-relevant radiation doses?

This question was approached in two steps. At first, the susceptibility of single-crystal silicon and SU-8 resonators to proton-radiation induced degradation was investigated in single-material resonators with contactless actuation and readout. Both materials are in widespread use for microsystems structures, and for successful deployment in space applications the stability of the mechanical properties must be ensured over the full device lifecycle. Effects of space-relevant proton doses were examined by monitoring minute changes in the Young's modulus and by structural investigations using x-ray diffraction and FTIR spectroscopy. Single crystal silicon resonators were exposed to 10 MeV and 60 MeV protons with doses up to 10^{13} cm^{-2}, corresponding to 5.9 Mrad. Even at the highest doses neither a change of the Young's modulus was observed nor did x-ray diffraction indicate the formation of elevated concentrations of structural defects. The compatibility of SU-8 with in-orbit radiation environments was investigated at fluences of 10^{10}-10^{12} cm^{-2} using protons with energies ranging from 10 MeV to 200 MeV. Its elastic modulus changed by less than 5.5% at the highest doses.

Going over from the materials level to a complete microsystem, the susceptibility of piezoelectrically activated silicon tuning fork resonators to proton and gamma-irradiation was investigated. A very good radiation tolerance was observed, with no significant degradation at doses of up to 170 krad.

C) Is it possible to analytically describe the pressure dependency of the resonance characteristics of tuning fork resonators which are in close vicinity to the package?

The influence of air damping on the quality-factor and the resonance frequency of tuning forks encapsulated on the wafer level has been analyzed theoretically and experimentally from the free molecular regime to the viscous damping region. The pressure-sensitivity of the resonators was characterized by measurements of the resonance frequency and the quality factor as a function of the air pressure from 10^{-3} mbar to 1 bar. The resonators were found to be highly suited for leak rate measurement down to 10^{-14} mbar l s^{-1}.

In this work two contributions to the understanding of air-damping in microstructures are made: The first is a refinement of the molecular damping model proposed by Bao and coworkers [178]. Molecular dynamics simulations of squeeze-film air damping reported in literature have indicated that Bao's model underestimated the damping. In this study, Bao's model was refined to account for additional parameters such as the variation of the gap width and the velocity variation of the resonator over the oscillation cycle. A significantly improved agreement with experiments was found. A limitation of the methodology is related to the assumption of purely elastic and specular scattering of the gas molecules on the surfaces. Secondly, the 'string of beads' theory commonly used to describe the damping of microresonators in the viscous regime was adapted using a phenomenological correction factor to account for the geometry of the beams. The results of the models were compared to experimental measurements and good agreement was found.

The models presented deepen the understanding of the damping effects in the economically important tuning fork resonators and support the co-design of the resonators and the surrounding package.

7.2 Implications of the findings

Firstly, the measurement of the dynamical properties of single-material microresonators was shown to be a powerful method for the investigation of material properties in structures relevant to microsystems technology. The selected geometries, fabrication processes, and operation modes add to the relevance and allow for a direct transfer of the results presented in this study to other types of MEMS devices. These results indicate that single crystal silicon and SU-8 are very well suited for space applications regarding their radiation tolerance and that the elasticity of the two materials can be considered to remain constant under space-relevant doses for most applications. In addition, it was also found that piezoelectrically activated silicon microresonators using AlN thin films are highly resistant to radiation damage.

Secondly, in spite of the limitations discussed above, it has been shown in this case study that HRXRD is a powerful method providing key information on stresses in microelectromechanical systems and supplements other analysis techniques applied in microtechnology. The possibility to access information on the strain distribution in sub-surface structures at a depth of up to approximately 100 µm, and the nondestructive nature of the technique underpin the practical suitability of HRXRD for quality control during the development, fabrication, packaging and testing of microsystems.

Finally, an improved framework for the analysis of air-damping in microresonators and their packages has been presented. These findings deepen the understanding of air-damping in MEMS and extend the range of tools available for the prediction of the performance of microresonators in the design phase, both related to pressure sensitivity in pressure sensors or hermeticity test structures and on the allowable pressure inside a cavity of other resonant structures.

7.3 Research perspectives

In summary, it is especially noteworthy that the reliability of microsystems is a multifaceted problem. For instance, the radiation tolerance is determined by the individual materials, but also by the interaction between adjacent materials. In addition, packaging provides protection to the device but also gives rise to additional damping, strains and limits the interaction with the environment.

Attaining the goal of exploiting the full potential benefits of HRXRD may be facilitated by exploring the following strategies:

- The strain and rotation components obtained from the finite element analysis could be used as an input to computer programs which account for the dynamical diffraction effects, i.e. based on the Takagi-Taupin equations [235], [236].
- In addition, there is need for more case studies of the measurement of strain in buried structures such as embedded dies and (wafer-level) die packages. The combination of HRXRD with environmental tests such as temperature, pressure and humidity (i.e. accelerated aging) would be of special relevance to investigate the strain distribution and its dependence on the respective environmental parameter *in-situ*.

The single-material resonators with contactless actuation and readout offer great potential for the investigation of the mechanical properties of MEMS materials. In this context it would be especially beneficial to conduct more studies on:

- the variation of the elasticity of other important structural MEMS materials (SiC, III-nitrides and silicon) especially at higher radiation doses such as they are encountered in nuclear fission and fusion reactors,
- the stability of the Poisson's ratio of materials under harsh environmental conditions using torsional resonators, and
- the influence of the oxygen plasma in low Earth orbits on MEMS materials [237], most notably polymers,
- the influence of radiation on the damping in MEMS materials and the study of the underlying mechanisms. Resonators with high quality-factors, and hence minimized intrinsic damping, would be especially suited for this purpose [238].

In addition, it would be of great interest to further investigate the limits of silicon resonators with regards to the frequency stability and the possibility to replace quartz oscillators by silicon also in high-end applications. An evaluation of different silicon-based actuation technologies (thermal, electrostatic or piezoelectric actuation) under space-relevant conditions, most notably thermal stresses and radiation would be of particular benefit in this regard.

In conclusion, it can be stated that the fabrication processes, operation modes, materials and failure modes of microsystems define a vast landscape in which many areas still remain uncharted to date. It is crucial to approach a system from different perspectives to construct a global picture of the systems properties, its weaknesses and its strengths. This thesis attempted to contribute to the mapping of the unexplored areas in this landscape and to support the development of microsystems which reach their full potential.

A. Appendix Nonlinear 3-Point and 4-Point Bending for MEMS Mechanical Strength Investigations and Fabrication Process Qualification

In this appendix the efforts made on the development of an instrumental setup and a theoretical analysis of non-linear 3-point and 4-point bending are presented. The applications targeted were specimens with sub-mm width and thicknesses of 50-500 µm. For instance, microfabricated structures used in mechanical watches or macro-MEMS (3D sensors and actuators made from 2D building blocks fabricated from wafers [239]) can have such small dimensions and experience very high levels of mechanical strain during assembly and operation. In addition, the constant device miniaturization in advanced technologies leads to dies size which are smaller than 1 mm^2 and which are fabricated on ultrathin wafers, for instance in supervisory and RFID circuits.

The essence of this chapter is published T. Bandi, X. Maeder, A. Dommann, H. Shea and A. Neels, *Proc. SPIE*, 2014 pp. 897509 (© 2014 Society of Photo Optical Instrumentation Engineers).

A.1 Bending test geometry and simulation

As mentioned in section 2.2, it is important to reproduce fabrication processes and specimen geometries of real devices as close as possible when evaluating the failure distribution of test specimens such as simple beams. The length of the beams is less crucial because it can be accounted for by analysis of the Weibull failure distribution. The probability of rupture *S* in the 2-paramter Weibull distribution is given by [240]

$$S = 1 - e^{-\int_A k\left(\frac{\sigma}{\sigma_0}\right)^m dA} \tag{A.1}$$

In (A.1) the exponent is integrated over the whole stressed surface. This is justified by the assumption that defects at the surface cause fracture; otherwise the integration may run over the stressed volume. The parameters σ, σ_0, m and k denote the stress at a given position on the surface of the specimen, the characteristic yield strength, the shape parameter of the Weibull distribution and a proportionality factor which equals unity. The parameters σ_0 and *m* are the characteristic parameters of the failure distribution and depend on the material properties and defect distribution. If the sample length is varied this will increase the total loaded area but not change the defect distribution, and hence σ_0 and *m*, because they do not vary along the length of the specimen if the cross-section is constant (as is the case for rectangular cuboid dies).

In [241] the non-linearity of three-point bending and four-point bending was analyzed by a spring model with rigid bodies and by finite element analysis. A reasonable correspondence between the experimental three-point bending and the FEA model was found, but the case of four-point bending has not been experimentally validated. Here the non-linear bending of the specimen was numerically simulated by considering the large deflection of a slender Euler-Bernoulli beam. In the bent beam the outer exposed side is under tensile strain, the inner side is under compression and the neutral centerline is stress-free. The stress increases linearly with the distance from the centerline, and hence thicker specimens are under higher stresses at a given beam curvature than thin specimens. The coordinate system is chosen such that the unconstrained beam is parallel to the *x*-axis and during the test it is deflected in the *y*-direction. In all cases the positions of the pins along the *x*-axis is equidistant. Non-linear four point bending has been investigated previously in [242], [243]. The bending of the beams in the three-point bending is given by the following second order differential equation [244]:

$$\frac{M}{EI} = \frac{1}{EI} F\left(x\left(\cos(\theta) + \mu \sin(\theta)\right) + y\left(\sin(\theta) - \mu \cos(\theta)\right) = \frac{\dfrac{\partial^2 y}{\partial x^2}}{\left(1 + \left(\dfrac{\partial y}{\partial x}\right)^2\right)^{3/2}} \tag{A.2}$$

The parameters *E*, *I*, *F*, *x*, *y*, *θ* and μ are the Young's modulus, second moment of inertia, the force acting on the outer pins normal to the beam, the *x* and *y* coordinate of a point on the beam centerline, the contact angle of the beam with the outer pins and the static friction coefficient between the pins and the beam, respectively. Equation (A.2) was numerical solved using a Runge-Kutta approach similar to the technique proposed in [242] for four-point bending: The integration was made starting from the outer pins towards the center of the beam. It was limited to one half or the beam profile due to the symmetry of the profile. For a given contact angle *θ* an initial guess was made for *F* and then (A.2) was solved step-wise using the Runge-Kutta algorithm [245]. At the apex of the beam profile its gradient needed to vanish. If this condition was not fulfilled, the force *F* was adjusted and the process iterated until convergence was achieved. In the four-point bending a similar expression for the bending moment *M* applies but the two zones between the outer and the inner pins and between the inner pins and the center need to be treated separately [242].

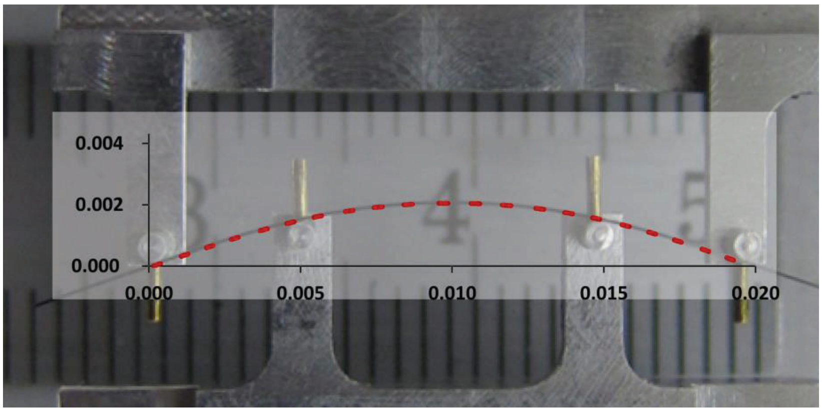

Figure A.1: Superposition of a bent beam and the theoretical beam profile according to equation (A.2). The force sensor is attached to the inner pins while the outer pins are displaced by the stepping motor. The units of the x and y axis is meters.

The size of the pins exerting the bending force on the specimens was non-negligible in comparison to the specimen size and because large bending angles were encountered during the tests, the model was extended to account for the effect of the pins on the profile of the bent beam. This was simply achieved by calculating the contact point on the pins as a function of the contact angle. In Figure A.2 left, the profile of the beam for various deflections in the case of four-point bending is shown. The round points show the position of the pins which enforce the bending of the beam. The right graph in Figure A.2 shows the inverse curvature radius along the bent beam.

The profile and curvature of the beam depend on the static friction coefficient μ between the beam and the pins. Therefore the 3-point and 4-point bending tests also yield information on this parameter. Based on the simulations the experimentally accessible force of the beam on the pins parallel to the y-axis was calculated.

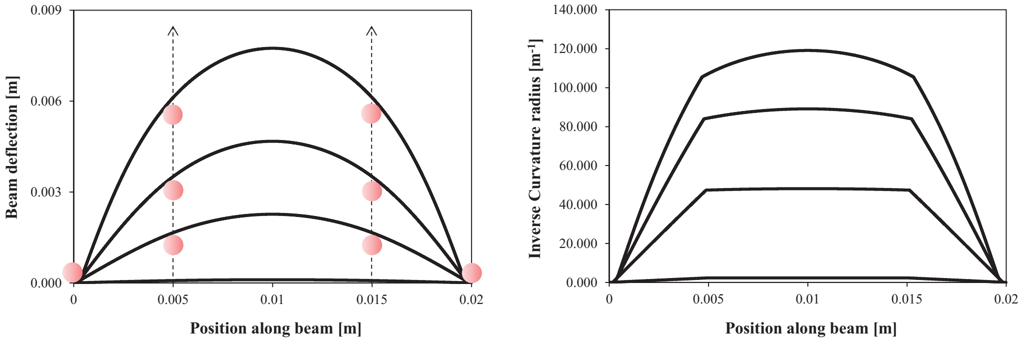

Figure A.2: (Left) Profile of a non-linearly bent Euler-Bernoulli beam for various deflection states. The round dots show the position of the pins. (Right) The inverse curvature radius along the beams. The curvature is inversely proportional to the strain.

Figure A.1 shows a comparison of the profile of a bent beam with the profile obtained by solving the 4-point bending equation equivalent to (A.2) [242]. The calculated bending line (red) was uniformly scaled and superposed over the experimental image and an excellent agreement was found.

A.2 Experimental setup

As mentioned above, the experimental setup was based on the instrument presented in [11], where the instrument is described in detail. The two chucks which enforced the bending of the beam were mounted on a stepping motor and a force sensor, respectively. The motor was moved at a speed of 10 μm/s. The pins were made from aluminum and had a radius of 0.5 mm to avoid sharp contacts. To qualify the experimental setup single-crystal silicon beams fabricated by deep-reactive ion etching with a cross-section of 50x50 μm^2 and 50 mm length were used. The same specimens were used in 2-point bending in [11], so the dimensions, surface state and failure distribution were well characterized. The characteristic yield strength and the shape parameter of the 2-parameter Weibull distribution were 4 GPa and 2.62, respectively. The etched sidewalls were oriented perpendicular to the bending direction (i.e. out of the image plane in Figure A.1).

During the experiment the displacement of the stepping motor was recorded together with the force P acting on the pins normal to the direction of motion of the pins (y-axis in Figure A.2). For comparing the experiments of specimens with different sizes the force was normalized with regards to the distance a between the outer pins, the elasticity of the beams and their second moment of inertia $\alpha = 2Pa^2/EI$.

A.3 Results and discussion

Figure A.3 shows the experimental results obtained in three-point bending (Figure A.3, left) and four-point bending (Figure A.3, right). The maximum strain to which the specimens were exposed in the two tests was around 1 GPa in both tests. Therefore the specimens did not break even at the highest deflections. This allowed measuring the bending parameters of the specimens in the full experimentally accessible range. In the linear-bending regime where the experimental data overlaps with the dotted line (linear theory) the repeatability of the data was best. At higher deflections the variations of the data increased, which was attributed to a stepped slipping motion of the beam along the pins.

The experimental data showed a very good agreement with the model with static fiction coefficients of 0.19 and 0.22 for the four-point bending and the three-point bending, respectively. The small variation between the two values was presumably due to variations of the surface finish of the aluminum pins. For comparison, the theoretical curves for various values of the friction coefficient (dashed lines). The dash-dotted line shows the simulated result

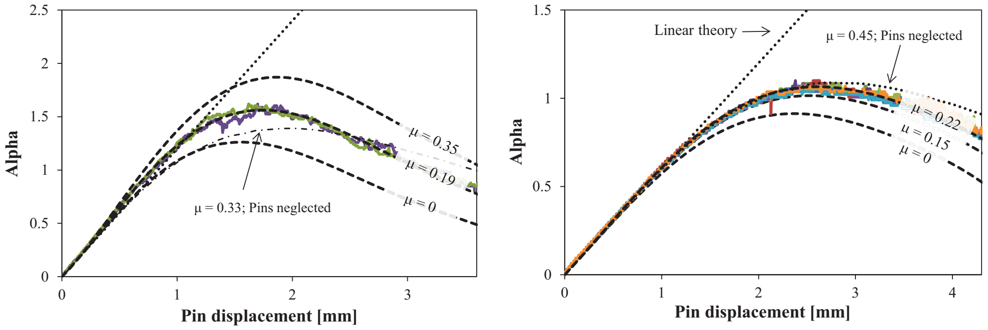

Figure A.3: Force versus pin-displacement for the three-point bending (Left) and four-point bending (right). The distance between the outer pins was 10 mm in both cases. Three measurements with three different samples are shown in both graphs. The dotted line represents the linear theory, the dashed line shows the results of the non-linear bending theory, and the dash-dotted line is the non-linear model without considering the pin geometry.

under neglect of the pins (radius equal to zero). The significant disagreement between this model and the experimental data shows the importance of incorporating the pins in the model.

The results obtained show that the instrumental setup for three-point bending and four-point bending provides valuable insights on the mechanical properties and failure distribution of microfabricated specimens under bending loads. By adapting the size of the chucks different stress ranges can be accessed. To exemplify this, Figure A.4 shows the experimentally accessible stress ranges for a sample with a thickness of 100 µm. By selecting the appropriate test geometry the mechanical stability of specimens with widely varying yield strengths can be evaluated.

A.4 Conclusions

The development progress of a micromechanical test bench for the reliability assessment of microstructures was reported. The instrument induces a displacement-controlled deformation in 4-point, 3-point and 2-point bending. The mechanical test setup allows reproducing the strain conditions and sample properties such as surface-to-volume ratio and loaded-surface-to-edge radio as well as the fabrication processes as close as possible. In addition, tensile testing geometries and custom-made chucks for testing of specific specimen geometries are available [11]. The instrumental test setup allows quantifying the failure distribution in test structures and functional devices with yield strengths in the full range between 0 and 10 GPa. In addition, in-situ testing in combination with high-resolution x-ray diffraction measurements can be used to investigate strain distributions and defects in crystalline specimens [11].

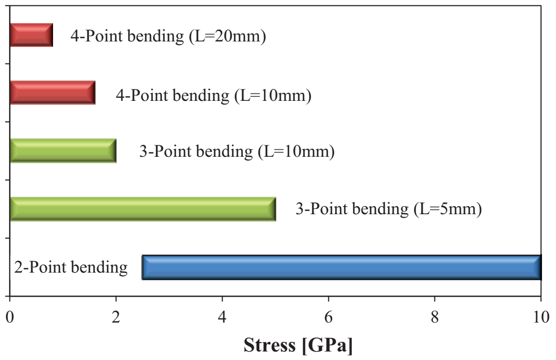

Figure A.4: Comparison of the experimentally accessible stresses in a 100 μm thick specimen. The values of *L* denote the distance between the outer pins.

By quantifying the yield strength distributions these methods allow optimizing fabrication and die separation processes. The safety margins of structure geometries and of dicing lines may be reduced which can lead to significantly higher number of devices per wafer, most importantly for small dies with surfaces of below one square-millimeter. Further results on the qualification of laser processes for chip separation using HRXRD combined with micro-mechanical testing have been obtained in the frame of a CTI project and have been presented elsewhere [154],[155].

Bibliography

[1] A. L. Hartzell, M. G. daSilva and H. R. Shea, *MEMS reliability (MEMS Reference Shelf Series)*. Boston, MA: Springer US, 2011.

[2] V. T. Srikar and S. M. Spearing, "A critical review of microscale mechanical testing methods used in the design of microelectromechanical systems," *Exp. Mech.*, vol. 43, no. 3, pp. 238-247, Sep. 2003.

[3] M. F. Pantano, H. D. Espinosa and L. Pagnotta, "Mechanical characterization of materials at small length scales," *J. Mech. Sci. Technol.*, vol. 26, no. 2, pp. 545-561, Feb. 2012.

[4] W. N. Sharpe, "Mechanical properties of MEMS materials," in *The MEMS Handbook.* Boca Raton, FL: CRC/Taylor & Francis, 2002, ch. 3, pp. 1-33.

[5] M. G. Da Silva and S. Bouwstra, "Critical comparison of metrology techniques for MEMS," in *Proc. SPIE*, 2007, pp. 64630C.

[6] J. T. M. van Beek and R. Puers, "A review of MEMS oscillators for frequency reference and timing applications," *J. Micromech. Microeng.,* vol. 22, no. 1, pp. 013001, Jan. 2012.

[7] F. L. Walls and J. R. Vig, "Fundamental limits on the frequency stabilities of crystal oscillators," *IEEE Trans. Ultrason. Ferroelect. Freq. Contr.*, vol. 42, no. 4, pp. 576-589, Jul. 1995.

[8] J. R. Vig and T. R. Meeker, "The aging of bulk acoustic wave resonators, filters and oscillators," in *Proc. 45th Ann. Symp. on Frequency Control*, Los Angeles, CA, 1991, pp. 77-101.

[9] J. Gomes and H. R. Shea, "Displacement damage effects in silicon MEMS at high proton doses," in *Proc. SPIE*, 2011, pp. 79280G.

[10] H-C. Tsai and W. Fang, "Determining the Poisson's ratio of thin film materials using resonant method," *Sens. Actuators A, Phys.*, vol. 103, no. 3, pp. 377-383, Feb. 2003.

[11] A. Schifferle, "Combined experimental methods for the mechanical characterization of materials," PhD Thesis, ETH Zürich, Switzerland 2011.

[12] A. Böge (edts), *Formeln und Tabellen Maschinenbau*, Wiesbaden, Germany: Vieweg Verlag, 1999, pp. 222-225 (in german).

[13] A. Böge (edts), *Formeln und Tabellen Maschinenbau*, Wiesbaden, Germany: Vieweg Verlag, 1999, pp. 238 (in german).

[14] B. Poon, D. Rittel and G. Ravichandran, "An analysis of nanoindentation in elastoplastic solids," *Int. J. Solids. Struct.*, vol. 45, no. 25-26, pp. 6399–6415, Dec. 2008.

[15] B. Poon, D. Rittel and G. Ravichandran, "An analysis of nanoindentation in linearly elastic solids," *Int. J. Solids. Struct.,* vol. 45, no. 24, pp. 6018–6033, Dec. 2008.

[16] D. J. Shuman, A. L. M. Costa and M. S. Andrade, "Calculating the elastic modulus from nanoindentation and microindentation reload curves," *Mater. Charact.*, vol. 58, no. 4, pp. 380-389, Apr. 2007.

[17] M. S. Gaither, R. S. Gates, R. Kirkpatrick, R. F. Cook and F. W. DelRio, "Etching process effects on surface structure, fracture strength, and reliability of single-crystal silicon theta-like specimens," *J. Microelectromech. Syst.*, vol. 22, no. 3, pp. 589-602, Jun. 2013.

[18] O. M. Jadaan, N. N. Nemeth, J. Bagdahn and W. N. Sharpe, "Probabilistic Weibull behavior and mechanical properties of MEMS brittle materials," *J. Mater. Sci.*, vol. 38, no. 20, pp. 4087 – 4113, Oct. 2003.

[19] T. Namazu, Y. Isono, and T. Tanaka, "Evaluation of size effect on mechanical properties of single crystal silicon by nanoscale bending test using AFM," *J. Microelectromech. Syst.*, vol. 9, no. 4, pp. 450-459, Dec. 2000.

[20] T. Namazu and Y. Isono, "Fatigue life prediction criterion for micro-nanoscale single-crystal silicon structures," *J. Microelectromech. Syst.*, vol. 18, no. 1, pp. 129-137, Feb. 2009.

[21] J. Samuels and S. G. Roberts, "The brittle-ductile transition in silicon: 1. Experiments," *Proc. Royal Soc. A*, vol. 421, no. 1860, pp. 1–23, Jan. 1989.

[22] X. D. Han, K. Zheng, Y. F. Zhang, X. N. Zhang, Z. Zhang and Z. L. Wang, "Low-temperature in situ large-strain plasticity of silicon nanowires," *Adv. Mater.*, vol. 19, no. 16, pp. 2112–2118, Aug. 2007.

[23] F. Östlund, K. Rzepiejewska-Malyska, K. Leifer, L. M. Hale, Y. Y. Tang, R. Ballarini, W. W. Gerberich and J. Michler, "Brittle-to-ductile transition in uniaxial compression of silicon pillars at room temperature," *Adv. Funct. Mater.*, vol. 19, no. 15, pp. 2439–2444, Aug. 2009.

[24] W-S. Lei, A. Kumar and R. Yalamanchili, "Die singulation technologies for advanced packaging: A critical review," *J. Vac. Sci. Technol. B*, vol. 30, no. 4, pp. 040801, 2012.

[25] M. J. Matthewson, and G. J. Nelson, "A novel four-point bend test for strength measurement of optical fibers and thin beams – Part II: Statistical Analysis," *J. Lightwave Technol.*, vol. 14, no. 4, pp. 564-571, Apr. 1996.

[26] V. L. Huy, S. Kamiya, K. Nagayoshi, H. Izumi, J. Gaspar and O. Paul, "A prediction scheme of the static fracture strength of MEMS structures based on the characterization of damage distribution on a processed surface," *J. Micromech. Microeng.*, vol. 23, no. 4, pp. 045008, Apr. 2013.

[27] M. Steiert and J. Wilde, "New probabilistic reliability model describing the risk of chip fracture in chip-on-board technology," in *Proc. 4th Electronic System-Integration Technology Conf. (ESTC)*, Amsterdam, Netherlands, 2012, pp. 1-6.

[28] B. L. Boyce, R. Ballarini and I. Chasiotis, "An argument for proof testing brittle microsystems in high-reliability applications," *J. Micromech. Microeng.*, vol. 18, no. 11, pp. 117001, Nov. 2008.

[29] S-H. Chae, J-H. Zhao, D. R. Edwards and P. S. Ho, "Effect of dicing technique on the fracture strength of Si dies with emphasis on multimodal failure distribution," *IEEE Trans. Device Mat. Rel.*, vol. 10, no. 1, pp. 149-156, Mar. 2010.

[30] M. Ranjan, L. Gopalakrishnan, K. Srihari, and C. Woychik, "Die cracking in flip chip assemblies," in *Proc. 48th IEEE Electronic Components & Technology Conf.*, Seattle, WA, 1998, pp. 729-733.

[31] M-Y. Tsai, C. H. J. Hsu and C. T. O. Wang, "Investigation of thermo-mechanical behaviors of flip chip BGA packages during manufacturing process and thermal cycling," *IEEE Trans. Comp. Packag. Technol.*, vol. 27, no. 3, pp. 568-576, Sep. 2004.

[32] H. Behnken, M. Ape and D. Franke, "Simulation of mechanical stress during bending tests for crystalline wafers," in *Proc. 3rd World Conf. on Photovoltaic Energy Conversion*, Osaka, Japan, 2003, pp. 1308-1311.

[33] J. Brückner, E. Auerswald, R. Dudek, S. Rzepka and B. Michel, "Review of experimental strength testing methods for silicon dies," in *Proc. MicroCar 2013*, Leipzig Germany, 2011, pp.84-86.

[34] B. Yeung and T-Y. T. Lee, "An overview of experimental methodologies and their applications for die strength measurement," *IEEE Trans. Compon. Packag. Technol.*, vol. 26, no. 2, pp. 423-428, Jun. 2003.

[35] M-Y. Tsai and C. S. Lin, "Testing and evaluation of silicon die strength," *IEEE Trans. Electron. Packag. Manufact.*, vol. 30, no. 2, pp. 106-114, Apr. 2007.

[36] *Fracture Toughness of Resin Systems for Base Materials*, IPC-TM-650 Test Methods Manual, 2013.

[37] T. L. Anderson, *Fracture Mechanics – Fundamentals and Applications,* 3rd ed. Boca Raton, FL: CRC/Taylor & Francis, 2005, ch. 7, pp. 348.

[38] H. A. C. Tilmans, J. De Coster, P. Helin, V. Cherman, A. Jourdain, P. De Moor, B. Vandevelde, N. P. Pham, J. Zekry, A. Witvrouw and I. De Wolf, "MEMS packaging and reliability: An undividable couple," *Microelectron. Reliab.*, vol. 52, no. 9-10, pp. 2228-2234, Sep. 2012.

[39] D. M. Tanner, "MEMS reliability: Where are we now?," *Microelectron. Reliab.*, vol. 49, no. 9-11, pp. 937-940, Sep. 2009.

[40] S. H. Choa, "Reliability of MEMS packaging: vacuum maintenance and packaging induced stress," *Microsyst. Technol.*, vol. 11, no. 11, pp. 1187-1196, Oct. 2005.

[41] G. E. Loeb, F. J. R. Richmond, "BION^{TM} implants for therapeutic and functional electrical stimulation," in: Chapin JK, Moxon KA (edts.) *Neural prostheses for restoration of sensory and motor function*. Boca Raton, FL: CRC/Taylor & Francis, 2001.

[42] R. Melamud, M. Hopcroft, C. Jha, B. Kim, S. Chandorkar, R. Candler and T. W. Kenny, "Effects of stress on the temperature coefficient of frequency in double clamped resonators," in *Proc. Transducers*, Seoul, South Corea, 2005, vol. 1, pp. 392-395.

[43] J. Liu, Y. Shi, P. Li, J. Tang, R. Zhao and H. Zhang, "Experimental study on the package of high-g accelerometer," *Sens. Actuators A, Phys.*, vol. 173, no. 1, pp. 1-8, Jan. 2012.

[44] Y. Q. Qu, R. Melamud and T. W. Kenny, "Using encapsulated MEMS resonators to measure evolution in thin film stress," in *Proc. Transducers*, Denver, CO, 2009, pp. 1138-1141.

[45] W-T. Hsu and C. T-C. Nguyen, "Geometric stress compensation for enhanced thermal stability in micromechanical resonators," in *Proc. IEEE Trans. Ultrason. Symp.*, Sendai, Japan, 1998, vol. 1, pp. 945-948.

[46] Z. Hou, X. Wu, D. Xiao, Z. Chen and J. Su, "Structural improvement in resonant silicon sensors to sub-ppm/°C temperature coefficient of resonance frequency," *J. Micro/Nanolith. MEMS MOEMS*, vol. 13, no. 1, pp. 013016, Mar. 2014.

[47] M. Gonzalez, A. Jourdain, B. Vandevelde and H. A. C. Tilmans, "Effect of thermo-mechanical stress on resonant frequency shift of a silicon MEMS resonator," in *Proc. Int. Conf. on Thermal, Mechanical and Multi-Physics Simulation and Experiments in Microelectronics and Micro-Systems (EuroSimE)*, Freiburg im Breisgau, Germany, 2008, pp. 1-5.

[48] P. Li, S. Gao, H. Liu, J. Liu and Y. Shi, "Effects of package on the performance of MEMS piezoresistive accelerometers," *Microsyst. Technol.*, vol. 19, no. 8, pp. 1137-1144, Aug. 2013.

[49] M. Stoica, J. Das, J. Bednarcik, H. Franz, N. Mattern, W. H. Wang, and J. Eckert, "Strain distribution in $Zr_{64.13}Cu_{15.75}Ni_{10.12}Al_{10}$ bulk metallic glass investigated by in situ tensile tests under synchrotron radiation," *J. Appl. Phys.*, vol. 104, no. 1, pp. 013522, 2008.

[50] A. Schifferle, A. Neels, O. Papes, A. Dommann and E. Mazza, "Combined testing for MEMS characterization," *Procedia Engineering*, vol. 5, pp. 878-881, Jan. 2010.

[51] A. Neels, A. Dommann, A. Schifferle, O. Papes and E. Mazza, "Reliability and failure in single crystal silicon MEMS devices," *Microelectron. Reliab.*, vol. 48, no. 8-9, pp. 1245-1247, Aug. 2008.

[52] I. De Wolf, "Micro-Raman spectroscopy to study local mechanical stress in silicon integrated circuits," *Semicond. Sci. Technol.,* vol. 11, no. 2, pp. 139-154, Feb. 1996.

[53] D. J. Dingley, A. J. Wilkinson, G. Meaden and P. S. Karamched, "Elastic strain tensor measurement using electron backscatter diffraction in the SEM," *J. Electron. Microsc.*, vol. 59(Supplement), pp. 155–163, Aug. 2010.

[54] M. Krause, A. Graff and F. Altmann, "Strain determination using electron backscatter diffraction," *AIP Conf. Proc.,* vol. 1300, pp. 139-144, 2010.

[55] V. Holý, U. Pietsch and T. Baumbach, *High-resolution x-ray scattering from thin films and multilayers*. Berlin and Heidelberg, D: Springer Verlag, 1999, ch. 5.

[56] A. Dommann and A. Neels, "X-Ray strain measurements in strained silicon devices," *AIP Conf. Proc.*, vol. 1378, pp. 131-137, 2011.

[57] A. Dommann and A. Neels, "Quality control on strained silicon devices," *AIP Conf. Proc.*, vol. 1300, pp. 109-113, 2010.

[58] A. Dommann and A. Neels, "Reliability of MEMS," in *Proc. SPIE*, 2011, pp. 79280B.

[59] A. Neels, G. Bourban, H. R. Shea, A. Schifferle, E. Mazza and A. Dommann, "Aging of MEMS – Correlation of mechanical and structural properties," *Procedia Chemistry*, vol. 1, no. 1, pp. 820-823, Sep. 2009.

[60] C. S. Wong, N. S. Bennett, D. Manessis, A. Danilewsky, P. J. McNally, "Non-destructive laboratory-based x-ray diffraction mapping of warpage in Si die embedded in IC packages," *Microelectron. Eng.*, vol. 117, pp. 48-56, Apr. 2014.

[61] P. Atkins and J. De Paula, *Physical Chemistry,* 8th ed. New York: W. H. Freeman and Company, 2006, ch. 13, pp. 432.

[62] H. R. Shea, "Radiation sensitivity of microelectromechanical system devices," *J. Micro/Nanolith. MEMS MOEMS*, vol. 8, no. 3, pp. 031303, Jul. 2009.

[63] S. S. McClure, L. D. Edmonds, R. Mihailovich, A. H. Johnston, P. Alonzo, J. DeNatale, J. Lehman, and C. Yui, "Radiation effects in micro-electromechanical systems (MEMS): RF Relays," *IEEE Trans. Nucl. Sci.*, vol. 49, no. 6, pp. 3197-3202, Dec. 2002.

[64] K. O'Brien, "Spacecraft shielding for a Mars mission," *Adv. Space Res.,* vol. 36, no. 9, pp. 1731-1736, Jan. 2005.

[65] E. G. Stassinopoulos and J. P. Raymond, "The space radiation environment for electronics," *Proc. IEEE,* vol. 76, no. 11, pp. 1423-1442, Nov. 1988.

[66] J. R. Schwank, M. R. Schaneyfelt, P. Paillet, D. E. Beutler, V. Ferlet-Cavrois, B. L. Draper, R. A. Loemker, P. E. Dodd and F. W. Sexton, "Optimum laboratory radiation source for hardness assurance testing," *IEEE Trans. Nucl. Sci.,* vol. 48, no. 6, pp. 2152-2157, Dec. 2001.

[67] J. R. Schwank, M. R. Shaneyfelt and P. E. Dodd, "Radiation hardness assurance testing of microelectronic devices and integrated circuits: Radiation environments, physical mechanisms, and foundations for hardness assurance," *IEEE Trans. Nucl. Sci.*, vol. 60, no. 3, pp. 2074-2100, Jun. 2013.

[68] R. A. Mewaldt, "Galactic cosmic ray composition and energy spectra," *Adv. Space. Res.,* vol. 14, no. 10, pp. 737-747, Oct. 1994.

[69] J. F. Ziegler and J. M. Manoyan, "The stopping of ions in compounds," *Nucl. Instrum. Methods Phys. Res. B, Beam Interact. Mater. At.,* vol. 35, no. 3/4, pp. 215-228, Dec. 1988.

[70] G. P. Summers, E. A. Burke, P. Shapiro and S. R. Scott, "Damage correlations in semiconductors exposed to gamma, electron, and proton radiation," *IEEE Trans. Nucl. Sci.,* vol. 40, pp. 1372-1379, 1993.

[71] A. Akkerman, J. Barak, M. B. Chadwick, J. Lewinson, M. Murat and Y. Lifshitz, "Updated NIEL calculations for estimating the damage induced by particles and gamma-rays in Si and GaAs," *Radiat. Phys. Chem.,* vol. 62, no. 4, pp. 301-310, Oct. 2001.

[72] T. R. Oldham, "Analysis of damage in MOS devices for several radiation environments," *IEEE Trans. Nucl. Sci.,* vol. 31, no. 6, pp. 1236–1241, Dec. 1984.

[73] M. J. Berger, J. S. Coursey, M. A. Zucker and J.Chang, *ESTAR, PSTAR, and ASTAR: Computer programs for calculating stopping-power and range tables for electrons, protons, and helium ions (version 1.2.3)*, [Online]. Available: http://physics.nist.gov/Star (Accessed on 27. Feb. 2011), National Institute of Standards and Technology, Gaithersburg, MD, 2005.

[74] *Standard guide for use of an X-ray tester (10 keV photons) in ionizing radiation effects testing of semiconductor devices and microcircuits*, ASTM International Standard F1467 - 11, 2012.

[75] P. Paillet, J. R. Schwank, M. R. Schaneyfelt, V. Ferlet-Cavrois, R. L. Jones, O. Flament and E. W. Blackmore, "Total dose hardness assurance testing using laboratory radiation sources," *IEEE Trans. Nucl. Sci.,* vol. 50, no. 6, pp. 2310-2315, Dec. 2003.

[76] *Total dose steady-state irradiation test method*, ESCC Basic Specification No. 22900, Issue 3, 2007, [Online]. Available: https://escies.org (Accessed on 16. Feb. 2012).

[77] H. Spieler, "Introduction to radiation-resistant semiconductor devices and circuits," *AIP Conf. Proc.,* vol. 390, pp. 23-49, 1997.

[78] C. Cibiel, P. Canzian, V. Candelier and J. Lamboley, "Ultra-stable oscillators dedicated to Low-Earth-Orbit Applications: Behavior vs radiation," in *Proc. IEEE Int. Frequency Control Symp.*, 2007, pp. 1164–1169.

[79] J. J. Martin, "Radiation-induced frequency offsets and acoustic loss in AT-cut quartz crystals," *J. Appl. Phys.,* vol. 68, no. 10, pp. 5095-5104, 1990.

[80] G. L. Weaver, M. J. Reinhart, H. B. Sequeira and W. Stapor, "Examination of detailed frequency behavior of quartz resonators under low dose exposures to proton radiation," in *Proc. 2004 IEEE Int. Frequency Control Symp. and Expo.*, pp. 79-93.

[81] D. L. Griscom, "Point defects and radiation damage processes in α-quartz," in *Proc. 33rd Annu. Symp. on Frequency Control.*, Atlantic City, NJ, 1979, pp. 98-109.

[82] J. J. Martin, "Electrodiffusion (sweeping) of ions in quartz – A review," *IEEE Trans. Ultrason. Ferroelect. Freq. Contr.,* vol. 35, no. 3, pp. 288-296, May 1988.

[83] L. Wang, J. Tang, and Q-A. Huang, "Gamma irradiation effects on surface-micromachined polysilicon resonators," *J. Microelectromech. Syst.*, vol. 20, no. 5, pp. 1071-1073, Oct. 2011.

[84] L. Wang, J. Tang, and Q-A. Huang, "Gamma and electron beam irradiation effects on the resistance of micromachined polycrystalline silicon beams," *Sens. Actuators A, Phys.*, vol. 177, pp. 99-104, Apr. 2012.

[85] P. Gkotsis, V. Kilchytska, C. Fragkiadakis, P. B. Kirby, J-P. Raskin and L. A. Francis, "Effects of fast neutrons on the electromechanical properties of materials used in microsystems," *J. Microelectromech. Syst.*, vol. 21, no. 6, pp. 1471-1483, Dec. 2012.

[86] L. A. Francis, P. Gkotsis, V. Kilchytska, X. Tang, S. Druart, J-P. Raskin and D. Flandre, "Impact of radiations on the electromechanical properties of materials and on the piezoresistive and capacitive transduction mechanisms used in microsystems," in *Proc. SPIE*, 2013, pp. 86140J.

[87] D. G. Gilmore (edts), *Satellite Thermal Control Handbook Volume I: Fundamental Technologies*, E1 Segundo, CA: The Aerospace Corporation Press, 1994, ch. 2.

[88] A. L. Hartzell, M. G. da Silva and H. R. Shea, *MEMS reliability (MEMS Reference Shelf Series).* Boston, MA: Springer US, 2011, ch. 2.

[89] *Space Engineering – Testing*, European Cooperation for Space Standardization (ECSS) Standard ECSS-E-10-03A, Feb. 2002.

[90] M. Bloch, O. Mancini and T. McClelland, "What we don't know about quartz clocks in space," in *Proc. 41th Annu. Precise Time and Time Interval Meeting*, Santa Ana Pueblo, NM, 2009, pp. 457-472.

[91] J. A. Kusters and J. R. Vig, "Hysteresis in quartz resonators-A review," *IEEE Trans. Ultrason. Ferroelect. Freq. Contr.*, vol. 38, no. 3, pp. 281-290, May 1991.

[92] R. C. Turner, P. A. Fuierer, R. E. Newnham and T. R. Shrout, "Materials for high temperature acoustic and vibration sensors: A review," *Appl. Acoust.*, vol. 41, pp. 299-324, 1994.

[93] C. Bourgeois, E. Steinsland, N. Blanc and de N. F. Rooij, "Design of resonators for the determination of the temperature coefficients of elastic constants of monocrystalline silicon," in *Proc. 1997 IEEE Int. Frequency Control Symp.*, Orlando, FL, pp. 791–799.

[94] J. C. Salvia, R. Melamud, S. A. Chandorkar, S. F. Lord and T. W. Kenny, "Real-time temperature compensation of MEMS oscillators using an integrated micro-oven and a phase-locked loop," *J. Microelectromech. Syst.,* vol. 19, no. 1, pp. 192-201, Feb. 2010.

[95] H. Lee, A. Partridge and F. Assaderaghi, "Low jitter and temperature stable MEMS oscillator," in *Proc. 2012 IEEE Int. Frequency Control Symp.*, Baltimore, MD, pp. 1–5.

[96] J. Vig and Y. Kim, "The low-power potential of oven-controlled MEMS oscillators," *IEEE Trans. Ultrason. Ferroelect. Freq. Contr.,* vol. 60, no. 4, pp. 851-853, Apr. 2013.

[97] A. Hajjam, A. Logan and S. Pourkamali, "Doping-induced temperature compensation of thermally actuated high-frequency silicon micromechanical resonators," *J. Microelectromech. Syst.,* vol. 21, no. 3, pp. 681-687, Jun. 2012.

[98] A. Jaakkola, M. Prunnila, T. Pensala, J. Dekker and P. Pekko, "Experimental determination of the temperature dependency of the elastic constants of degenerately doped silicon," *Joint European Frequency and Time Forum & Int. Frequency Control Symp. (EFTF/IFC),* pp. 421-424, Jul. 2013.

[99] M. Rais-Zadeh, V. A. Thakar, Z. Wu and A. Peczalski, "Temperature compensated silicon resonators for space applications," in *Proc. SPIE,* 2013, pp. 86140E.

[100] B. Kim, R. N. Candler, M. A. Hopcroft, M. Agarwal, W-T. Park and T. W. Kenny, "Frequency stability of wafer-scale film encapsulated silicon based MEMS resonators," *Sens. Actuators A, Phys.,* vol. 136, no. 1, pp. 125-131, May 2007.

[101] M. Lutz, A. Partridge, P. Gupta, N. Buchan, E. Klaassen, J. McDonald and K. Petersen, "MEMS oscillators for high volume commercial applications," in *Proc. Transducers*, Lyon, France, 2007, pp. 49–52.

[102] E. J. Ng, H. K. Lee, C. H. Ahn, R. Melamud and T. W. Kenny, "Stability of silicon microelectromechanical systems resonant thermometers," *IEEE Sensors J.,* vol. 13, no. 3, pp. 987-993, Mar. 2013.

[103] K. M. Lakin, K. T. McCarron, J. F. McDonald and J. Belsick, "Temperature coefficient and ageing of BAW composite materials," in *Proc. 2001 IEEE Int. Frequency Control Symp.,* Seattle, WA, pp. 605-608.

[104] D. M. Tanner, R. H. Olsson, T. B. Parson and S. M. Crouch, "Stability experiments on MEMS aluminum nitride RF resonators," in *Proc. SPIE*, 2010, pp. 759209.

[105] C. Gorecki, K. Krupa, R. Jozwicki and M. Jozwik, "Reliability study of AlN-driven microcantilevers based on interferometric measurements of their static and dynamic behaviours," in *Proc. SPIE*, 2010, pp.779104.

[106] K. Krupa, C. Gorecki, R. Jozwicki, M. Jozwik and A. Andrei, "Interferometric study of reliability of microcantilevers driven by AlN sandwiched between two metal layers," *Sens. Actuators A, Phys.,* vol. 171, no. 2, pp. 306-316, Nov. 2011.

[107] R. Tabrizian, G. Casinovi and F. Ayazi, "Temperature-stable silicon oxide (SilOx) micromechanical resonators," *IEEE Trans. Electron Devices,* vol. 60, no. 8, pp. 2656-2663, Aug. 2013.

[108] Ariane 5 User's manual, Issue 5 Revision 1, Jul 2011. [Online]. Available: http://www.arianespace.com/launch-services-ariane5/Ariane5_users_manual_Issue5_July2011.pdf (Accessed on 27. Feb. 2014).

[109] A. L. Hartzell, M. G. da Silva and H. R. Shea, *MEMS reliability (MEMS Reference Shelf Series).* Boston, MA: Springer US, 2011, ch. 4, sec. 4.2.2.

[110] V. T. Srikar and S. D. Senturia, "The reliability of microelectromechanical systems (MEMS) in shock environments," *J. Microelectromech. Syst.*, vol. 11, no. 3, pp. 206-214, Jun. 2002.

[111] S. Sundaram, M. Tormen, B. Timotijevic, R. Lockhart, T. Overstolz, R. P. Stanley and H. R. Shea, "Vibration and shock reliability of MEMS: modeling and experimental validation," *J. Micromech. Microeng.*, vol. 21, no. 4, pp. 045022, Apr. 2011.

[112] R. K. Traeger, "Nonhermeticity of polymeric lid sealants," *IEEE Trans. Parts, Hybrids, Packag.*, vol. 13, no. 2, pp. 147-152, Jun. 1977.

[113] G. Jiang and D. D. Zhou, "Technology advances and challenges in hermetic packaging for implantable medical devices," in *Implantable Neural Prostheses 2, Biological and Medical Physics, Biomedical Engineering,* New York: Springer, 2010, pp. 27-61.

[114] M. Schuettler, J. S. Ordonez, T. S. Santisteban, A. Schatz, J. Wilde and T. Stieglitz, "Fabrication and test of a hermetic miniature implant package with 360 electrical feed-throughs," in *Proc. 32nd Annu. Int. Conf. IEEE Engineering in Medicine and Biology Society (EMBC)*, Buenos Aires, Argentina, 2010, pp. 1585-1588.

[115] S. Costello, M. P. Y. Desmulliez and S. McCracken, "Review of test methods used for the measurement of hermeticity in packages containing small cavities," *IEEE Trans. Compon. Packag. Manufact. Technol.*, vol. 2, no. 3, pp. 430-438, Mar. 2012.

[116] P-L. Charvet, P. Nicolas, D. Bloch and B. Savornin, "MEMS packaging reliability assessment: Last development in the field of residual gas analysis tests," in *Proc. 2013 European Microelectronics Packaging Conf. (EMPC)*, Grenoble, France, pp. 1-5.

[117] D. Lellouchi, J. Dhennin, X. Lafontan, D. Veyrie, J-F. Le Neal and F. Pressecq, "A new method for the hermeticity testing of wafer-level packaging," *J. Micromech. Microeng.,* vol. 20, no. 2, pp. 025031, Feb. 2010.

[118] F. Gueissaz and J-P. Randin, "Method of checking the hermeticity of a closed cavity of a micrometric component and micrometric component for the implementation of the same," U.S. Patent 7833484, Nov. 16, 2010.

[119] F. Gueissaz, "Ultralow leak detection method for MEMS devices," in *Proc. 18th IEEE Conf. Micro Electro Mechanical Systems (MEMS)*, 2005, pp. 524–527.

[120] J. Frömel, D. Billep, T. Gessner, M. Wiedmer, "Application of micromechanical resonant structures for measuring the sealing of bonded sensor systems," *Microsyst. Technol.*, vol. 12, no. 5, pp. 481-483, Apr. 2006.

[121] A. Faes, G. Resta, F. Solazzi and B. Margesin, "Modeling of gold microbeams as strain and pressure sensors for characterizing MEMS packages," *Microsyst. Technol.*, vol. 18, no. 7-8, pp. 1139-1145, Aug. 2012.

[122] H. Okada, T. Itoh and T. Suga, "Wafer level sealing characterization method using Si micro cantilevers," *Sens. Actuators A, Phys.*, vol. 147, no. 2, pp. 359-364, Oct. 2008.

[123] M. Bao and H. Yang, "Squeeze film air damping in MEMS," *Sens. Actuators A, Phys.*, vol. 136, no. 1, pp. 3-27, May 2007.

[124] J. P. Bibring et al., "The Rosetta Lander ('Philae') investigations," *Space Sci. Rev.,* vol. 128, no. 1-4, pp. 205-220, May 2007.

[125] NASA Solar System Exploration: Planets [Online]. Available: http://solarsystem.nasa.gov/planets/index.cfm (Accessed on 26. May 2014).

[126] O. Colpen and H. E. Gruen, "Tuning fork precision oscillators," in *Proc. 13th Annu. Symp. on Frequency Control*, 1959, pp.165-181.

[127] C-E. Guillaume, "Nobel lecture - Invar and Elinvar," Nobel Media AB (2013), [Online]. Available: http://www.nobelprize.org/nobel_prizes/physics/laureates/1920/guillaume-lecture.html (Accessed on 14. Nov. 2013).

[128] D. Ruffieux N. Scolari, F. Giroud, T-C. Le, S. Dalla Piazza, F. Staub, K. Zoschke, C-A. Manier, H. Oppermann, T. Suni, J. Dekker, and G. Allegato, "A versatile timing microsystem based on wafer-level packaged XTAL/BAW resonators with sub-μW RTC mode and programmable HF clocks," *IEEE J. Solid-State Circuits*, vol. 49, no. 1, pp. 212-222, Jan. 2014.

[129] D. Ruffieux, F. Krummenacher, A. Pezous and G. Spinola-Durante, "Silicon resonator based 3.2 μW real time clock with ±10 ppm frequency accuracy," *IEEE J. Solid-State Circuits*, vol. 45, no. 1, pp. 224-234, Jan. 2010.

[130] J. Baborowski, C. Bourgeois, A. Pezous, C. Muller, M-A. Dubois, "Piezoelectrically activated silicon resonators," in *Proc. IEEE Int. Frequency Control Symp., Joint with the 21st European Frequency and Time Forum*, Geneva, Switzerland, May 2007, pp.1210-1213.

[131] J-M. Friedt, E. Carry, "Introduction to the quartz tuning fork," *Am. J. Phys.,* vol. 75, no. 5, pp. 415-422, 2007.

[132] C. Muller, J. Baborowski, A. Pezous, M-A. Dubois, "Experimental evidence of thermoelastic damping in silicon tuning fork," *Procedia Chemistry,* vol. 1, no. 1, pp. 1395-1398, Sep. 2009.

[133] J. Baborowski, A. Pezous, G. Spinola Durante, R. Jose James, R. Ziltener, C. Muller, M-A. Dubois, "Wafer level packaging technology for silicon resonators," *Procedia Chemistry,* vol. 1, no. 1, pp. 1535-1538, Sep. 2009.

[134] G. Spinola Durante, R. Jose James, C. Bosshard, C. Muller, J. Baborowski, A. Pezous, F. Cardot, M-A. Dubois, A. Neels, A. Dommann, "Reliable hermetic MEMS chip-scale packaging," in *Proc. 2011 European Microelectronics Packaging Conf. (EMPC)*, Brighton, UK, pp. 1-6.

[135] F. Engelmark, G. F. Iriarte, I. V. Katardjiev, M. Ottosson, P. Muralt, and S. Berg, "Structural and electroacoustic studies of AlN thin films during low temperature radio frequency sputter deposition," *J. Vac. Sci. Technol. A*, vol. 19, no. 5, pp. 2664-2669, Sep./Oct. 2001.

[136] P. Boch, J. C. Glandus, J. Jarrige, J. P. Lecompte and J. Mexmain, "Sintering, oxidation and mechanical properties of hot pressed aluminium nitride," *Ceram. Int.*, vol. 8, no. 1, pp. 34-40, Jan.-Feb. 1982.

[137] H. Iwanaga, A. Kunishige and S. Takeuchi, "Anisotropic thermal expansion in wurtzite-type crystals," *J. Mater. Sci.*, vol. 35, no. 24, pp. 2451-2454, 2000.

[138] J. H. Hubbell, and S. M. Seltzer, *Tables of X-Ray Mass Attenuation Coefficients and Mass Energy-Absorption Coefficients (version 1.4)*, [Online] Available: http://physics.nist.gov/xaamdi (Accessed on 06.05.2011), National Institute of Standards and Technology, Gaithersburg, MD, 2004.

[139] M. A. Hopcroft, W. D. Nix and T. W. Kenny, "What is the Young's modulus of silicon?," *J. Microelectromech. Syst.*, vol. 19, no. 2, pp. 229-238, Apr. 2010.

[140] K. E. Petersen, "Dynamic micromechanics on silicon: Techniques and devices," *IEEE Trans. Electron Devices*, vol. ED-25, no. 10, pp. 1241-1250, Oct. 1978.

[141] J. Mäkinen, " Thick-film SOI wafers: Preparation and properties," in *Handbook of Silicon Based MEMS Materials and Technologies.* Oxford, UK: William Andrew, 2010, ch. 7, pp. 125.

[142] F. G. Yost, M. M. Karnowsky, W. D. Drotning and J. H. Gieske, "Thermal expansion and elastic properties of high gold-tin alloys," *Metall. Trans. A*, vol. 21A, no. 7, pp. 1885-1889, Jul. 1990.

[143] F. Martin, P. Muralt and M-A. Dubois, "Process optimization for the sputter deposition of molybdenum thin films as electrode for AlN thin films," *J. Vac. Sci. Technol. A*, vol. 24, no. 4, pp. 946-952, Jul./Aug. 2006.

[144] W. Paszkowicz, S. Podsiado and R. Minikayev, "Rietveld-refinement study of aluminium and gallium nitrides," *J. Alloys Compounds,* vol. 382, no. 1-2, pp. 100-106, Nov. 2004.

[145] M. A. Moram and M. E. Vickers, "X-ray diffraction of III-nitrides," *Rep. Prog. Phys.*, vol. 72, no. 3, pp. 036502, Mar. 2009.

[146] C. Muller, F. Cardot, T. Bandi and A. Neels, "Wafer level encapsulation of micro-systems (WALES): Piezoelectric resonator WLP prototyping and screening," CSEM SA., Neuchatel, CH, Rep. T.N. 3.1.2, 2012.

[147] T. Bandi and A. Neels, "Wafer level encapsulation of micro-systems (WALES): piezoelectric resonator MEMS WLP testing," CSEM SA., Neuchatel, CH, Rep. T.N. 3.2.2, 2012.

[148] J. R. Patel and N. Kato, "X-ray diffraction topographs of silicon crystals with superposed oxide film. II. Pendellösung fringes: comparison of experiment with theory," J. Appl. Phys., vol. 44, no. 3, pp. 971-977, 1973.

[149] B. Olbrechts, B. Rue1, T. Pardoen, D. Flandre1 and J-P. Raskin, "Routes Towards Novel Active Pressure Sensors in SOI Technology," Adv. Mat. Res., vol. 276, pp. 145-155, Jul. 2011.

[150] W. Kröninger and F. Mariani, "Thinning and singulation of silicon: root causes of the damage in thin chips," in *Proc. 56th Electronic Components and Technology Conf.*, San Diego, CA, 2006, pp. 1317-1322.

[151] Y. Yang, K. De Munck, R. C. Teixeira, B. Swinnen, B. Verlinden and I. De Wolf, " Process induced sub-surface damage in mechanically ground silicon wafers," *Semicond. Sci. Technol.*, vol. 23, no. 7, pp. 075038, Jul. 2008.

[152] M. Radet, P. Jaffrennou, N. Habka, J. Penaud and B. Lombardet, "Analysis of saw damage in monocrystalline slurry sawn Si wafers using Raman spectroscopy," in *Proc. 38th IEEE Photovoltaic Specialists Conference (PVSC)*, Austin, TX, 2012, pp. 002723-002727.

[153] Y. Gogotsi, C. Baek and F. Kirscht, "Raman microspectroscopy study of processing-induced phase transformations and residual stress in silicon," *Semicond. Sci. Technol.*, vol. 14, no. 10, pp. 936–944, Oct. 1999.

[154] X. Maeder, T. Bandi, A. Neels, A. Dommann, Y. Dupraz and M-C. Pasquier, "Qualification of laser processes for chip separation using HRXRD and micromechanical testing," presented at the Swiss Nanoconvention 2013, Basel, [Poster].

[155] X. Maeder, T. Bandi, A. Neels, Y. Dupraz, M.-C. Pasquier, A. Dommann, "Qualification of laser processes for chip separation using HRXRD and micromechanical testing," CSEM Scientific and Technical report (2013), [Online], Available: http://www.csem.ch/ar2013/pdf/CSEM-STR-2013-11.pdf (Accessed on 09. Sep. 2014).

[156] Q. Shen, "Dynamical diffraction," in *Methods in Materials Research*, New York: John Wiley & Sons, 1999.

[157] C. R. Wie, "High resolution X-ray diffraction characterization of semiconductor structures," *Mater. Sci. Eng.*, vol. R13, no. 1, pp. 1-56, Sep. 1994.

[158] W. E. Newell, "Miniaturization of tuning forks," *Science,* vol. 161, no. 3848, pp. 1320-1326, Sep. 1968.

[159] M. Christen, "Air and gas damping of quartz tuning forks," *Sensors and Actuators*, vol. 4, pp. 555-564, Jan. 1983.

[160] D. Zeisel, H. Menzi and L. Ullrich, "A precise and robust quartz sensor based on tuning fork technology for (SF_6)-gas density control," *Sens. Actuators A, Phys.*, vol. 80, no. 3, pp. 233-236, Mar. 2000.

[161] F. J. Giessibl, "High-speed force sensor for force microscopy and profilometry utilizing a quartz tuning fork," *Appl. Phys. Lett.*, vol. 73, no. 26, pp. 3956-3958, Dec. 1998.

[162] L. D. Landau and E. M. Lifshitz, *Fluid Mechanics,* 2nd ed. Oxford UK: Pergamon Press, 1987, pp. 87-92.

[163] L. D. Landau and E. M. Lifshitz, *Theory of Elasticity,* 2nd ed. Oxford UK: Pergamon Press, 1970, pp. 115.

[164] F. R. Blom, S. Bouwstra, M. Elwenspoek and J. H. J. Fluitman, "Dependence of the quality factor of micromachined silicon beam resonators on pressure and geometry," *J. Vac. Sci. Technol. B, Microelectron.*, vol. 10, no. 19, pp. 19-26, Jan./Feb. 1992.

[165] H. Hosaka, K. Itao and K. Susumu, "Damping characteristics of beam-shaped micro-oscillators," *Sens. Actuators A, Phys.*, vol. 49, no. 1/2, pp. 87-95, 1995.

[166] W-M. Zhang, G. Meng and X. Wei, "A review on slip models for gas microflows," *Microfluid. Nanofluid.*, vol. 13, no. 6, pp. 845-882, Dec. 2012.

[167] P. Atkins and J. De Paula, *Physical Chemistry,* 8th ed. New York: W. H. Freeman and Company, 2006, ch. 21, pp. 752-756.

[168] K. Y. Yasumura, K. D. Stowe, E. M. Chow, T. Pfafman, T. W. Kenny, B. C. Stipe and D. Rugar, "Quality factors in micron- and submicron-thick cantilevers," *J. Microelectromech. Syst.*, vol. 9, no. 1, pp. 117-125, Mar. 2000.

[169] Y. Nishimori, S. Ueki, K. Miwa, T. Kubota, M. Sugiyama, S. Samukawa and G. Hashiguchi, "Effect of neutral beam etching on mechanical property of microcantilevers," *J. Vac. Sci. Technol. B*, vol. 31, no. 2, pp. 022001, 2013.

[170] L-W. Hung and C. T-C. Nguyen, "Q-boosted AlN array-composite resonator with Q > 10 000," in *Proc. IEEE Int. Electron Devices Meeting (IEDM)*, San Francisco, CA, 2010, pp. 7.3.1–4.

[171] L-W. Hung and C. T-C. Nguyen, "Capacitive-piezoelectric AlN resonators with Q > 12 000," in *Proc. 24th IEEE Conf. Micro Electro Mechanical Systems (MEMS) 2011,* Cancun, Mexico, pp. 173–176.

[172] J. R. Anderson, "Pressure gauge for corrosive gases in the micron and submicron region," *Rev. Sci. Instrum.*, vol. 29, no. 12, pp. 1073, 1958.

[173] R. G. Christian, "The theory of oscillating-vane vacuum gauges," *Vacuum,* vol. 16, no. 4, pp. 175-178, Apr. 1966.

[174] J. Lu, T. Ikehara, Y. Zhang, T. Mihara, T. Itoh, R. Maeda, "High quality factor silicon cantilever driven by PZT actuator for resonant based mass detection," in *Proc. Symp. on Design, Test, Integration and Packaging of MEMS/MOEMS*, Nice, France, 2008, pp. 60-65.

[175] J. Lübbe, M. Temmen, H. Schieder and M. Reichling, "Measurement and modelling of non-contact atomic force microscope cantilever properties from ultra-high vacuum to normal pressure conditions," *Meas. Sci. Technol.*, vol. 22, no. 5, pp. 055501, May 2011.

[176] H. Sumali, "Squeeze-film damping in the free molecular regime: model validation and measurement on a MEMS," *J. Micromech. Microeng.*, vol. 17, no. 11, pp. 2231–2240, Nov. 2007.

[177] J. W. Lee, R. Tung, A. Raman, H. Sumali and J. P. Sullivan, "Squeeze-film damping of flexible microcantilevers at low ambient pressures: theory and experiment," *J. Micromech. Microeng.*, vol. 19, no. 10, pp. 105029, Oct. 2009.

[178] M. Bao, H. Yang, H. Yin and Y. Sun, "Energy transfer model for squeeze-film air damping in low vacuum," *J. Micromech. Microeng*., vol. 12, no. 3, pp. 341-346, May 2002.

[179] S. Hutcherson and W. Ye, "On the squeeze-film damping of micro-resonators in the free-molecule regime," *J. Micromech. Microeng.*, vol. 14, no. 12, pp. 1726–1733, Dec. 2004.

[180] J. D. Zook, D. W. Burns, H. Guckel, J. J. Sniegowski, R. L. Engelstad and Z. Feng, "Characteristics of polysilicon resonant microbeams," *Sens. Actuators A, Phys.*, vol. 35, no. 1, pp. 51–59, Oct. 1992.

[181] C Feng, L.Y.Jiang, "Molecular dynamics simulation of squeeze-film damping effect on nano resonators in the free molecular regime," *Physica E*, vol. 43, no. 9, pp. 1605-1609, Jul. 2011.

[182] K. Kokubun, M. Hirata, H. Murakami, Y. Toda and M. Ono, "A bending and stretching mode crystal oscillator as a friction vacuum gauge," *Vacuum*, vol. 34, no. 8-9, pp. 731-735, Aug. 1984.

[183] A. A. Kosterev, "Applications of quartz tuning forks in spectroscopic gas sensing," *Rev. Sci. Instrum.,* vol. 76, no. 4, pp. 043105, 2005.

[184] K. Kokubun, M. Hirata, M. Ono, H. Murakami and Y. Toda, "Unified formula describing the impedance dependence of a quartz oscillator on gas pressure," *J. Vac. Sci. Technol. A*, vol. 5, no. 4, pp. 2450-2453, Jul. 1987.

[185] K. Kokubun, M. Hirata, M. Ono, H. Tanaka, R. Aida and A. Nagata, "Dependence of the pressure sensitivity of a quartz oscillator on its size," *Vacuum*, vol. 40, no. 6, pp. 521-524, Jan. 1990.

[186] J-H. Lee, S-T. Lee, C-M. Yao and W. Fang, "Comments on the size effect on the microcantilever quality factor in free air space," *J. Micromech. Microeng.*, vol. 17, no. 1, pp. 139-146, Jan. 2007.

[187] S. Bianco, M. Cocuzza, S. Ferrero, E. Giuri and G. Piacenza, "Silicon resonant microcantilevers for absolute pressure measurement," *J. Vac. Sci. Technol. B*, vol. 24, no. 4, pp. 1803-1809, Jul/Aug 2006.

[188] G. K. Youngren and A. Acrivos, "Stokes flow past a particle of arbitrary shape: A numerical method of solution," *J. Fluid Mech.*, vol. 69, no. 2, pp. 377-403, May 1975.

[189] B. Munshi, R. P. Chhabra and P. S. Ghoshdastidar, "A numerical study of steady incompressible Newtonian fluid flow over a disk at moderate Reynolds numbers," *Can. J. Chem. Eng.*, vol. 77, no. 1, pp. 113-118, Feb. 1999.

[190] G. K. Batchelor, "Slender-body theory for particles of arbitrary cross-section in Stokes flow," *J. Fluid Mech.*, vol. 44, no. 3, pp. 419-440, Nov. 1970.

[191] M. J. Gluckman, S. Weinbaum and R. Pfeffer, "Axisymmetric slow viscous flow past an arbitrary convex body of revolution," *J. Fluid Mech.*, vol. 55, no. 4, pp. 677, Oct. 1972.

[192] S. Lee, Y. Moon, J. Yoon and H. Chung, "Analytical and finite element method design of quartz tuning fork resonators and experimental test of samples manufactured using photolithography 2: comprehensive analysis of resonance frequencies using Sezawa's approximations," *Vacuum*, vol. 78, no. 1, pp. 91-105, Apr. 2005.

[193] X. Jun, Y. Bo, L. Xin and C. Juan, "Theoretical model and optimization of a novel temperature sensor based on quartz tuning fork resonators," *Physica Scripta*, vol. T129, pp. 316-320, Dec. 2007.

[194] P. R. Heyliger, "When beam theories fail," *J. Mech. Mater. Struct.*, vol. 8, no. 1, pp. 15-35, Mar. 2013.

[195] M. A. G. Suijlen, J. J. Koning, M. A. J. van Gils, H. C. W. Beijerinck, "Squeeze film damping in the free molecular flow regime with full thermal accommodation," *Sens. Actuators A, Phys.*, vol. 156, no. 1, pp. 171–179, Nov. 2009.

[196] M. A. G. Suijlen, C. van der Avoort, J. T. M. van Beek, J. J. Koning, H. C. W. Beijerinck, "Dual-mode device for *in situ* testing of MEMS packaging quality," *Sens. Actuators A, Phys.*, vol. 175, pp. 139–149, Mar. 2012.

[197] O. Leroy, J. Perrin, J. Jolly, M. Péalat and M. Lefebvre, "Thermal accommodation of a gas on a surface and heat transfer in CVD and PECVD experiments," *J. Phys. D Appl. Phys.*, vol. 30, no. 4, pp. 499-509, Feb. 1997.

[198] W. M. Trott, J. N. Castañeda, J. R. Torczynski, M. A. Gallis, and D. J. Rader, "An experimental assembly for precise measurement of thermal accommodation coefficients," *Rev. Sci. Instrum.*, vol. 82, no. 3, pp. 035120, 2011.

[199] A. D. Chew, "Comment on ‘Survey on measurement of tangential momentum accommodation coefficient’ [J. Vac. Sci. Technol. A26, 634 (2008)]," *J. Vac. Sci. Technol. A*, vol. 27, no. 3, pp. 591-592, May/Jun 2009.

[200] E. B. Arkilic, K. S. Breuer and M. A. Schmidt, "Mass flow and tangential momentum accommodation in silicon micromachined channels," *J. Fluid Mech.*, vol. 437, pp. 29-43, Jun. 2001.

[201] J. R. Srour, C. J. Marshall and P. W. Marshall, "Review of displacement damage effects in silicon devices," *IEEE Trans. Nucl. Sci.*, vol. 50, no. 3, pp. 653-670, Jun. 2003.

[202] H. Lorenz, M. Despont, N. Fahrni, J. Brugger, P. Vettiger, P. Renaud, "High-aspect-ratio, ultrathick, negative-tone near-UV photoresist and its application for MEMS," *Sens. Actuators A, Phys.*, vol. 64, no. 1, pp. 33-39, Jan. 1998.

[203] A. Del Campo and C. Greiner, "SU-8: a photoresist for high-aspect-ratio and 3D submicron lithography," *J. Micromech. Microeng.*, vol. 17, no. 6, pp. R81-R95, Jun. 2007.

[204] Y. Gonin, F. Munnik F. Benninger, F. Dias and S. Mikhailov, "Comparison of a new photoresist (DiaPlate 133) with SU-8 using both x-ray and ion beam lithographies," *J. Vac. Sci. Technol. B*, vol. 22, no. 4, pp. 1982-1986, 2004.

[205] L. J. Guerin, M. Bossel, M. Demierre, S. Calmes and Ph. Renaud, "Simple and low cost fabrication of embedded microchannels by using a new thick-film photoplastic," in *Proc. Transducers*, 1997, vol. 1-2, pp. 1419-1422.

[206] I. Roch, Ph. Bidaud, D. Collard and L. Buchaillot, "Fabrication and characterization of an SU-8 gripper actuated by a shape memory alloy thin film," *J. Micromech. Microeng.*, vol. 13, no. 2, pp. 330-336, Mar. 2003.

[207] M. Niklaus, S. Rosset and H. Shea, "Array of lenses with individually tunable focal-length based on transparent ion-implanted EAPs," in *Proc. SPIE*, 2010, pp. 76422K.

[208] M. J. Key, V. Cindro and M. Lozano, "On the radiation tolerance of SU-8, a new material for gaseous microstructure radiation detector fabrication," *Radiat. Phys. Chem.*, vol. 71, no. 5, pp. 1003–1007, Dec. 2004.

[209] J. F. Ziegler, J. P. Biersack and U. Littmark, *Stopping and Range of Ions in Solids*, New York: Pergamon Press, 1985. Software available online: www.srim.org (Accessed on 10. Jun. 2011).

[210] P. Atkins and J. De Paula, *Physical Chemistry*, 8th ed. New York: W. H. Freeman and Company, 2006, ch. 13.

[211] S. Schmid and C. Hierold, "Damping mechanisms of single-clamped and prestressed double-clamped resonant polymer microbeams," *J. Appl. Phys.*, vol. 104, no. 9, 093516, 2008.

[212] S. R. Messenger, E. A. Burke, G. P. Summers, M. A. Xapsos, R. J. Walters, E. M. Jackson and B. D. Weaver, "Nonionizing energy loss (NIEL) for heavy ions," *IEEE Trans. Nucl. Sci.*, vol. 46, no. 6, pp. 1595-1602, Dec. 1999.

[213] E. H. Lee, "Ion-beam modification of polymeric materials – fundamental principles and applications," *Nucl. Instrum. Methods Phys. Res. B, Beam Interact. Mater. At.*, vol. 151, no. 1-4, pp. 29-41, May 1999.

[214] Z. F. Di, M. Q. Huang, Y. Q. Wang and M. Nastasi, "Dynamic annealing versus thermal annealing effects on the formation of hydrogen-induced defects in silicon," *Appl. Phys. Lett.*, vol. 97, no. 19, pp. 194101, 2010.

[215] E. H. Lee, G. R. Rao and L. K. Mansur, "Hardness enhancement and crosslinking mechanisms in polystyrene irradiated with high energy ion-beams," *Mater. Sci. Forum*, vol. 248-249, pp. 135-146, Dec. 1997.

[216] T. L. Tan, D. Wong, P. Lee, R. S. Rawat and A. Patran, "Study of a chemically amplified resist for x-ray lithography by Fourier Transform Infrared Spectroscopy," *Appl. Spectrosc.*, vol. 58, no. 11, pp. 1288-1294, Nov. 2004.

[217] S. Keller, G. Blagoi, M. Lillemose, D. Haefliger and A. Boisen, "Processing of thin SU-8 films," *J. Micromech. Microeng.*, vol. 18, no. 12, pp. 125020, Dec. 2008.

[218] D. Wong, T. L. Tan, P. Lee, R. S. Rawat and A. Patran, "Study of x-ray lithographic conditions for SU-8 by Fourier transform infrared spectroscopy," *Microelectron. Eng.*, vol. 83, no. 10, pp. 1912-1917, Oct. 2006.

[219] Y. Wang, J-H. Pai, H-H. Lai, C. E. Sims, M. Bachman, G. P. Li and N. L. Allbritton, "Surface graft polymerization of SU-8 for bio-MEMS applications," *J. Micromech. Microeng.*, vol. 17, no.7, pp. 1371-1380, Jul. 2007.

[220] M. Joshi, N. Kale, R. Lal, V. R. Rao and S. Mukherji, "A novel dry method for surface modification of SU-8 for immobilization of biomolecules in bio-MEMS," *Biosens. Bioelectron.,* vol. 22, no. 11, pp. 2429-2435, May 2007.

[221] A. Chapiro, "Chemical modifications in irradiated polymers," *Nucl. Instrum. Methods Phys. Res. B, Beam Interact. Mater. At.*, vol. 32, no. 1-4, pp. 111-114, May 1988.

[222] T. Sasuga, H. Kudoh and T. Seguchi, "High energy ion irradiation effects on polymer materials-changes in mechanical properties of PE, PSF and PES," *Polymer*, vol. 40, no. 18, pp. 5095-5102, Aug. 1999.

[223] H. Koizumi, T. Ichikawa, H. Yoshida, H. Shibata, S. Tagawa and Y. Yoshida, "Radical formation in the radiolysis of solid alanine by protons and helium ions," *Nucl. Instrum. Methods Phys. Res. B, Beam Interact. Mater. At.*, vol. 117, no. 3, pp. 269-274, Sep. 1996.

[224] S. Seki, S. Tsukuda, K. Maeda, Y. Matsui, A. Saeki and S. Tagawa, "Inhomogeneous distribution of crosslinks in ion tracks in polystyrene and polysilanes," *Phys. Rev. B*, vol. 70, no. 14, 144203, Oct. 2004.

[225] S. Seki, K. Maeda, Y. Kunimi, S. Tagawa, Y. Yoshida, H. Kudoh, M. Sugimoto, Y. Morita, T. Seguchi, T. Iwai, H. Shibata, K. Asai, and K. Ishigure, "Ion beam induced crosslinking reactions in poly(di-n-hexylsilane)," *J. Phys. Chem. B*, vol. 103, no. 15, pp. 3043-3048, Apr. 1999.

[226] D. J. T. Hill and J. L. Hopewell, "Effects of 3 MeV proton irradiation on the mechanical properties of polyimide films," *Radiat. Phys. Chem.*, vol. 48, no. 5, pp. 533-537, Nov. 1996.

[227] T. Sasuga, S. Kawanishi, T. Seguchi and I. Kohno, "Proton irradiation effects on several organic polymers," *Polymer*, vol. 30, no. 11, pp. 2054-2059, Nov. 1989.

[228] A. Licciardello and O. Puglisi, "Anomalous molecular weight distribution in ion irradiated polystyrene near the gel transition," *Nucl. Instrum. Methods Phys. Res. B, Beam Interact. Mater. At.*, vol. 91, no. 1-4, pp. 436-441, Jun. 1994.

[229] J. L. Magee, and A. Chatterjee, "Radiation chemistry of heavy-particle tracks. 1. General considerations," *J. Phys. Chem.,* vol. 84, no. 26, pp. 3529-3536, Dec. 1980.

[230] C. Riedel, and R. Spohr, "Correcting overlapping counts in dose calibration at high event-densities," *Nuclear Tracks,* vol. 5, no. 3, pp. 265-270, Sep. 1981.

[231] J-D. Cho, H-T. Ju, Y-S. Park, J-W. Hong, "Kinetics of Cationic Photopolymerizations of UV-Curable Epoxy-Based SU8-Negative Photoresists With and Without Silica Nanoparticles," *Macromol. Mater. Eng.*, vol. 291, no. 9, pp. 1155–1163, Sep. 2006.

[232] R. Feng and R. J. Farris, "The characterization of thermal and elastic constants for an epoxy photoresist SU8 coating," *J. Mater. Sci.,* vol. 37, no. 22, pp. 4793-4799, Nov. 2002.

[233] L. P. Schanwald, J. R. Schwank, J. J. Sniegowski, D. S. Walsh, N. F. Smith, and K. A. Peterson, "Radiation effects on surface micro machined comb drives and microengine," *IEEE Trans. Nucl. Sci.*, vol. 45, no. 6, pp. 2789–2798, Dec. 1998.

[234] Defense Logistics Agency Standard MIL-STD-883H, (2009, Nov. 9) [Online]. Available: http://www.dscc.dla.mil/Downloads/MilSpec/Docs/MIL-STD-883/std883.pdf (Accessed on 03. May 2012).

[235] P. F. Fewster, *X-ray scattering from semiconductors*, 2nd ed. London: Imperial College Press, 2003, ch. 2, sec. 2.4, pp. 56-64.

[236] M. Sánchez del Río, C. Ferrero and V. Mocella, "Computer simulation of bent perfect crystal diffraction profiles," in Proc. SPIE, 2014, vol. 3151, pp. 312-323.

[237] A. de Rooij, "Corrosion in space," in *Encyclopedia of Aerospace Engineering*, John Wiley & Sons Ltd, 2010.

[238] R. A. Buser and N. F. de Rooij, "Very high Q-factor resonators in monocrystalline silicon," *Sensors and Actuators*, vol. A21-A23, pp. 323-327, 1990.

[239] S. Henein, F. Barrot, A. Dommann, S. Droz, L. Lisowski, J-M. Mayor, T. Overstolz, P. Schwab, P. Walter and C. Verjus, "Silicon flexure-based micro-balance for batch

weighing processes," CSEM Scientific and Technical report (2008), [Online], Available: http://www.csem.ch/docs/Show.aspx/9407/docname/CSEM-STR08-Page%2089.pdf (Accessed on 30. Dec. 2013).

[240] W. Weibull, "A statistical theory of the strength of materials," *Proc. Roy. Swedish Inst. for Eng. Res.*, vol. 151, no. 5, pp. 1-45, 1939.

[241] S. Schoenfelder, M. Ebert, C. Landesberger, K. Bock and J. Bagdahn, "Investigations of the influence of dicing techniques on the strength properties of thin silicon," *Microelectron. Reliab.*, vol. 47, no. 2-3, pp. 168-178, Feb. 2007.

[242] G. J. Nelson, M. J. Matthewson and B. Lin, "A novel four-point bend test for strength measurement of optical fibers and thin beams – Part I: Bending Analysis," *J. Lightwave Technol.*, vol. 14, no. 4, pp. 555-563, Apr. 1996.

[243] A. Ohtsuki, "An analysis of large deflections in a four-point bending with friction at all supports," *Bulletin of JSME,* vol. 29, no. 251, pp. 1377-1382, 1986.

[244] A. Ohtsuki, "A large deflection in a three-point bending," *J. Japan Soc. Mater. Sci.*, vol. 34, no. 387, pp. 1419-1423, 1985 (in Japanese).

[245] I. N. Bronstein, K. A. Semendjajew, G. Musiol and H. Mühlig, *Taschenbuch der Mathematik*, Thun CH: Verlag Harri Deutsch, 2001, pp. 928 (in german).

Publications

Peer-reviewed publications:

[1] A. Neels, O. Sereda, T. Bandi, and X. Maeder, "Crystallographic services and technology support for industry," *Chimia*, vol. 68, no. 1/2, pp. 14–18, Feb. 2014.

[2] T. Bandi, J. Gomes, A. Neels, A. Dommann, L. Marchand and H. R. Shea, "Proton-radiation tolerance of silicon and SU-8 as structural materials for high-reliability microsystems," *J. Microelectromech. Syst.*, vol. 22, no. 6, pp. 1395-1402, Dec. 2013.

[3] A. C. Clark, K. K. Schwarzwälder, T. Bandi, D. Maradan, and D. M. Zumbühl, "Method for cooling nanostructures to microkelvin temperatures," *Rev. Sci. Instrum.*, vol. 81, no. 10, pp. 103904, 2010.

[4] N. Plattner, T. Bandi, J. D. Doll, D. L. Freeman and M. Meuwly, "MD simulations using distributed multipole electrostatics: structural and spectroscopic properties of CO- and methane-containing clathrates," *Mol. Phys.*, vol. 106, no. 12-13, pp. 1675-1684, Jun. 2008.

Conference Proceedings:

[5] T. Bandi, H. R. Shea and A. Neels, "Mechanical properties of MEMS materials – Reliability investigations by mechanical- and HRXRD-characterization related to environmental testing," in *Proc. SPIE*, 2014, pp. 9113-10.

[6] T. Bandi, J. Baborowski, A. Dommann, H. Shea, F. Cardot and A. Neels, "Evaluation of silicon tuning-fork resonators under space-relevant radiation conditions," in *Proc. SPIE*, 2014, pp. 89750I.

[7] T. Bandi, X. Maeder, A. Dommann, H. Shea and A. Neels, "Improved test setup for MEMS mechanical strength investigations and fabrication process qualification," in *Proc. SPIE*, 2014, pp. 897509.

[8] T. Bandi, A. Dommann and A. Neels, "Analysis of Stress in Silicon-Based Microsystems by X-ray Diffraction Techniques," in *Proc. 2013 European Microelectronics Packaging Conf. (EMPC)*, Grenoble, France, pp. 1-4. This contribution won the **Best Paper Award**.

[9] T. Bandi, J. Polido-Gomes, A. Neels, A. Dommann and H. R. Shea, "Making MEMS more suited for Space: Assessing the proton-radiation tolerance of structural materials for microsystems in orbit," in *Proc. SPIE*, 2013, pp. 86140M-1.

[10] B. Neuenschwander, B. Jaeggi, M. Schmid, A. Dommann, A. Neels, T. Bandi, G. Hennig, "Factors controlling the incubation in the application of ps laser pulses on copper and iron surfaces," in *Proc. SPIE*, 2013, pp. 86070D.

[11] A. Dommann, T. Bandi and A. Neels, "Drift and aging investigations in silicon-based sensors," in *Proc. Microcar 2013*, Leipzig, Germany.

[12] T. Bandi, A. Dommann and A. Neels, "Stress investigations in silicon-based microsystems using x-ray diffraction methods," in *Proc. Microcar 2013*, Leipzig, Germany.

[13] Alex Dommann, Tobias Bandi and Antonia Neels, "Aging analysis for MEMS devices using X-ray techniques," in *Proc. Smart Systems Integration 2012*, Zürich, Switzerland.

[14] A. Neels, A. Dommann, T. Bandi, Ph. Niedermann, R. Kaufmann, G. Isella, C. V. Falub and H. von Känel, "A novel approach to reduce stress in thick Ge layers," in *Proc. MicroCar 2011*, Leipzig, Germany.

Submitted:

[15] T. Bandi, J. Baborowski, A. Dommann, H. Shea, F. Cardot and A. Neels, "Evaluation of silicon tuning-fork resonators under mechanical loads and space-relevant radiation conditions," (under review in *J. Micro/Nanolith. MEMS MOEMS*).

Poster presentations:

[16] X. Maeder, T. Bandi, A. Neels, A. Dommann, Y. Dupraz and M-C. Pasquier, "Qualification of Laser Processes for Chip Separation using HRXRD and Micromechanical Testing," *Swiss Nanoconvention*, Basel, Switzerland, 2013.

[17] T. Bandi, A. Neels, A. Dommann, P. Niedermann, C. V. Falub, H. von Känel, "HRXRD studies on high quality epitaxial germanium on pre-patterned silicon," *Annual Meeting of the Swiss Crystallographic Society*, Bern, Switzerland, 2011.

Curriculum vitae

Personal information

First name / Surname	Bandi Tobias
Nationality	Swiss
Date of birth	10. August 1984

Education

September 2010 – August 2014	PhD Studies at CSEM SA and EPFL of which 8 months at ESA/ESTEC, Noordwijk (NL)
September 2003 – February 2005 and March 2006 – April 2009	Bachelor of Science and Master of Science with Major Nano-Sciences at the University of Basel (CH)
August 2000 – August 2003	Matura with Major Biology and Chemistry, Gymnasium Thun Seefeld, (CH)

Professional experience

Mai 2009 – July 2010	Consultant, Oepfelbaum IT Management AG, Zürich (CH)
October 2005 – February 2006	System tester, Oepfelbaum IT Management AG, Zürich (CH)
March – September 2005	Guide in the Swiss pavilion at the World Exposition 2005 in Nagoya (JPN)

Languages	German (first language), English, French
IT and Computer skills	Comsol, LabView, Latex, Matlab, Microsoft Office Tools, Octave, SRIM